

**Formation of Ordered Structures with Symmetries  
other than Hexagonally Close-Packed**

**Dissertation**

zur Erlangung des akademischen Grades eines  
Doktors der Naturwissenschaften (Dr. rer. nat.)

in der Bayreuther Graduiertenschule  
für Mathematik und Naturwissenschaften (BayNAT)  
der Universität Bayreuth

vorgelegt von

**Miriam Eugenie Judith Hummel**

aus Rüdesheim am Rhein

Bayreuth, 2019



Die vorliegende Arbeit wurde in der Zeit von Oktober 2014 bis September 2018 in Bayreuth am Lehrstuhl Physikalische Chemie I unter Betreuung von Herrn Professor Dr. Stephan Förster angefertigt.

Vollständiger Abdruck der von der Bayreuther Graduiertenschule für Mathematik und Naturwissenschaften (BayNAT) der Universität Bayreuth genehmigten Dissertation zur Erlangung des akademischen Grades einer Doktorin der Naturwissenschaften (Dr. rer. nat.).

Dissertation eingereicht am: 04.09.2018

Zulassung durch das Leitungsgremium: 27.09.2018

Wissenschaftliches Kolloquium: 11.12.2018

Amtierender Direktor: Prof. Dr. Dirk Schüler

Prüfungsausschuss:

Prof. Dr. Stephan Förster	(Gutachter)
Prof. Dr. Andreas Greiner	(Gutachter)
JProf. Dr. Anna Schenk	(Vorsitz)
Prof. Dr. Markus Retsch	



Für meine Familie.



# Contents

<b>List of publications</b>	<b>V</b>
<b>List of abbreviations</b>	<b>VII</b>
<b>Abstract</b>	<b>1</b>
<b>Zusammenfassung</b>	<b>3</b>
<b>1 Introduction</b>	<b>5</b>
<b>2 Theory</b>	<b>13</b>
2.1 Essentials of colloidal self-assembly . . . . .	13
2.1.1 Synthesis of colloidal particles . . . . .	13
2.1.2 Colloidal stability . . . . .	16
2.1.3 Colloidal assembly at interfaces . . . . .	20
2.2 Quasicrystals . . . . .	26
2.2.1 Symmetries in periodic and non-periodic systems . . . . .	26
2.2.2 Quasicrystal models . . . . .	27
2.2.3 Soft quasicrystals . . . . .	30
2.3 Preparation and investigation of nano- and microstructures . . . . .	32
2.3.1 Soft Lithography . . . . .	33
2.3.2 Scanning electron microscopy . . . . .	35
<b>3 Synthesis of colloidal polymer particles</b>	<b>51</b>
3.1 Variation of co-monomer concentration . . . . .	51
3.2 Variation of reaction temperature . . . . .	53
3.3 Variation of the ionic strength . . . . .	54
<b>4 Preparation of two-dimensional Bravais lattices by colloidal self-assembly</b>	<b>57</b>
4.1 Preparation of colloidal monolayers . . . . .	59
4.2 Transfer of colloidal monolayers onto hydrophobic substrates . . . . .	60
4.3 Theoretical analysis of monolayer stretching . . . . .	65

4.4	Influence of the immersion direction during transfer . . . . .	71
4.5	Influence of the contact angle of the substrate . . . . .	72
4.6	Appendix . . . . .	76
<b>5</b>	<b>Preparation of quasicrystals by colloidal self-assembly</b>	<b>81</b>
5.1	Preparation of colloidal monolayers . . . . .	83
5.2	Theoretical analysis of quasicrystalline particle arrangements . . . . .	84
5.3	Influence of the particle number ratio . . . . .	86
5.4	Influence of the particle size ratio . . . . .	88
5.5	Calculation of bond orientational order . . . . .	89
5.6	Molecular dynamics simulations of binary particle mixtures . . . . .	90
<b>6</b>	<b>Preparation of quasicrystals by soft lithography</b>	<b>97</b>
6.1	Preparation of micropatterns by soft lithography . . . . .	99
6.2	Replication of micropatterns to thin metal layers . . . . .	101
6.3	Characterization of optical properties . . . . .	102
6.4	Simulation of waveguiding properties . . . . .	104
<b>7</b>	<b>Conclusion and future perspectives</b>	<b>109</b>
<b>8</b>	<b>Experimental Section</b>	<b>113</b>
8.1	Materials . . . . .	113
8.2	Synthesis . . . . .	113
8.2.1	Synthesis of PS colloids . . . . .	113
8.2.2	Synthesis of PMMA particles . . . . .	114
8.2.3	Synthesis of polymers for hydrophobic substrates . . . . .	114
8.3	Sample Preparation . . . . .	115
8.3.1	Preparation of hydrophobic substrates . . . . .	115
8.3.2	Preparation of two-dimensional colloidal crystals . . . . .	115
8.3.3	Preparation of quasicrystalline micropatterns . . . . .	117
8.4	Methods . . . . .	119
8.4.1	Scanning electron microscopy . . . . .	119

8.4.2	Contact angle . . . . .	119
8.4.3	Differential scanning calorimetry . . . . .	119
8.4.4	Optical microscopy . . . . .	119
8.4.5	Atomic force microscopy . . . . .	119
<b>Danksagung</b>		<b>121</b>
<b>Eidesstattliche Versicherungen und Erklärungen</b>		<b>123</b>



## List of publications

Parts of this thesis are based on contents that will be published in peer-reviewed journals:

1. Ordered Particle Arrays via a Langmuir Transfer Process : Access to Any Two-Dimensional Bravais Lattice. **M.E.J. Hummel**, C. Stelling, B.A.F. Kopera, F.A. Nutz, M. Karg, M. Retsch, S. Foerster. *Langmuir*, 2019, 35 (4), 973–979.  
*Adapted contents of this publication can be found in Chapters 1, 2, 4, 7 and 8.*
2. Quasicrystalline Order in Self-Assembled Binary Colloidal Monolayers. **M.E.J. Hummel**, M. Dulle, F.A. Nutz, M. Retsch, S. Foerster, 2019, *in preparation*  
*Adapted contents of this publication can be found in Chapter 1, 2, 3, 5, 7 and 8.*
3. Photonic Band Gaps in Quasicrystalline Structures: Quasirystals with Arbitrary Symmetry by Soft Lithography. **M.E.J. Hummel**, M. Dulle, B.A.F. Kopera, S. Foerster, 2019, *in preparation*  
*Adapted contents of this publication can be found in Chapter 1, 2, 6, 7 and 8.*

Further work from the following publications is not included in this thesis:

1. Interfacial stabilization by soft Janus nanoparticles. J.H. Schroeder, M. Doroshenko, D. Pirner, **M.E.J. Mauer**, B. Förster, V. Boyko, B. Reck, K.J. Roschmann, A.H.E. Müller, S. Foerster, 2016, *Polymer*
2. Reinforcement of nanostructured organogels by hydrogen bonds. D. Pirner, M. Dulle, **M.E.J. Mauer**, S. Foerster, 2016, *RSC Advances*



## List of abbreviations

<b>AA</b>	acrylic acid
<b>AFM</b>	atomic force microscopy
<b>AIBN</b>	azobisisobutyronitrile
<b>ATR-FTIR</b>	attenuated total reflection Fourier transform infrared spectroscopy
<b>BOO</b>	bond orientational order
<b>BSE</b>	backscattered electrons
<b>CAD</b>	computer-aided design
<b>cmc</b>	critical micelle concentration
<b>DLVO</b>	Deyaguin-Landau-Verwey-Overbeek
<b>EsB</b>	energy selective backscattered electrons
<b>FFT</b>	fast Fourier transform
<b>GDM</b>	generalized dual method
<b>hcp</b>	hexagonally close-packed
<b>HD</b>	high density
<b>IR</b>	infrared
<b>KPS</b>	potassium peroxodisulfate
<b>LD</b>	low density
<b>MD</b>	molecular dynamics
<b>MMA</b>	methyl methacrylate
<b>nBA</b>	<i>n</i> -butyl acrylate
<b>PAG</b>	photo acid generator
<b>PBG</b>	photonic band gap
<b>PDMS</b>	poly(dimethylsiloxane)
<b>PEB</b>	post exposure bake
<b>PMMA</b>	poly(methyl methacrylate)

<b>P(nBA-co-MMA)</b>	poly( <i>n</i> -butyl acrylate-co-methyl methacrylate)
<b>P(nBA-co-S)</b>	poly( <i>n</i> -butyl acrylate-co-styrene)
<b>PS</b>	polystyrene
<b>PTFE</b>	polytetrafluoroethylene
<b>SDS</b>	sodium dodecyl sulfate
<b>SE</b>	secondary electrons
<b>SEM</b>	scanning electron microscopy
<b>SERS</b>	surface enhance Raman spectroscopy
<b>TEM</b>	transmission electron microscopy
<b>T<sub>g</sub></b>	glass transition temperature
<b>ROP</b>	ring opening polymerization

## Abstract

Self-assembly is one of the most intriguing phenomena in nature and has inspired scientists across disciplines. In particular, colloidal crystallization has been the subject of intensive research. Analogously to the natural examples, artificial systems feature, in most cases, a hexagonal close-packed arrangement. This is the result of an interplay of attractive and repulsive forces between particles which lead to thermodynamically stable arrangements with the highest packing volume fraction. Applications of these systems are found in optical devices due to their ability to diffract visible light. Although hexagonal systems are well established, an extension to other geometries is sorely needed and would increase the applicability of these systems with their more unusual physical properties.

The scope of this thesis is the preparation of ordered structures with symmetries other than hexagonal close-packed. More precisely, colloidal crystals for all two-dimensional Bravais lattices and colloidal quasicrystals with dodecagonal symmetry were obtained by interfacial self-assembly. Furthermore, quasicrystalline structures with arbitrary symmetries were fabricated using soft lithography. The advantage of self-assembled (quasi-) crystals is that they can readily form at interfaces due to the presence of interparticle forces. However, without further modification of the self-assembly process only crystals with six-fold symmetry will form from monodisperse, spherical particles of one size. For this reason, soft lithography is an attractive supplement as here the final structures are independent from chemical or physical forces, but can be designed in advance without limitation in symmetry.

For colloidal self-assembly, the polymer colloids were synthesized via surfactant-free emulsion polymerization. The major prerequisites for controlled crystallization are monodispersity in single particle systems, and for binary particle systems distinct particle sizes. In order to meet these requirements, the synthesis of polystyrene colloids was studied thoroughly. The diameter of the colloids was adjusted by a combination of various parameters including temperature, concentration of acrylic acid (co-monomer), and variation of the ionic strength. For all parameters a linear dependence was observed so that a precise size adjustment was possible. Besides simple polystyrene colloids, particles consisting of poly(*n*-butyl acrylate-co-methyl methacrylate) were synthesized. These particles feature the properties of hard spheres, but offer a low glass transition temperature that can be used as tool for thermal fixation.

The self-assembly of different colloids was accomplished at the water/air interface. The starting point for the preparation of particle arrays featuring the two-dimensional Bravais lattices is a colloidal monolayer at the water/air interface with hexagonal close-packed symmetry. The astonishing fact is that this monolayer can be transferred into an arbitrary Bravais lattice just by one-dimensional stretching. In experiments, the floating colloidal crystal was collected on a hydrophobic substrate which induced a linear stretching along

the uptake direction. With this, the magnitude of stretching is dependent on the contact angle of the substrate. The crucial step for the preservation of the stretched structures is a final thermal fixation to avoid re-contraction by capillary forces upon drying.

For more complex structures, binary particle systems were self-assembled at the water/air interface. The influence of size and number ratio of small and large particles was studied in more detail. Theoretical considerations for possible geometries of quasicrystalline particle arrangements were compared with experimental results of interfacial self-assembly and molecular dynamics simulations. In theory, two variations of a dodecagonal quasicrystal can be predicted for a binary particle system. However, the experimental results suggested that only the high density quasicrystal is in practice feasible whereas the low density geometry is not stable, which was confirmed by simulations. Moreover, the simulations revealed that only within a narrow range of size and number ratios do quasicrystalline structures form.

An even broader variety of structures can be realized by soft lithography. Using computer-aided design software, arbitrary patterns can be designed and created with lithography techniques. The advantage of this method is the possibility to fabricate single (quasi-) crystals on a centimeter scale without any defects. Furthermore, soft lithography based on polydimethylsiloxane is compatible with other materials. As a consequence, structures can be transferred to other moldable materials or thin metal films. In this thesis, quasicrystalline structures were prepared and characterized with respect to their optical properties. It was observed that the transmission was decreased in a certain wavelength range dependent on the lattice constant. This suggests that the manufactured structures are able to open a (partial) photonic band gap.

In summary, these results are the first to show convenient protocols for the preparation of two-dimensional ordered structures with symmetries other than hexagonal close-packed. This is a milestone for future works that deal with colloidal (quasi-)crystals for the investigation of optical phenomena and for the preparation of functional devices e.g. in the field of photonics for telecommunication, illumination and data storage.

## Zusammenfassung

Die Selbst-Assemblierung ist eines der faszinierendsten Phänomene der Natur, das Wissenschaftler aus verschiedensten Fachrichtungen inspiriert hat. In einem besonderen Fokus steht dabei die Kristallisation von Kolloiden. Ähnlich wie in der Natur, besitzen auch künstliche kolloidale Systeme in den meisten Fällen eine hexagonale, dichte Packung - ein thermodynamisch stabiler Zustand mit dem höchsten Partikelvolumenanteil. Dieses Verhalten resultiert aus einem Zusammenspiel von anziehenden und abstoßenden Kräften, die zwischen den Partikeln herrschen. Kolloidale Kristalle werden hauptsächlich in optischen Bauteilen verwendet, wo man ihre Fähigkeit sichtbares Licht zu beugen ausnutzt. Obwohl sich die hexagonalen Systeme in vielen Anwendungen bewährt haben, ist es wünschenswert auch geordnete Strukturen mit anderen Symmetrien besser zu erforschen. Weitere einfach zugängliche Geometrien würden die Zahl der Anwendungen erhöhen und sie durch neue physikalische Eigenschaften bereichern.

Die vorliegende Arbeit beschäftigt sich mit geordneten Strukturen, die sich von der hexagonalen, dichten Packung unterscheiden. Genauer gesagt, wurden kolloidale Kristalle mit allen existierenden zweidimensionalen Bravais-Gittern und zwölfachsig symmetrische kolloidale Quasikristalle durch Selbst-Assemblierung an Grenzflächen hergestellt. Daneben wurden quasikristalline Strukturen mit beliebiger Symmetrie über *Soft Lithografie* geschaffen. Der Vorteil der selbst-assemblierten (Quasi-)Kristalle ist, dass sie sich eigenständig aufgrund eines Kräftegleichgewichts zwischen den Partikeln an Grenzflächen bilden. Allerdings sind mit dieser Methode für sphärische Partikel in der Regel lediglich Kristalle mit sechsfacher Symmetrie erhältlich, sofern der Assemblierungsprozess nicht durch menschliche Hand abgewandelt wird. Aus diesem Grund ist *Soft Lithografie* eine attraktive Ergänzung, da hier die erhaltenen Strukturen nicht von chemischen oder physikalischen Kräften abhängig sind, sondern im Voraus ohne Limitierung der Symmetrieeigenschaften entworfen werden können.

Für die Selbst-Assemblierung von Kolloiden wurden Polymerpartikel mittels emulgatorfreier Emulsionspolymerisation synthetisiert. Um eine kontrollierte Kristallisation zu ermöglichen, müssen die Partikel eine hohe Monodispersität in Ein-Partikel-Systemen und zusätzlich ein genaues Größenverhältnis in Zwei-Partikel-Systemen aufweisen. Um diese Voraussetzungen zu erfüllen, wurde die Synthese von Polystyrol-Partikeln genauer untersucht. Der Durchmesser der Partikel konnte über verschiedene Parameter beeinflusst werden. Sowohl Reaktionstemperatur und Konzentration der Acrylsäure (Co-Monomer) als auch die Ionenstärke bewirken eine lineare Veränderung der Partikelgröße. Neben einfachen Polystyrol-Partikeln wurden weiterhin Partikel aus Poly(*n*-butylacrylatcomethylmethacrylat) hergestellt. Diese Partikel vereinen die Eigenschaften von harten Kugeln mit einer niedrigen Glasübergangstemperatur. Damit können die Partikel durch Erwärmung auf Oberflächen fixiert werden.

In dieser Arbeit wurden verschiedene Kolloide an der Wasser/Luft-Grenzfläche ange-

ordnet und untersucht, unter welchen Bedingungen sich neue Strukturen ausbilden. Der Ausgangspunkt für die Ordnung von Partikeln in zweidimensionalen Bravais-Gittern ist eine kolloidale Monolage an der Wasser/Luft-Grenzfläche mit einfacher hexagonal, dichter Packung. Das beeindruckende ist, dass diese Monolage nur mit Hilfe einer eindimensionalen Verstreckung in ein beliebiges Bravais-Gitter umgewandelt werden kann. Dazu wurde in den Experimenten die schwimmende Monolage auf ein hydrophobes Substrat aufgenommen. Die Verstreckung erfolgte hierbei in Richtung der Aufnahme, wobei der Verstreckungsfaktor nur von dem Kontaktwinkel des Substrats abhängig ist. Der entscheidende Schritt dieser Methode ist die thermische Fixierung der Partikel auf dem Substrat, ohne diese sich die Strukturen aufgrund von Kapillarkräften während dem Trocknen wieder zusammen ziehen würden.

Komplexere Strukturen wie beispielsweise Quasikristalle wurden durch die Selbst-Assemblierung von Zwei-Partikel-Systemen hergestellt. In diesem Zusammenhang wurden vor allem die Auswirkungen des Größen- und Zahlenverhältnisses von kleinen zu großen Partikeln näher untersucht. Die theoretische Betrachtung von möglichen quasikristallinen Partikelanordnungen wurde mit experimentellen Ergebnissen und *Molecular Dynamics* Simulationen verglichen. Prinzipiell sind zwei Variationen eines zwölfachsig symmetrischen Quasikristalls denkbar, der durch Selbst-Assemblierung von zwei verschiedenen Partikelgrößen entsteht. Allerdings zeigte sich in den Experimenten, dass nur der Quasikristall mit höherer Dichte gebildet wird, während der mit niedriger Dichte nicht stabil ist. Dieses Ergebnis wird auch durch die Simulationen bestätigt. Darüber hinaus zeigt sich in den Simulationen, dass sowohl das Größen- als auch das Zahlenverhältnis empfindliche Parameter sind. Das hat zur Folge, dass sich quasikristalline Strukturen nur innerhalb eines engen Parameterfensters formieren.

Um eine noch größere Vielfalt an geordneten Strukturen zu realisieren, wurde in dieser Arbeit *Soft Lithografie* verwendet. Mit Hilfe von rechnerunterstützter Konstruktionssoftware, können beliebige Muster entworfen und durch Lithografie hergestellt werden. Ein großer Vorteil dieser Methode ist die Möglichkeit Ein(-quasi-)kristalle ohne Defektstrukturen im Zentimetermaßstab zu erstellen. Des Weiteren ist *Soft Lithografie* basierend auf Polydimethylsiloxan einfach handhabbar und kompatibel mit einer Reihe weiterer formbarer Materialien sowie dünnen Metallschichten. In dieser Arbeit wurden die optischen Eigenschaften der hergestellten quasikristallinen Strukturen untersucht. Die Ergebnisse zeigten, dass innerhalb eines bestimmten Wellenlängenbereichs, abhängig von der Gitterkonstante, eine reduzierte Transmission vorliegt. Das deutet darauf hin, dass die gefertigten Strukturen (partielle) photonische Bandlücken besitzen können.

Zusammenfassend stellt diese Arbeit einfache Methoden vor, um zweidimensionale geordnete Strukturen, insbesondere mit nicht hexagonaler Symmetrie herzustellen. Das ist ein Meilenstein für zukünftige Arbeiten auf dem Gebiet der kolloidalen (Quasi-)Kristalle, vor allem für die Untersuchung von photonischen Eigenschaften und die Herstellung von funktionalen Bauteilen für Telekommunikation, Beleuchtung und Datenspeicherung.

# 1 Introduction

Self-assembly describes the process of spontaneous organization of individual components into ordered structures. It is *the science of things that put themselves together*.<sup>[1]</sup> The human fascination for order that arises from disorder originates in nature that evolves incredibly complex structures in an uncountable number. Starting from huge galaxies, nature provides organized structure at all length scales down to molecular crystals.

One characteristic that reoccurs in many systems in nature is the hexagonal arrangement of individual entities. The hexagonal order is the result of investing the minimum amount of energy to gain maximum efficiency. Interestingly, we observe this behavior both in living and inanimate systems. We find hexagonal patterns in both honeycomb structures built by bees in their nests, and in the shape of snowflakes (Figure 1.1).

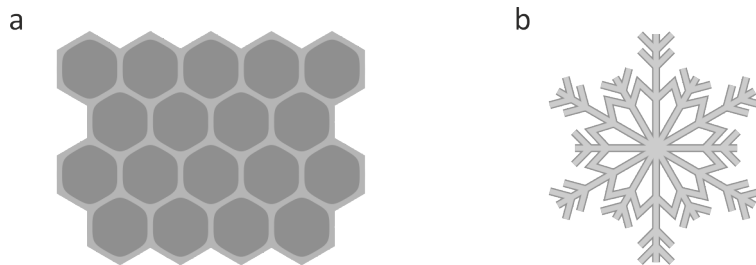


Figure 1.1: Schematic illustrations of hexagonal shapes in nature: (a) honeycombs and (b) snowflakes.

All these examples are based on the same principle: minimizing the surface area for a two-dimensional arrangement of regular shapes. In living examples, the hexagons are the result of intelligence documented in the genetic material. Bees are concerned about using wax as sparsely as possible to create mechanically stable structures. They build their hexagonal cells in order to achieve the best economy of material. Non-living examples, emerge from the physical laws of nature. Snowflakes, for example, result from the crystallization of water molecules that align in order to maximize attractive and minimize repulsive interactions.

Over millenia, nature has evolved efficient mechanisms to assemble molecules at all length scales. This initiated a concerted effort by scientists to mimic nature with synthetic systems. The natural processes have become an inspiration to self-assemble artificial architectures starting from the nanoscale.

Given the observations of order in nature, it is hardly surprising that many self-assembled artificial systems show hexagonal order. The first discovery of colloidal crystallization in two-dimensions by Pieranski in 1980 showed that there is a general framework of forces that enables self-assembly of colloidal crystals at interfaces.<sup>[2]</sup> The self-assembly of polystyrene (PS) particles at the water/air interface yielded a hexagonal lattice as a state of minimum energy. Since then, much research has been devoted to explain the

process of colloidal self-assembly. Today, we know that self-assembly is based on the concept of force balance. The spontaneous association is the result of an interplay of attractive and repulsive forces between the colloids.<sup>[3]</sup> Many techniques for the fabrication of two-dimensional colloidal crystals have been developed and optimized with respect to their throughput, reproducibility and quality.<sup>[4]</sup> The common feature of these self-assembly techniques is that monodisperse colloidal particles readily assemble into hexagonally close-packed (hcp) arrays. These particle arrays are widely used as versatile templates, e. g. for surface patterning. By contrast to the large variety of hexagonal structures, there are only a small number of methods that yield non-hexagonal structures. These other symmetries feature new and more unusual physical properties, which could add more flexibility to existing applications.<sup>[4]</sup>

In this concern, lithography methods are significantly more versatile than self-assembly for surface patterning as they are not limited to physical and chemical forces that govern the process of colloidal self-assembly. Today, the ability to create patterns on the micro- and nanoscale can be accomplished by various techniques ranging from electron beam lithography to photo lithography and soft lithography. A common principle for these methods is the preparation of appropriate templates (masks, stamps) that comprise the desired structure with an arbitrary design. The replication of these templates eventually yields structured surfaces in manifold materials. However, a general drawback of lithography is the relatively low throughput combined with high costs and the requirement for specialized equipment.<sup>[5]</sup>

**Aim of the thesis.** The focus of this thesis is on the generation of ordered structures via self-assembly and lithography on the nano- to micro-scale. Non-hexagonal, crystalline and quasicrystalline rather than ubiquitous hexagonal structures are of particular interest. As described above, both methods – self-assembly and lithography – offer attractive benefits for the fabrication of two-dimensional patterns. For this reason, the following work relies on both techniques to create structures with different characteristics resulting from the features of the individual manufacture processes.

It has been shown that monodisperse particles are able to assemble into two-dimensional structures which show a hexagonal order with large-scale uniform domain orientation. The assembled particle arrays can be transferred to different substrates and used for various applications e. g. in lithography<sup>[6,7]</sup>, optics<sup>[8]</sup> and photonics<sup>[9]</sup>. A striking advantage over other methods generating structures in the nano- to micrometer range is that colloidal self-assembly is cheap and fast. However, it also has a major disadvantage which is the restriction to structures that result from the assembly process. In most cases these structures are based on hexagonally close-packed arrangements of the colloids as a result of attractive capillary forces between the particles. As opposed to this many applications would benefit from non-close-packed particle arrays with tunable interparticle distances, and non-hexagonal symmetries to control optical, adhesive or magnetic sur-

face properties, e. g., in the case of anti-reflective coatings<sup>[10]</sup> or photonic band gap devices<sup>[11]</sup>. Only over the last decade have attempts been made to assemble more complex structures. The approaches cover both the formation of non-close-packed, hexagonal arrangements<sup>[4,12-17]</sup> and the more intricate non-close-packed, non-hexagonal arrangements<sup>[18-22]</sup>. *However, the reported strategies either yield non-close-packed structures which are only stable at the fluid interface or the fabrication is based on complex multi-step procedures. This thesis reveals a new, straightforward strategy to produce colloidal crystals with the symmetry of all five two-dimensional Bravais lattices. The method relies on hexagonally close-packed monolayers at the water/air interface which are stretched in one dimension by collection on hydrophobic substrates. Herein, the role of the attractive capillary forces, which usually promote the formation of close-packed, hexagonal structures upon drying, is closer analyzed. In the course of investigations, it is shown that a combination of hydrophobic collection substrate and adhesive fixation of the particles introduces a variety of stable non-close-packed, non-hexagonal arrays. In order to increase the versatility of the method both adhesive particles and adhesive substrates are developed. In addition, the direct dependence of the final structure on the hydrophobicity of the substrate and the orientation of the monolayer at the interface is revealed.*

Another advance in colloidal self-assembly relates to the formation of colloidal crystals from particles with different sizes. Vogel *et al.*<sup>[23]</sup> presented a range of crystal structures assembled from binary particle mixtures. Besides, Talapin *et al.*<sup>[24]</sup> were the first to show that nanoparticles of two distinct sizes can self-assemble into quasicrystalline arrangements. *This thesis combines the mentioned studies and investigates the formation of binary colloidal quasicrystals by self-assembly. Thereby, the crucial role of the number and size ratios of the particles is emphasized.* Today, synthesis protocols allow the manufacture of particles from various materials with high accuracy concerning their size and monodispersity. A straightforward synthetic strategy to produce large amounts of well-defined colloidal particles is surfactant-free emulsion polymerization of styrene.<sup>[25]</sup> *In order to determine important parameters of the synthesis and to achieve maximal control on the size of the colloids, this reaction protocol is analyzed thoroughly. Therefore, the influence of the monomer and comonomer concentration, the reaction temperature and the ionic strength on the final reaction products are investigated.* For quasicrystals with twelve-fold symmetry various tilings and combinations of small and large particles are conceivable. However, most models are based on an Archimedian-like tiling of squares and triangles. Talapin *et al.*<sup>[24]</sup> reported that the vertices of this tiling are decorated with large particles, whereas the interstices of the squares are additionally filled with six octahedrally arranged small particles. Thereof they derived a distinct number and size ratio as prerequisite for the formation of quasicrystalline domains. *Proceeding from their consideration, in this thesis different decorations of a dodecagonal quasicrystal with small and large particles at the water/air interface are analyzed. Self-assembly is investigated experimentally with varying number and size ratios. Furthermore, theoretical simulations complement the experimental findings and elucidate the influence of number, size and repulsion/attraction of the particles.*

Although it has been shown that self-assembled structures can both be non-close-packed and non-hexagonal, self-assembly still cannot produce arbitrary particle arrangements. Compared to self-assembly, lithography is able to create structures with any conceivable design. Lithography can be used to create near-diffraction limited features with either light or electrons/ions as the writing beam. While the latter possesses a far higher resolution, it is slow and requires costly equipment. However, Zoorob *et al.*<sup>[26]</sup> demonstrated that quasicrystalline lattices produced by this method can possess photonic band gaps even for materials with low refractive indices. Today, soft lithography is one of the major techniques for the fabrication of micropatterned surfaces. The procedure of soft lithography as part of a rapid prototyping technique was developed by Whitesites *et al.*<sup>[27,28]</sup> and involves the replication of a microstructured template in a soft elastomer. *This thesis presents a systematic study on the fabrication of quasicrystalline micropatterns with arbitrary symmetry using soft lithography. In addition, a procedure is developed to transfer relief structures from poly(dimethylsiloxane) (PDMS) to thin metal layers for optical characterization. The characterization focuses on the influence of the lattice constant on the transmission and reveals a direct relationship to the position of a possible band gap.*

In summary, the motivation of this thesis is to research new methods for the fabrication of complex assembled nano- and microstructures. Non-hexagonal crystalline and quasicrystalline structures are fabricated via colloidal self-assembly and soft lithography. This work, therefore, concentrates on processes which can be used to prepare defined, ordered structures. The simplicity of the methods described in this thesis makes more complex structures easily accessible for a broad range of scientists.

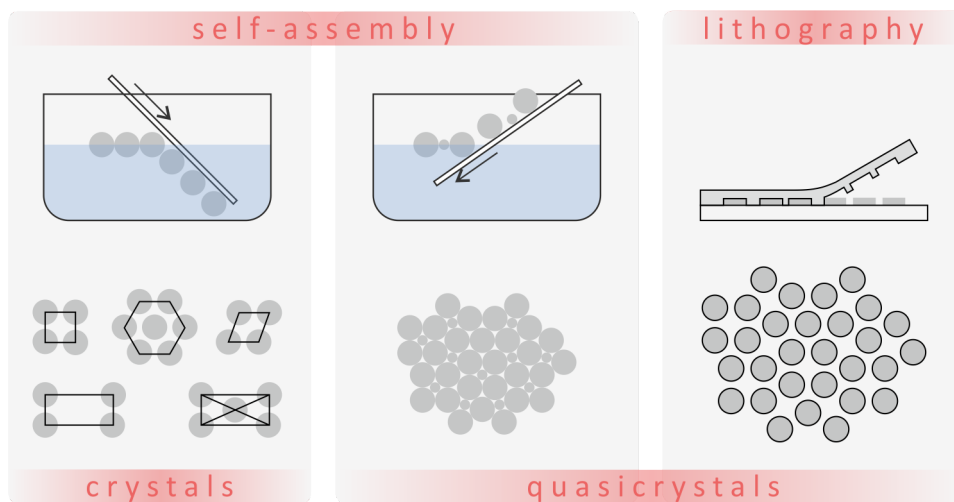


Figure 1.2: Fabrication of ordered, non-hexagonal colloidal assemblies.

**Organization of the thesis.** The thesis is divided into two major parts. In the first part, the reader is introduced to the theoretical frameworks and experimental methods that are relevant for this work. Chapter 2 gives an overview about the synthesis of colloidal particles, stabilization and two-dimensional assembly of colloids, outlines the exception-

ality of quasicrystals and explains the principles of the two major techniques used in this thesis, soft lithography and scanning electron microscopy.

In the second part, chapters 3-6, the results of the individual projects of this work are discussed in more detail (Figure 1.2). These chapters will cover the synthesis of polymer particles (chapter 3), the generation of Bravais lattices by non-close packed colloidal particles (chapter 4), the self-assembly of binary soft colloidal quasicrystals (chapter 5) and the fabrication of quasicrystalline structures with arbitrary symmetry via soft lithography (chapter 6). Finally, the major results of this thesis are summarized in chapter 7 which also gives ideas for future works. The materials and methods used are briefly described in chapter 8.

## References

- [1] Pelesko, J. *Self Assembly: The Science of Things That Put Themselves Together*; CRC Press, 2007.
- [2] Pieranski, P. Two-Dimensional Interfacial Colloidal Crystals. *Physical Review Letters* **1980**, *45*, 569–572.
- [3] Lee, Y. *Self-Assembly and Nanotechnology: A Force Balance Approach*; Wiley, 2008.
- [4] Vogel, N.; Retsch, M.; Fustin, C. A.; Del Campo, A.; Jonas, U. Advances in colloidal assembly: the design of structure and hierarchy in two and three dimensions. *Chemical Reviews* **2015**, *115*, 6265–311.
- [5] Geissler, M.; Xia, Y. Patterning: Principles and Some New Developments. *Advanced Materials* **2004**, *16*, 1249–1269.
- [6] Nemiroski, A.; Gonidec, M.; Fox, J. M.; Jean-Remy, P.; Turnage, E.; Whitesides, G. M. Engineering Shadows to Fabricate Optical Metasurfaces. *ACS Nano* **2014**, *8*, 11061–11070.
- [7] Vogel, N.; Weiss, C. K.; Landfester, K. From soft to hard: the generation of functional and complex colloidal monolayers for nanolithography. *Soft Matter* **2012**, *8*, 4044–4061.
- [8] Romanov, S. G.; Vogel, N.; Bley, K.; Landfester, K.; Weiss, C. K.; Orlov, S.; Korovin, A. V.; Chuiko, G. P.; Regensburger, A.; Romanova, A. S.; Kriesch, A.; Peschel, U. Probing guided modes in a monolayer colloidal crystal on a flat metal film. *Physical Review B* **2012**, *86*, 195145.
- [9] Ai, B.; Yu, Y.; Möhwald, H.; Zhang, G.; Yang, B. Plasmonic films based on colloidal lithography. *Advances in Colloid and Interface Science* **2014**, *206*, 5–16.
- [10] Stelling, C.; Bernhardt, C.; Retsch, M. Subwavelength Etched Colloidal Monolayers: A Model System for Tunable Antireflective Coatings. *Macromolecular Chemistry and Physics* **2015**, *216*, 1682–1688.
- [11] Fenollosa, R.; Meseguer, F. Non-Close-Packed Artificial Opals. *Advanced Materials* **2003**, *15*, 1282–1285.
- [12] Isa, L.; Kumar, K.; Muller, M.; Grolig, J.; Textor, M.; Reimhult, E. Particle lithography from colloidal self-assembly at liquid-liquid interfaces. *ACS Nano* **2010**, *4*, 5665–70.
- [13] Law, A. D.; Buzza, D. M.; Horozov, T. S. Two-dimensional colloidal alloys. *Physical Review Letters* **2011**, *106*, 128302.

- [14] Vogel, N.; Goerres, S.; Landfester, K.; Weiss, C. K. A Convenient Method to Produce Close- and Non-close-Packed Monolayers using Direct Assembly at the Air-Water Interface and Subsequent Plasma-Induced Size Reduction. *Macromolecular Chemistry and Physics* **2011**, *212*, 1719–1734.
- [15] Volk, K.; Fitzgerald, J. P.; Retsch, M.; Karg, M. Time-Controlled Colloidal Superstructures: Long-Range Plasmon Resonance Coupling in Particle Monolayers. *Advanced Materials* **2015**, *27*, 7332–7.
- [16] Quint, S. B.; Pacholski, C. Extraordinary long range order in self-healing non-close packed 2D arrays. *Soft Matter* **2011**, *7*, 3735–3738.
- [17] Vogel, N.; Fernandez-Lopez, C.; Perez-Juste, J.; Liz-Marzan, L. M.; Landfester, K.; Weiss, C. K. Ordered arrays of gold nanostructures from interfacially assembled Au@PNIPAM hybrid nanoparticles. *Langmuir* **2012**, *28*, 8985–93.
- [18] Yan, X.; Yao, J.; Lu, G.; Li, X.; Zhang, J.; Han, K.; Yang, B. Fabrication of non-close-packed arrays of colloidal spheres by soft lithography. *Journal of the American Chemical Society* **2005**, *127*, 7688–9.
- [19] Li, X.; Wang, T.; Zhang, J.; Yan, X.; Zhang, X.; Zhu, D.; Li, W.; Zhang, X.; Yang, B. Modulating two-dimensional non-close-packed colloidal crystal arrays by deformable soft lithography. *Langmuir* **2010**, *26*, 2930–6.
- [20] Malaquin, L.; Kraus, T.; Schmid, H.; Delamarche, E.; Wolf, H. Controlled particle placement through convective and capillary assembly. *Langmuir* **2007**, *23*, 11513–21.
- [21] Khanh, N. N.; Yoon, K. B. Facile organization of colloidal particles into large, perfect one- and two-dimensional arrays by dry manual assembly on patterned substrates. *Journal of the American Chemical Society* **2009**, *131*, 14228–30.
- [22] Rey, M.; Law, A. D.; Buzza, D. M. A.; Vogel, N. Anisotropic Self-Assembly from Isotropic Colloidal Building Blocks. *Journal of the American Chemical Society* **2017**, *139*, 17464–17473, PMID: 29136378.
- [23] Vogel, N.; Viguerie, L. d.; Jonas, U.; Weiss, C. K.; Landfester, K. Wafer-Scale Fabrication of Ordered Binary Colloidal Monolayers with Adjustable Stoichiometries. *Advanced Functional Materials* **2011**, *21*.
- [24] Talapin, D. V.; Shevchenko, E. V.; Bodnarchuk, M. I.; Ye, X.; Chen, J.; Murray, C. B. Quasicrystalline order in self-assembled binary nanoparticle superlattices. *Nature* **2009**, *461*, 964–967.
- [25] Goodwin, J. W.; Hearn, J.; Ho, C. C.; Ottewill, R. H. Studies on the preparation and characterisation of monodisperse polystyrene lattices. *Colloid and Polymer Science* **1974**, *252*, 464–471.

- [26] Zoorob, M. E.; Charlton, M. D. B.; Parker, G. J.; Baumberg, J. J.; Netti, M. C. Complete photonic bandgaps in 12-fold symmetric quasicrystals. *Nature* **2000**, *404*, 740–743.
- [27] Xia, Y.; Whitesides, G. M. Soft Lithography. *Angewandte Chemie International Edition* **1998**, *37*, 550–575.
- [28] Xia, Y.; Whitesides, G. Soft lithography. *Annual Review of Materials Science* **1998**, *28*, 153–184.

## 2 Theory

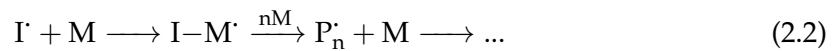
The following chapter gives an overview about the theoretical aspects of colloidal self-assembly and quasicrystals. Colloidal self-assembly starts with the synthesis of suitable particles whereby size and shape control are crucial, as well as colloidal stability. Models which quantitatively describe quasicrystals are also introduced, which relate to a material that is neither a classical crystal nor an amorphous solid. Finally, quasicrystals in soft matter are addressed in more detail.

### 2.1 Essentials of colloidal self-assembly

#### 2.1.1 Synthesis of colloidal particles

The colloids used in this thesis were synthesized by surfactant-free emulsion polymerization. Emulsion polymerizations in general are counted among radical polymerizations, where hydrophobic monomers react with free radicals within submicron polymer droplets dispersed in a continuous aqueous phase. Due to the heterogeneous nature of this process, the reaction mechanism and kinetics are different from other types of radical polymerizations. This chapter provides an overview of the basic mechanisms in radical polymerizations and the special features of emulsion polymerization.

**Free radical polymerization.** Free radical polymerization is a method of polymerization which proceeds via chain growth of monomers. The polymerization involves four different radical reactions: generation of the radical initiator (2.1), propagation via radical addition of monomers (2.2), chain transfer and termination by disproportionation (2.3) and chain termination by radical-radical recombination (2.4).



where I, M,  $\text{P}_n$  signify initiator, monomer and polymer chains with  $n$  monomeric units, respectively.

The monomer conversion in a free radical polymerization first increases, before it steadily levels off as a function of time. After a certain degree of conversion the gel effect (Trommsdorff effect) sets in. Due to an increase of viscosity the diffusion of free radicals is hindered and the bimolecular termination reaction is retarded. This leads to an autoacceleration of the polymerization reaction and a sharp increase of the molecular weight. Although the

polymerization rate is mostly dominated by mobile monomer species, the chain growth can become diffusion-controlled when the reaction temperature drops below the  $T_g$  of the reaction medium. In this case, the polymerization rate continuously decreases at the end of polymerization limiting the achievable conversion.<sup>[1,2]</sup>

**Emulsion polymerization.** Emulsion polymerizations are standard methods for the preparation of latex particles. As compared to free radical polymerizations, emulsion polymerizations benefit from a high reaction velocity and a high molar mass of the polymer. Simultaneously, the reaction mixture features a low viscosity throughout the polymerization due to the aqueous medium. Furthermore, water is well suited to control the heat flux during the synthesis. Schematic illustrations of both a conventional and a surfactant-free emulsion polymerization are shown in Figure 2.1.

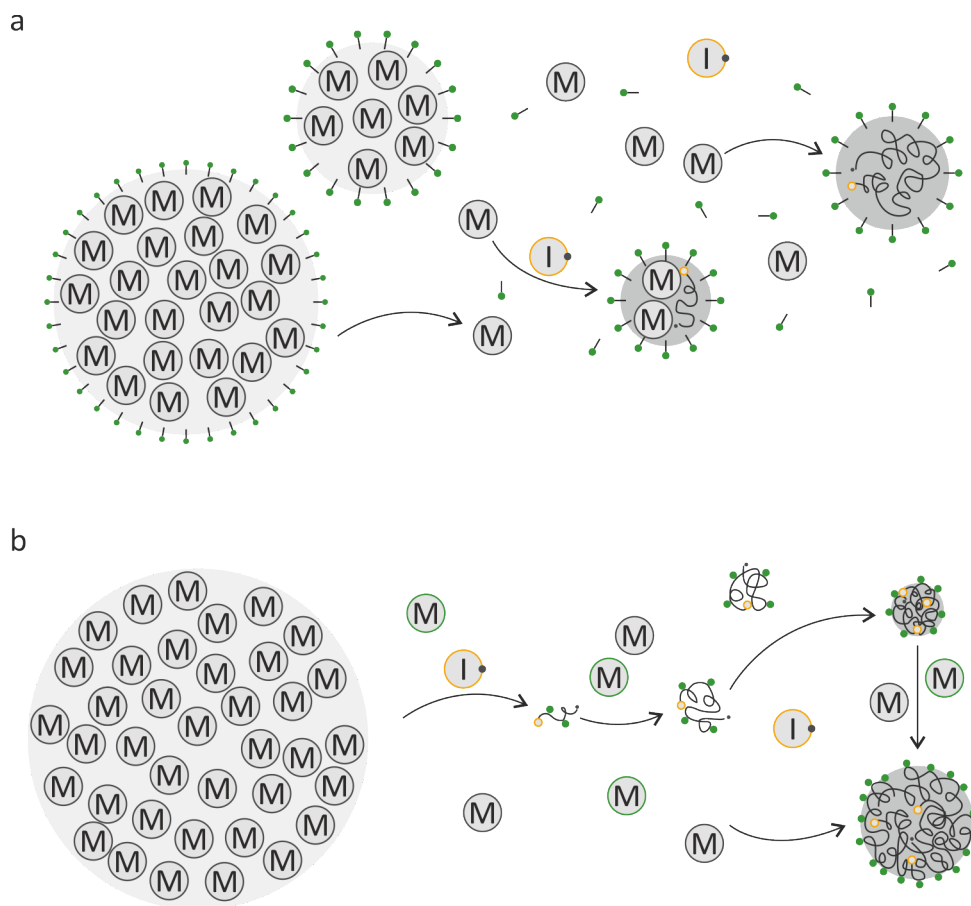


Figure 2.1: Schematic illustrations of emulsion polymerizations. (a) In a conventional emulsion polymerization the monomer and polymer are mainly located in micelles stabilized by surfactants. (b) A surfactant-free emulsion polymerization is characterized by the presence of monomer in large droplets and electrostatic stabilization of the formed polymer by charged groups of the initiator and co-monomer. Adapted by permission from Springer; B. Vollmert, *Polymer Chemistry*, copyright 1973.<sup>[3]</sup>

As emulsion polymerization involves relatively hydrophobic monomers, the polymerization process requires the formation of an oil-in-water emulsion in order to increase the interfacial area. In a conventional emulsion polymerization (Figure 2.1 a) a surfactant is used with a concentration significantly above the critical micelle concentration (cmc). Thereby, the hydrophobic monomer is emulsified in a high number of micelles. Additionally, a low concentration of the monomer is dissolved as individual molecules in the medium and the rest is present as large monomer droplets. The initiation reaction with a water-soluble initiator takes place in the aqueous phase. After degradation of the initiator into radical species, monomer is added to form oligomeric chains. These chains eventually enter a micelle and the polymerization continues quickly in the monomer-rich phase inside. Due to the high ratio of micelles to monomer droplets, the probability is rather low that droplets become polymerization loci. A prerequisite of the models that describe emulsion polymerizations is that only one active radical species is present per micelle. A second radical that enters a micelle stops the polymerization, which only continues upon a new radical entering. During polymerization further monomer diffuses into the micelles and chain growth takes place until all monomer is completely consumed. The outstanding characteristic of emulsion polymerization is the separation of the free radicals into the discrete polymer micelles. This feature reduces the probability of bimolecular termination and chain transfer reactions, yielding a faster polymerization rate and a higher molecular weight.<sup>[2-5]</sup>

The surfactant-free emulsion polymerization shown in Figure 2.1 b was first introduced by Ottewill *et al.*<sup>[6]</sup> In this process no special emulsifier is used. Here, colloidal stability is achieved via electrostatic stabilization with charged initiator molecules and water-soluble co-monomers (Figure 2.2).

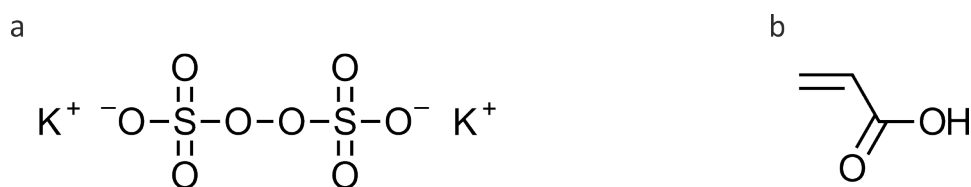


Figure 2.2: Typical initiator and co-monomer used in a surfactant-free emulsion polymerization. (a) Initiator: KPS. (b) Co-monomer: AA.

In contrast, in conventional emulsion polymerization the hydrophobic monomer is distributed in the form of larger monomer droplets while small amounts are molecularly dissolved in the medium. The initiation starts likewise in the aqueous phase. The main difference is the addition of monomer units by the radical species in the aqueous phase until the polymer chain reaches a critical length. Upon this chain length the polymer becomes too hydrophobic and collapses to form polymer particle nuclei. These nuclei can coalesce, yielding stable primary particles which are electrostatically stabilized by charged groups of the initiator and co-monomer at the particle/water interface. Polymerization continues as further monomer diffuses into the hydrophobic particles until

complete consumption.<sup>[7]</sup>

The advantage of surfactant-free emulsion polymerization over conventional emulsion polymerization is that no additional surfactant is present in the final dispersion. For the formation of colloidal crystals this is a crucial aspect, as surfactants can significantly influence attractive and repulsive forces during self-assembly.

### 2.1.2 Colloidal stability

The stability of suspended particles is accepted to originate from the balance of attractive van der Waals to repulsive electrostatic interactions, described by the Deyaguin-Landau-Verwey-Overbeek (DLVO) theory.<sup>[8,9]</sup> Another mechanism of stabilization is steric stabilization which is however not closer explained in this work. The focus of the following chapter will be set on conditions of stability and instability in aqueous colloidal systems.

**Van der Waals forces.** At short distances van der Waals forces are responsible for the attraction between two particles. The three contributions of dipole-dipole (Keesom), dipole-induced dipole (Debye) and induced dipole-induced dipole (London) interactions sum up to the total attractive energy  $E_a$ . All these interactions are attractive and inversely proportional to the sixth power of the interatomic distance  $D$ .

$$E_a = E_{Keesom} + E_{Debye} + E_{London} = -\frac{C_{AB}}{D^6} \quad (2.5)$$

where  $C_{AB}$  is a constant that summarizes the distance-independent contributions, polarizability and dipole moment, of the considered molecules A and B.

For colloidal particles only the London dispersion interactions have to be discussed in more detail. In large assemblies of molecules the individual Keesom and Debye forces offset so that the particles have no net dipole moment nor polarization.

In principle, there are microscopic and the macroscopic approaches to describe the van der Waals attraction between colloids. The latter is more quantitative, though it requires detailed data about the material properties and interaction between the medium and the colloids. As this is not readily available for many systems, the attraction forces are typically predicted by a more qualitative microscopic approach. Here, the attractive energy is calculated as sum of the attraction between all molecules. A remarkable difference between molecules and colloidal particles is that the attractive energy decreases less for colloids with increasing distance  $D$  than between molecules. The van der Waals energy between two spheres ( $E_{sphere-sphere}$ ) with the radii  $R_A$  and  $R_B$  and a distance  $D \ll R_A, R_B$  is given by the Derjaguin approximation.

$$E_{sphere-sphere} = -\frac{A_H}{6D} \cdot \frac{R_A R_B}{R_A + R_B} \quad (2.6)$$

where  $A_H$  is the Hamaker constant with  $A_H = \pi^2 C_{AB} \rho_A \rho_B$ ,  $C$  is the coefficient in the particle–particle pair interaction and  $\rho$  being the number density of the spheres.<sup>[10,11]</sup> The Hamaker constant is an important measure for the description of particle dispersions. For decreasing  $A_H$ , van der Waals attraction decreases which in turn leads to a stabilization of the dispersion.

**Electrostatic forces.** In this work, colloidal particles are used in aqueous suspensions where electrostatic charges are readily generated on the surface of the colloid. Both the adsorption of ions and the dissociation of surface groups impart surface charge. These charges induce an electric field, which in turn attracts counter ions. As a result, the colloidal particles are surrounded by a so called electric double layer.

A theoretical description of this electric double layer is given by Stern. Stern combines the theories of Helmholtz and of Gouy and Chapman. In the Helmholtz model, the counter ions adsorb directly in the form of a molecular layer to the surface. They are rigidly bound and neutralize the surface charges. Helmholtz, therefore, assumed a linear drop of the potential across the layer of counter ions. By contrast, Gouy and Chapman considered the thermal motion of the counter ions. The electric double layer is constituted by a diffuse distribution of counter ions that move away from the surface due to thermal fluctuations. In this model, the potential decays exponentially and can be calculated by the Poisson-Boltzmann equation.

The Stern theory now divides the electric double layer into the inner Stern layer and the outer, diffuse Gouy-Chapman layer (Figure 2.3). The Stern layer is based on the Helmholtz theory, where the counter ions are immobilized on the surface. In the adjacent Gouy-Chapman layer, the spacial distribution of the mobile ions is provided by Poisson-Boltzmann statistics.<sup>[12]</sup>

The Stern layer can be further divided into two parts. Ions that bind specifically to the surface characterize the inner Helmholtz plane. In between these specifically bound ions, water molecules adsorb to the surface with a distinct preferential orientation depending on the surface charge. The subsequent nonspecifically adsorbed counter ions, including their hydration shell, constitute the outer Helmholtz plane. It separates the Stern from the Gouy-Chapman layer and indicates the point where the zeta potential ( $\zeta$  potential) is measured. The zeta potential is the potential difference between the dispersed particle, including the stationary layers of attached ions, and the surrounding medium.

A theoretical description of the Stern model can be composed with the Poisson-Boltzmann equation. Here, the Poisson equation describes the potential distribution in solution and the Boltzmann equation gives information about the spatial distribution of the ions. In general, the Poisson-Boltzmann equation is a partial differential equation of second order, which has numerical solutions for most cases. However, if the model is simplified to an infinitely extended planar surface without separate consideration of the Stern layer,

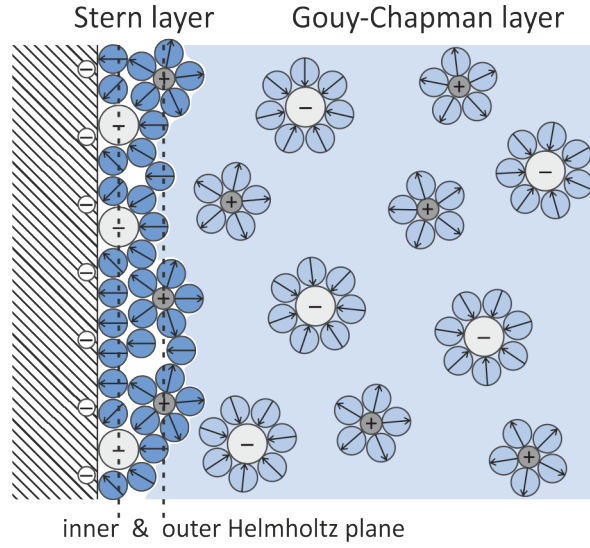


Figure 2.3: Schematic illustration of the Stern model of the electric double layer in a liquid at contact with a negatively charged surface. The Stern model combines the model of Helmholtz, where ions strongly adhere to the charged surface within an inner layer, and the model of Gouy-Chapman, where ions are diffusely distributed within an outer layer. Adapted from Taylor & Francis Group LLC, P.C. Hiemenz *et al.*, Principles of colloid and surface chemistry, 1997.<sup>[13]</sup>

the linearized Poisson-Boltzmann equation can be used. Then, the electric potential  $\psi$  depends on the distance  $D$  from the surface, the surface potential  $\psi_0$ , and  $\kappa$ , which is related to the Debye length  $\lambda_D = \kappa^{-1}$ .

$$\psi = \psi_0 \cdot e^{-\kappa D} \quad (2.7)$$

with

$$\kappa = \sqrt{\frac{2c_0 e^2}{\epsilon \epsilon_0 k_B T}} \quad (2.8)$$

where  $c_0$  is the concentration of electrolytes,  $e$  is the charge of an electron,  $\epsilon$  is the dielectric constant,  $\epsilon_0$  is the permittivity of space,  $k_B$  is the Boltzmann constant, and  $T$  is the temperature. A characteristic shape of the electric potential at a charged surface is shown in Figure 2.4.

The Debye length is a measure of the exponential decay: the electric potential decreases by a factor of  $e^{-1}$  every Debye length. With increasing concentration of electrolytes,  $\lambda_D$  shortens and the exponential decay becomes steeper. Furthermore, the  $\zeta$  potential at the outer Helmholtz plane is affected, as at higher electrolyte concentrations the Gouy-Chapman layer is stronger compressed.<sup>[10,11]</sup>

**DLVO theory.** The DLVO theory explains the stability of colloidal particles by a combination of attractive van der Waals forces and repulsive electrostatic double layer forces. The van der Waals forces, therefore, promote aggregation of the colloids, whereas the

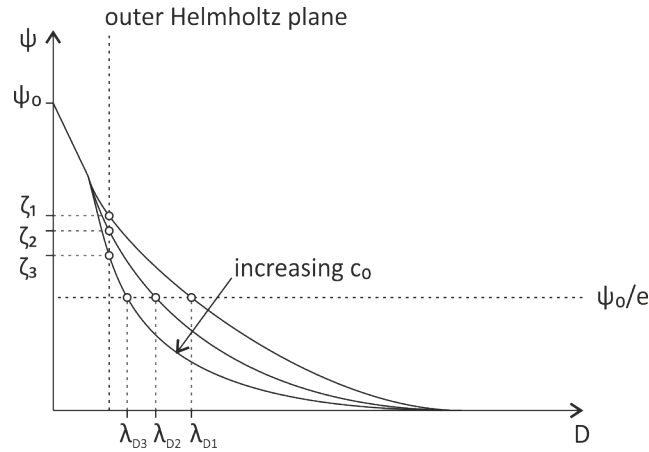


Figure 2.4: Schematic illustration of the progress of the electrostatic potential at charged surfaces. An increasing electrolyte concentration affects both the  $\zeta$  potential and the Debye length  $\lambda_D$  by screening surface charges and thereby lowering the effective electrostatic potential. Adapted from Taylor & Francus Group LLC, P. C. Hiemenez *et al.*, Principles of colloid and surface chemistry, 1997. [13]

electrostatic forces provide colloidal stability. The total interaction energy of two colloidal particles as the sum of the individual contributions is shown in Figure 2.5.

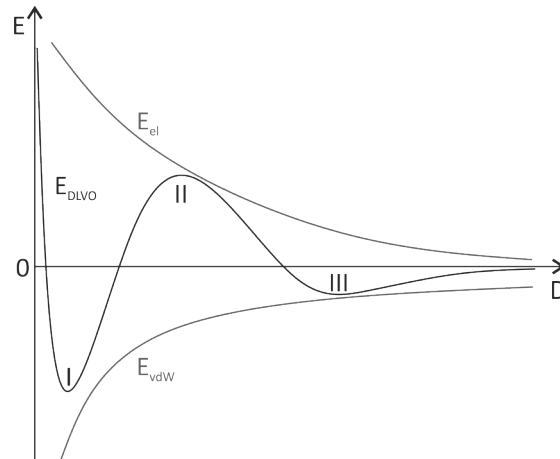


Figure 2.5: Graphical representation of the DLVO theory. The total interaction energy  $E_{DLVO}$  of two particles can be described as a sum of the individual contributions from van der Waals  $E_{vdW}$  and electrostatic energies  $E_{el}$ . Adapted from Taylor & Francus Group LLC, P. C. Hiemenez *et al.*, Principles of colloid and surface chemistry, 1997. [13]

For small distances  $D$  the interaction energy is dominated by the van der Waals attraction. Colloidal particles that approach each other with very short distances are trapped in the primary minimum (I). This state is referred to as aggregation. The energy maximum at intermediate distances (II) is the energy barrier that prevents aggregation. The height of the barrier depends on the surface potential and the electrolyte concentration. A sufficient colloidal stability is typically achieved for values that are significantly larger than the thermal energy of the particles ( $E_{II} > 25 k_B T$ ;  $\zeta$  potential  $> |\pm 40 \text{ mV}|$  and

$c_0 < 10^{-2} M$ ). This energy maximum explains the kinetic stability of colloidal dispersions. Particles have to overcome the energy barrier before they aggregate in the primary minimum. For high electrolyte concentrations, the energy barrier decreases as surface charges are screened until the barrier eventually disappears ( $E_{II} \leq 0$ ) at a critical electrolyte concentration. The addition of electrolytes increases the rate of aggregation so that the dispersion finally becomes unstable. A further feature of the energy-distance plot is the presence of a secondary minimum at long distances (III). This shallow minimum corresponds to a flocculation of the system which is usually reversible.

For two identical particles with a radius  $R$  and surface potentials  $\psi_0 \leq 25 mV - 80 mV$  the DLVO energy can be calculated with the linear approximation of the Poisson-Boltzmann equation.<sup>[10-12]</sup>

$$E_{DLVO} = 2\pi R\epsilon\epsilon_0\psi_0^2 e^{-\kappa D} - \frac{A_H R}{12D} \quad (2.9)$$

### 2.1.3 Colloidal assembly at interfaces

Colloidal assembly at interfaces is not only subject to an interplay of attractive van der Waals and repulsive electrostatic forces. Capillary forces and dipole interactions, that arise from the nature of interfaces, can also act on the particles during their organization.

**Interfacial energy.** The formation of an interface between two materials results in a certain interfacial energy. This energy is proportional to the area of the interface  $A$  and the interfacial tension between the two materials  $\gamma$ .

$$E \propto \gamma \cdot A \quad (2.10)$$

The observation that colloidal particles can become trapped at an interface is driven by an associated decrease in the interfacial energy. Therefore, there must exist a local decrease in energy larger than the thermal energy  $k_B T$ , which leads to the stabilization of the particles at the interface. This energy difference prevents the particles from entering the bulk materials. Figure 2.6 shows a particle  $P$  at the interface of the two materials  $A$  and  $B$ .

The mathematical explanation of the interfacial stabilization is given by Pierenaski.<sup>[14]</sup> The total interfacial energy depends on the interfacial tension between the materials  $\gamma$ , the particle radius  $R$  and the deviation from symmetrical immersion  $z \in [-R; R]$  of the particle with respect to the interface level. The resulting change in energy can be calculated with the three interfacial contributions.

$$\Delta E_{AB} = -\gamma_{AB} \cdot \pi(R^2 - z^2) \quad (2.11)$$

$$\Delta E_{PA} = \gamma_{PA} \cdot 2\pi(R^2 + Rz) \quad (2.12)$$

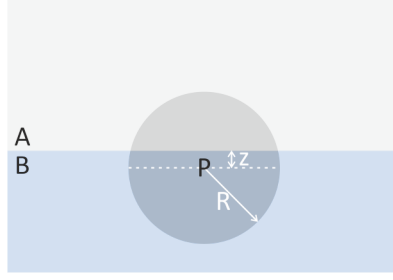


Figure 2.6: Schematic illustration of the geometrical conditions of a particle at an interface of two fluids. Adapted from P. Pieranski, *Physical Review Letters*, 48, 569-572, 1980. Copyright 2017 by the American Physical Society.<sup>[14]</sup>

$$\Delta E_{PB} = \gamma_{PB} \cdot 2\pi(R^2 - Rz) \quad (2.13)$$

The first equation describes the reduction of the interfacial area between *A* and *B* when a particle is introduced to the interface. The latter two equations give the contribution from the newly generated interfaces between the particle and the two materials. The total interfacial energy can be summarized to the following equation

$$E_{total} = E_{total,0} + z^2 \cdot \gamma_{AB} \cdot \pi + z \cdot (\gamma_{PA} - \gamma_{PB}) \cdot 2\pi R + (2\gamma_{PA} + 2\gamma_{PB} - \gamma_{AB}) \cdot \pi R^2 \quad (2.14)$$

Depending on the immersion depth *z*, the change in interfacial energy proceeds as shown in Figure 2.7.

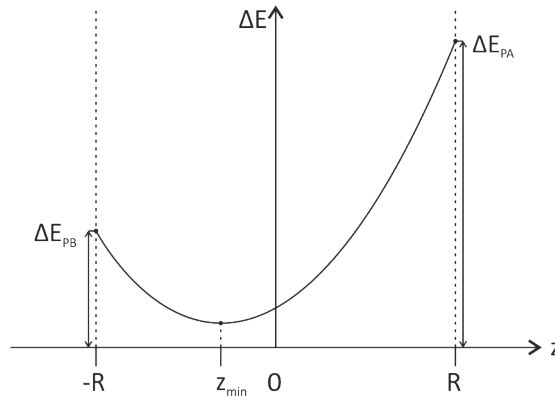


Figure 2.7: Graphical representation of the interfacial energy of a particle at an interface of two fluids. The stabilization of particles at interfaces is the result of an energy barrier that arises from the individual contributions of interfacial tensions in the considered system. Adapted from P. Pieranski, *Physical Review Letters*, 48, 569-572, 1980. Copyright 2017 by the American Physical Society.<sup>[14]</sup>

For  $z \geq R$  and  $z \leq -R$  the particle is removed from the interface and located completely in material *A* or *B*, respectively. These points signify the energy barriers that trap particles at the interface. The minimum interfacial energy, which denotes the preferential position

of a particle, is found at  $z_{min}$ .

$$z_{min} = R \cdot \frac{\gamma_{PB} - \gamma_{PA}}{\gamma_{AB}} \quad (2.15)$$

In this thesis, among others, polystyrene (PS) particles are assembled at the water/air interface. For this system the surface energy barrier can be calculated using the following surface tension values  $\gamma_{air/H_2O} = 72 \text{ mN/m}$ ,  $\gamma_{PS/air} = 35 \text{ mN/m}$  and  $\gamma_{PS/H_2O} = 10 \text{ mN/m}$ .<sup>[15]</sup> In practice though, most surfaces are non-ideal due to e. g. surface roughness (Wenzel<sup>[16]</sup>) or chemical heterogeneity (Cassie and Baxter<sup>[17]</sup>) and applicable values for particles may differ from literature values for macroscopic systems. Nevertheless, the theoretical consideration gives a good estimation for the order of magnitude of the interfacial energy.

For a PS particle with a radius of 250 nm the minimum change in interfacial energy is

$$\Delta E_{total,min} = 1.83 \cdot 10^{-15} \text{ J} (z_{min} = -174 \text{ nm})$$

Furthermore, with the boundary conditions  $z = -R$  and  $z = R$  the energy of a particle in one of the bulk phases can be calculated. From these values the energy barrier can be estimated, that has to be overcome by the particle, when it moves from the interface to one of the bulk phases.

$$\Delta E_{PA} - \Delta E_{total,min} = 2.57 \cdot 10^{-14} \text{ J}$$

$$\Delta E_{PB} - \Delta E_{total,min} = 6.02 \cdot 10^{-15} \text{ J}$$

The results show that the position of a PS particle at the water/air interface is energetically favorable. For this reason, it is possible to create stable, interfacial particle assemblies. The removal of a particle from this interface is prevented by an energy barrier which is in the order of  $10^6 k_B T$ .<sup>[14]</sup>

**Dipole-dipole energy.** Figure 2.8 shows two particles at the water/air interface which are electrostatically stabilized. Due to the different dielectric constants of water and air, the surface charges of the particles are asymmetrically distributed. Whereas water favors the dissociation of functional groups and stabilizes charged surfaces with its high dielectric constant, in air, and generally in media with low dielectric constants, particles are usually uncharged. As a result, the associated dipole moments are perpendicular to the water/air interface. The tendency of the dipole moments to align is hindered by the particles which are trapped at the interface. Consequently, a repulsive force is induced between the particles. This dipole-dipole interaction energy<sup>[18]</sup> is given by

$$E_{dipole} = \frac{\mu_1 \mu_2}{4\pi \epsilon_0 \epsilon_r} \cdot \frac{1}{D^3} \quad (2.16)$$

with

$$\mu = q \cdot l = z \cdot e \cdot \lambda_D \quad (2.17)$$

where  $\mu$  is the dipole moment, defined by the charge  $q$  and the distance  $l$  between the charges that constitute the dipole. For colloidal particles,  $q$  is given by the surface charge of the particles  $z \cdot e$ . The characteristic distance  $l$  between the surface charge and the counter ions in the aqueous solution is described by the Debye length  $\lambda_D$ .

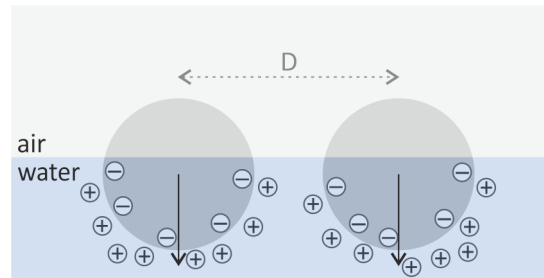


Figure 2.8: Schematic illustration of dipole-dipole interactions between two particles at the water/air interface. An asymmetric charge distribution results from the differences in the dielectric constants in water and air, which induces repulsive forces between the particles. Adapted from *Materials Today*, 13/6, R. McGorty *et al.*, Colloidal self-assembly at an interface, Copyright 2010, with permission from Elsevier.<sup>[19]</sup>

**Capillary forces.** Capillary forces are long-range interactions that occur for particles positioned at the interface of two different fluids. The origin of these forces is the surface tension. In order to minimize the surface energy between the two fluids, particles at interfaces cause a perturbation. The usual flat interface becomes depressed or elevated around the particles. Thereby, the bending of the interface overlaps for two approaching particles creating an attractive or repulsive interaction. In the case of particles with the same nature, capillary forces usually promote a further approach. These capillary interactions can be classified into immersion and flotation forces. Immersion forces occur when the interfacial deformation is a result of the particles' contact angle (Figure 2.9 a), whereas flotation forces are the result of gravity (Figure 2.9 b).

Immersion forces are long-range interactions that occur for particles on a substrate at a liquid interface or in a thin liquid film. In these cases the particles are partially immersed in a liquid, which has a thickness in the order of the particle diameter. The attractive force between the particles arises from the tendency of the liquid to minimize the free liquid surface area. This process is particularly relevant to particle deposition on solid substrates, which is accomplished for the collection of colloidal assemblies from the water/air interface. By contrast, flotation forces are caused by the weight of the particles and are just relevant for particles with a radius larger than  $10 \mu\text{m}$ .<sup>[12,20]</sup>

The Laplace equation of capillarity and the meniscus profile around the particles allow a mathematical calculation of both forces. As the exact solution is very complex, the

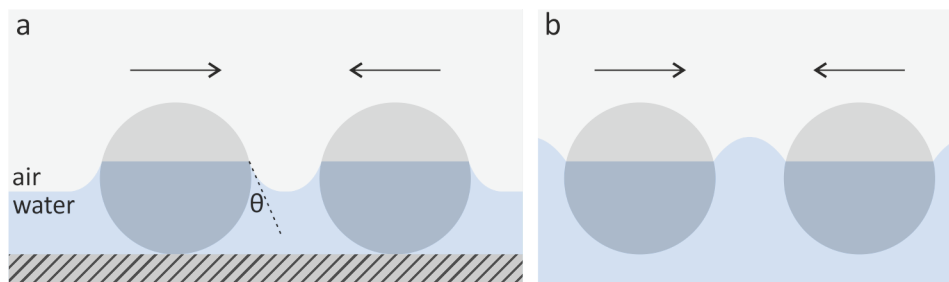


Figure 2.9: Schematic illustration of capillary forces between two particles at an interface. (a) Immersion forces arise from a deformation of the interface due to the contact angle of the particles. (b) Flotation forces are the result of gravitation that deforms the interface for large particles. Adapted from *Materials Today*, 13/6, R. McGorty *et al.*, *Colloidal self-assembly at an interface*, Copyright 2010, with permission from Elsevier.<sup>[19]</sup>

following expressions will only show the major dependencies of the forces.

$$F_{immersion} \propto \frac{R^2 \cdot \gamma}{D} \quad (2.18)$$

$$F_{flotation} \propto \frac{R^6}{\gamma \cdot D} \quad (2.19)$$

Both forces show the same functional dependence on the interparticle distance  $D$  but very different dependencies on the particle radius  $R$  and the surface tension  $\gamma$ .<sup>[21]</sup>

**Two-dimensional colloidal crystallization.** Monodisperse colloidal particles are able to assemble into two-dimensional crystals. A controlled formation of these assemblies is a key component for the fabrication of functional surfaces and thin film devices. They have various applications in lithography<sup>[22–25]</sup>, optics<sup>[26]</sup>, photonics<sup>[27]</sup>, and high-density data storage<sup>[28]</sup> to name but a few. Established preparation methods can be divided into direct assembly of colloidal particles on solid substrates, and liquid interface-mediated assembly. As this work is mostly based on liquid interface-mediated assembly, this process will be discussed further.

The interface-mediated process can be characterized by certain inherent features. As the particles exclusively assemble at an interface, the resulting crystal will be two-dimensional - the formation of multilayers is not possible. The liquid interface also enables a lateral mobility of the particles. Particles with a reasonable electrostatic stabilization can assemble into a minimum free energy position. Furthermore, the crystallization process can be influenced by the composition of the subphase. Addition of surfactant can push particles at the interface together while the change of the pH can introduce charges on the particle surface.

The crystallization in interface-mediated processes is driven by short-range van der Waals attraction and long-range electrostatic and dipole repulsion. A well-balanced presence of

these forces is a prerequisite for the formation of colloidal crystals with a high degree of order. The electrostatic repulsion is responsible for the energy barrier that prevents aggregation. For this reason, particles with high electrostatic stabilization possess a higher mobility and form assemblies with a lower free energy of conformation. Particles with an insufficient repulsion come into contact easily and cannot detach anymore as a result of van der Waals attraction. Consequently, the composition of the subphase is a crucial parameter as the pH and the electrolyte concentration strongly influence the electrostatic interparticle repulsion.

A standard technique for interface-mediated assembly is particle crystallization in a Langmuir trough (Figure 2.10 a). In this technique, the particles are spread at the water/air interface before moving barriers reduce the free interfacial area. In the beginning, the area reduction does not affect the surface pressure until the individual particles come into contact. Further compression leads to densely packed particle domains and finally, the interface is completely covered with a colloidal monolayer. At this point, the surface pressure begins to rise steeply as continued barrier movement causes buckling and collapse of the monolayer. The transfer of the monolayer can be accomplished manually by the withdrawal of a substrate from the subphase through the monolayer in a flat angle, by the slow lowering of the water level so that the monolayer is deposited on a substrate, or by vertical Langmuir-Blodgett transfer.<sup>[29]</sup>

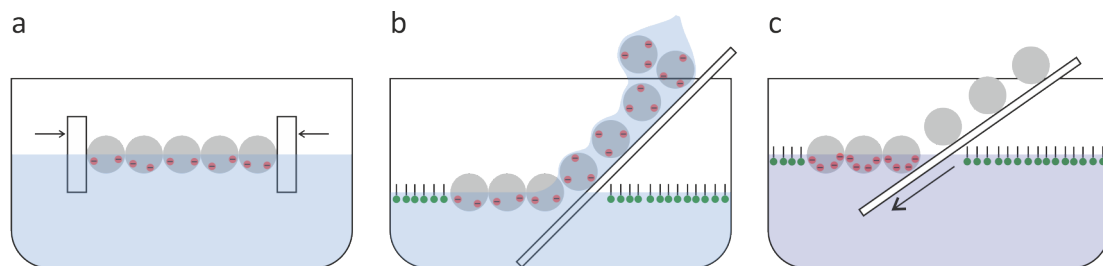


Figure 2.10: Schematic illustration of interface-mediated assembly techniques. (a) Langmuir trough, (b) direct interfacial self-assembly established by Vogel *et al.*<sup>[30]</sup>, (c) interfacial self-assembly established by Retsch *et al.*<sup>[31]</sup>.

A direct assembly technique at the water/air interface is reported by Vogel *et al.*<sup>[30]</sup> This technique is similar to the approach of Weekes *et al.*<sup>[32]</sup> and is based on directly spreading a colloidal solution at the interface (Figure 2.10 b). In brief, the colloidal suspensions are prepared in a 1:1 mixture of water and ethanol and applied via a tilted glass slide to the water surface. Thereby, the crystallization process is enhanced by the presence of sodium dodecyl sulfate (SDS) in the subphase. The formed monolayer can be collected on various substrates by withdrawal under a shallow angle.

Another simple and straightforward technique was introduced by Retsch *et al.*<sup>[31]</sup> (Figure 2.10 c). In principle, the technique is a two-step procedure. In the first step an aqueous colloidal suspension is spin-coated onto a functionalized glass slide. This yields individually distributed particles on the glass slide. Subsequently, the slide is slowly immersed

into the subphase, whereby colloidal crystallization occurs at the three-phase contact line. Upon immersion the particles detach from the glass surface and a freely floating monolayer is formed. Thereby, the assembly process is supported by the presence of SDS in the subphase and a suitable pH.

## 2.2 Quasicrystals

Quasicrystals can be classified somewhere between glasses and crystals. Whereas amorphous structures feature a completely random distribution, crystals are periodic. This means that in crystals there exists a unit cell which tells us the exact arrangement of particles. By simple translation of this unit cell the entire space can be filled with the crystalline structure. Quasicrystals have the exceptional characteristic that though they are aperiodic they feature long-range orientational order. For this reason, a certain unit cell cannot be defined but rather is infinitely large.

### 2.2.1 Symmetries in periodic and non-periodic systems

Classical crystals were defined by the International Union of Crystallography prior to 1992 as *"a substance in which the constituent atoms, molecules, or ions are packed in a regularly ordered, repeating three-dimensional pattern."* Thus, crystals possess a periodic lattice that allows only a limited set of rotational symmetries. This can be understood by imagination of a two-dimensional plane that has to be covered with tiles with no voids nor overlaps. In this scenario only triangles, squares, hexagons or distortions of these shapes will match. This selection of shapes arises from the fact that only those tiles can be assembled around a vertex using an integer number: six triangles, four squares or three hexagons and the corresponding number of their distortions (Figure 2.11).

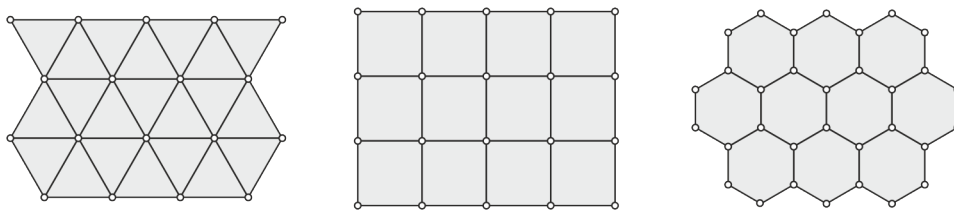


Figure 2.11: Tilings of a two-dimensional plane with triangular, square and hexagonal units. Adapted from J. Dubois, *Useful Quasicrystals*, World Scientific, 2005.<sup>[33]</sup>

For this reason, the rotational symmetry in such classical crystals is restricted to two-, three-, four- and six-fold symmetry. Any vertex in such a tiling can be deduced from any other vertex by an appropriate translation of the single tiles. This two-dimensional lattice can be expressed as an infinite array of periodically arranged points whereby the points coordinates are given by the following equation.

$$r = n_1 a_1 + n_2 a_2 \quad (2.20)$$

where  $n$  is an integer and  $a$  is a unit vector which defines the translation in the lattice from the origin to the position  $r$ . Therefore, it is possible to fill the entire space by translation of the corresponding unit cell.

In contrast, other shapes like pentagons or heptagons cannot cover a two-dimensional plane without any voids or overlaps (Figure 2.12). If a tiling of regular pentagons is considered for coverage of a two-dimensional lattice, a translation of a lattice point along a unit vector  $a$  does not yield a periodic lattice. The local arrangement of the translated point would require distances between points smaller than  $a$ , which contradicts a periodicity for the unit vector  $a$ . However, taking the new shortest distance will again lead to the same conclusion that there is an even smaller distance. This conclusion is also valid for symmetries higher than six. Octagonal, decagonal or dodecagonal symmetries do not lead to a periodically tiled plane.<sup>[33]</sup>

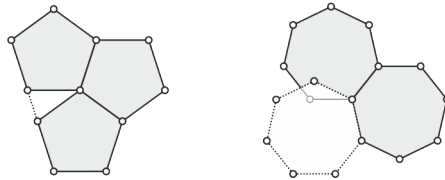


Figure 2.12: Tilings of a two-dimensional plane with pentagons (voids) or heptagons (overlaps). Adapted from J. Dubois, *Useful Quasicrystals*, World Scientific, 2005.<sup>[33]</sup>

## 2.2.2 Quasicrystal models

**$N$ -dimensional description of quasicrystals.** As quasicrystalline structures cannot be described as two-dimensional arrays of periodically arranged points, the mathematical definition is more complex. Quasiperiodicity is expressed by embedding the quasicrystalline structure in higher dimensional periodic space. Thereby, a quasicrystalline structure in  $n$  dimensions is obtained by a projection from a periodic structure in  $m$  dimensions ( $m > n$ ).<sup>[34,35]</sup>

A simple example of the  $N$ -dimensional description of quasicrystals is the generation of the *Fibonacci chain*. The Fibonacci chain is a one-dimensional quasicrystal constituted by two different elements. The points of this one-dimensional quasicrystal can be described by a projection from a two-dimensional square lattice onto a line. Thereby, all points of the square lattice can be described by  $r = n_1 a_1 + n_2 a_2$ , as it is periodic. The line, on which the square lattice is projected, has a slope  $\tau^{-1}$  with  $\tau = (1 + \sqrt{5})/2$  being the golden ratio (Figure 2.13).

The projection is accomplished for all points of the square lattice that lie within the dimension of a unit cell ( $\Delta = \sqrt{2}a$ ) around the dashed line (gray area). The result is a sequence of long ( $L$ ) and short ( $S$ ) elements with  $L/S = \tau$  on this line. These elements form the Fibonacci chain: a one-dimensional, non-periodic lattice with long-range order.

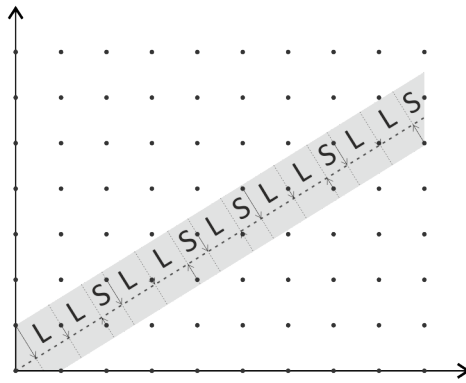
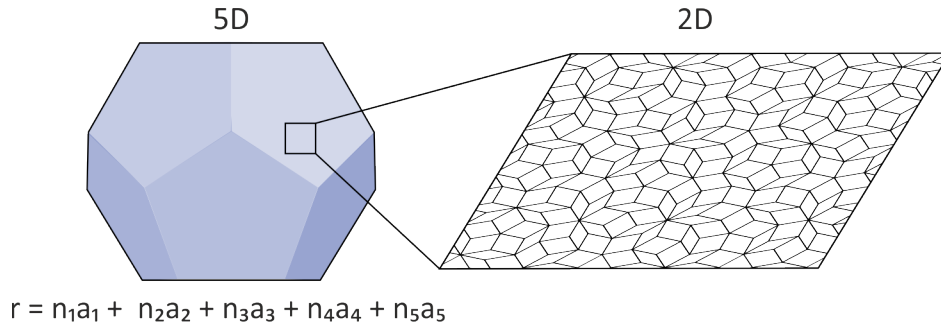


Figure 2.13: Generation of a Fibonacci chain by the projection of a two-dimensional square lattice on a line with the slope  $\tau^{-1}$ . Adapted from A. Piróth and J. Sólyom, *Fundamentals of the Physics of Solids: Volume 1*, Springer, 2007.<sup>[36]</sup>

As a consequence of the projection, each point of the Fibonacci chain is described by two indices of the square lattice. Hence, a one-dimensional quasicrystal can be described in two-dimensions.<sup>[37,38]</sup>

Two-dimensional quasicrystals require a description in even higher dimensional space. The *Penrose tiling* with five-fold rotational symmetry consists of a pair of tile shapes: a fat and a skinny rhombic tile. This tiling is the results from a projection of a segment of five-dimensional space onto a plane (Figure 2.14).<sup>[34]</sup>



$$\mathbf{r} = n_1\mathbf{a}_1 + n_2\mathbf{a}_2 + n_3\mathbf{a}_3 + n_4\mathbf{a}_4 + n_5\mathbf{a}_5$$

Figure 2.14: Generation of a Penrose tiling by the projection of a segment of five-dimensional periodic space onto a two-dimensional plane.

**Deflation method.** A special class of quasicrystals has the property of self-similarity. Quasicrystals of this class show the most symmetrical structure. These quasicrystals cannot only be constructed by projection from higher dimensional space, but due to their self-similarity they can also be generated by deflation using a substitution rule. These rules are self-similarity transformations, in which the original elements are subdivided into segments which in turn form another quasicrystal that is scaled down by a distinct factor.

In the one-dimensional case, the Fibonacci chain is an example of a self-similar quasicrystal. As described above the Fibonacci chain is a sequence of  $L$  and  $S$  segments with

$L/S = \tau$ . The elements of this sequence can be substituted by  $L \rightarrow LS$  and  $S \rightarrow L$  to create another, longer Fibonacci chain (Figure 2.15).<sup>[39]</sup> Mathematically the substitution can be expressed as

$$\begin{pmatrix} L \\ S \end{pmatrix} \rightarrow \begin{pmatrix} 1 & 1 \\ 1 & 0 \end{pmatrix} \begin{pmatrix} L \\ S \end{pmatrix} \quad (2.21)$$

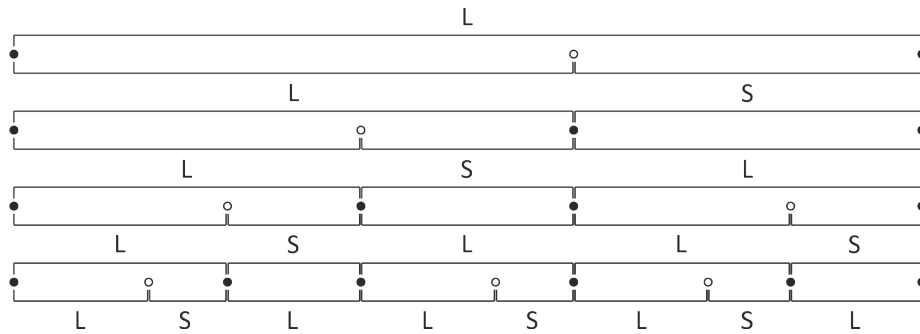


Figure 2.15: Generation of a Fibonacci chain by deflation with the substitutions rules  $L \rightarrow LS$  and  $S \rightarrow L$ . Adapted from D. Levine and P.J. Steinhardt, *Physical Review B*, 34, 596-616, 1986. Copyright 2017 by the American Physical Society.<sup>[40]</sup>

In two-dimensional space, the Penrose tiling is an example of a self-similar quasicrystalline structure (Figure 2.16 a). Figure 2.16 b shows the deflation rules for the Penrose tiling. The original tiles are decorated by smaller rhombic tiles scaled down by the factor  $\tau$ . Thereby the fat rhombus is substituted by three fat and two skinny smaller rhombi, and the skinny rhombus is substituted by two fat and two skinny rhombi. This decoration on the original tiles additionally represents matching rules, that constrain the packing of adjacent tiles during deflation. The interplay of substitution and matching rules allows filling space with a quasicrystalline structure by repeated deflation.<sup>[40]</sup>

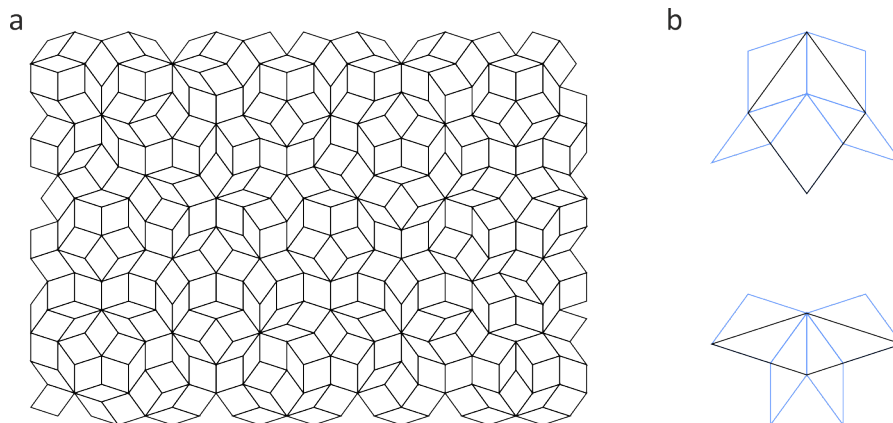


Figure 2.16: (a) Penrose tiling with 5-fold symmetry, (b) substitution rules for the Penrose tiling. Adapted from D. Levine and P.J. Steinhardt, *Physical Review B*, 34, 596-616, 1986. Copyright 2017 by the American Physical Society.<sup>[40]</sup>

**Generalized dual method.** The generalized dual method (GDM) can be used to construct quasicrystals with arbitrary symmetry.<sup>[41]</sup> The algorithm is considerably easier to implement for the calculation of quasicrystalline structures than projection methods from higher dimensional space which can be considered equal to the GDM.<sup>[42]</sup>

The general principle of the GDM is depicted in Figure 2.17. In the first step a number of sets of parallel lines are defined, whereby the number of sets equals the degree of symmetry in the quasicrystalline lattice. These lines are overlaid in a way so that a grid is created where only two lines intersect at once. In a certain radius around the center of the grid all line intersections are determined. Thereby, each intersection defines a rhombic tile in the final quasicrystalline lattice. The definition of the tiles is based on a calculation including the coordinates of the intersection and the direction vectors of the initially generated parallel line sets. As each intersection divides space into four regions, the result of the calculation are four vertices for each intersection defining the rhombic tile. A combination of all generated tiles creates a dense rhombic tiling without translational symmetry. A more detailed description of the GDM is given by Socolar *et al.*<sup>[41]</sup>

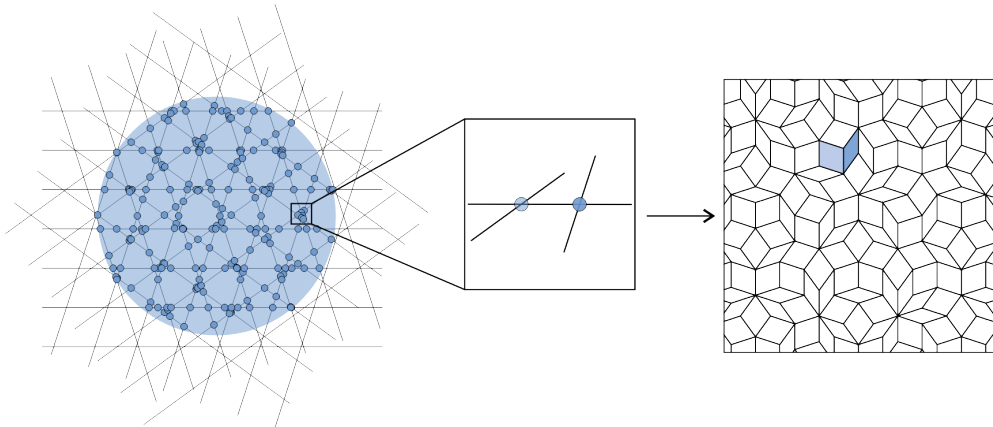


Figure 2.17: Schematic illustration of the general principle of the GDM. Adapted from J. E. S. Socolar *et al.*, *Physical Review B*, 32, 5547-5550, 1985. Copyright 2017 by the American Physical Society.<sup>[41]</sup>

### 2.2.3 Soft quasicrystals

The existence of quasicrystals was suggested in 1984 by Shechtman *et al.* They reported that rapidly cooled alloys with certain compositions can show sharp diffraction peaks with symmetries not allowed for crystals.<sup>[43]</sup> After this discovery, quasicrystalline structures have been observed in various complex metallic alloys.<sup>[44-46]</sup> Whereas these first quasicrystals were only metastable, later many stable quasicrystalline species were discovered and contributed significantly to the advances of quasicrystalline research.<sup>[47-50]</sup> All these alloys have in common that they mostly form quasicrystalline phases with icosahedral or decagonal symmetry.

Besides this first wave of discoveries of intermetallic quasicrystals, in the last decade also an increasing number of soft matter quasicrystals has been found. Metallic quasicrystals show their quasicrystalline order on the atomic length scale. Therefore, they are able to interact with electrons. By contrast, soft matter quasicrystals feature length scales where the propagation of light takes place. This enables new applications based on self-assembled nanomaterials that take advantage of the quasiperiodicity, such as complete and isotropic photonic band-gap materials. Hence, these structures can be exploited to manufacture optical materials with new and improved physical properties.

Soft quasicrystals on the molecular and nanoscale have been reported in various systems, including dendrimers<sup>[51]</sup>, star polymers<sup>[52]</sup>, block-copolymers<sup>[53–55]</sup>, mesoporous silica<sup>[56]</sup>, perovskites<sup>[57]</sup>, metal-organic coordination networks<sup>[58]</sup>, ferrocenecarboxylic acid<sup>[59]</sup>, fullerene<sup>[60]</sup> and nanoparticles<sup>[61–64]</sup>. Most of these systems show a dodecagonal (12-fold) symmetry in plane and a periodic stacking of these planes in three dimensional space.

The variety of soft quasicrystals suggests that there is a common generic mechanism for the formation of quasicrystalline order. However, the origin of their stability and the role of energetic and entropic contributions is still controversial. This question has been addressed by numerous theoretical works which predict quasicrystalline structures in computer-based simulation under different conditions. One of the simplest models is reported by Dotera *et al.* who proposed a two-length scale interaction that yields quasicrystals with 10-, 12-, 18- and 24-fold symmetry.<sup>[65]</sup> Based on this theoretical framework, the formation of quasicrystals can be either realized by a one-component or a two-component system. In a one-component system the two length scales are constituted by core-shell particles where the sizes of the core and the shell are the relevant parameters (Figure 2.18 a). In a two-component system binary particle mixtures are applied where the individual diameters of the particles represent the two different lengths (Figure 2.18 b).

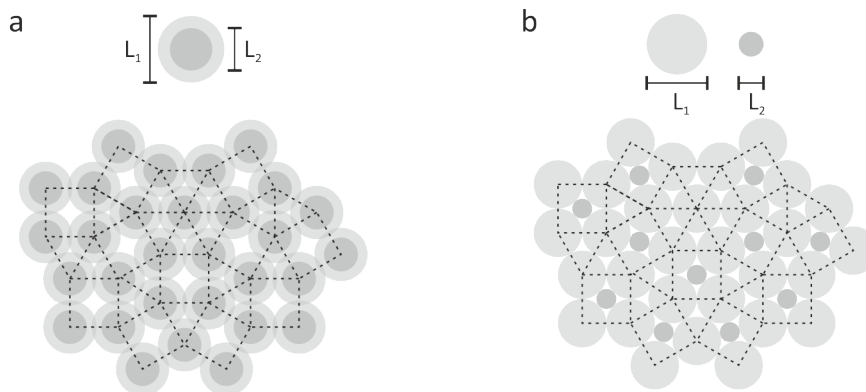


Figure 2.18: (a) One-component system, (b) two-component system.

This thesis focuses on the assembly of two-component systems. The first quasicrystals from a binary particle mixture were reported by Talapin *et al.*<sup>[61]</sup> They observed the self-

assembly of quasicrystalline structures with dodecagonal symmetry from different binary mixtures of nanoparticles, where the formation of the quasicrystalline phase was only observed for a distinct size ratio. If the ratio of the particle diameter matched  $\gamma = d_S/d_L \approx 0.43$ , a structure with dodecagonal symmetry was formed (Figure 2.19 a). For values of  $\gamma$  above or below 0.43 typically periodic  $AlB_2$  or  $CaB_6$  structures are found (Figure 2.19 b/c).

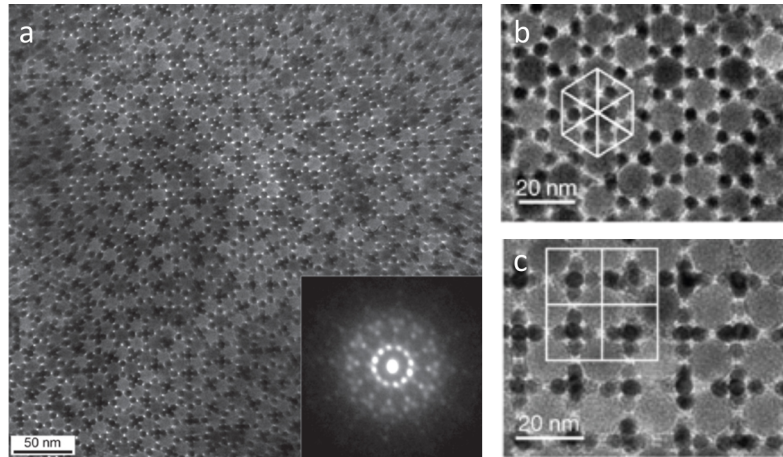


Figure 2.19: TEM images of superlattices self-assembled from 13.4 nm  $Fe_2O_3$  and 5 nm Au nanoparticles. (a) Quasicrystalline structure with 12-fold rotational symmetry, (b)  $AlB_2$  type structure, (c)  $CaB_6$  type structure. Adapted by permission from Macmillan Publishers Ltd: Nature<sup>[61]</sup>, copyright 2009

In a more detailed study of binary nanoparticle superlattices, it was shown that the formation of quasicrystalline structures in such systems is based on nanoparticles with different ligands. It is stated that the self-assembly is not merely driven by entropy, but rather favored kinetically due to a local free energy minimum. During the self-assembly, a ligand exchange between the nanoparticles takes place, which affects the thermodynamics of the system. As the ligand exchange requires the expense of energy, the energetic penalty for a densely packed structure might be too high. Thus, superlattices with lower packing densities such as the dodecagonal quasicrystal form driven by kinetics.<sup>[66]</sup> This work will investigate if similar structures can also be assembled by polymer particles which are significantly larger than the nanoparticles used by Talapin.

### 2.3 Preparation and investigation of nano- and microstructures

In addition to colloidal self-assembly, this thesis also relies on soft lithography to prepare ordered structures. Both concepts, self-assembly and soft lithography, yield structures with features in the nano- to micrometer range which are typically characterized by scanning electron microscopy (SEM).

### 2.3.1 Soft Lithography

Soft lithography is based on the manufacture of a template comprising the relief structures which are designed with computer-aided design (CAD) software and subsequently converted into high-resolution transparencies that work as photomasks. For the generation of the template a photoresist is selectively exposed to UV light. The non-cross-linked material can then be removed by dissolving in an appropriate solvent.

The herein used SU-8 50 is an epoxy-based negative photoresist. It is a 69 % solution of the main component EPON®SU-8 in  $\gamma$ -butyrolactone. EPON®SU-8 is a highly functionalized molecule bearing eight epoxy groups (Figure 2.20). The photoresist contains furthermore the photo acid generator (PAG) triarylsulfonium hexafluoroantimonate and 4-Methyl-1,3-dioxolan-2-one.

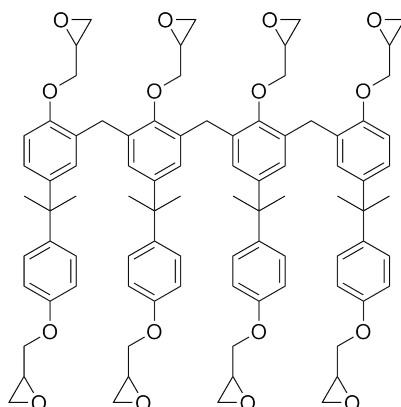


Figure 2.20: Chemical structure of EPON®SU-8.

The mechanism of UV light induced cross-linking of the photoresist is based on cationic ring opening polymerization (ROP). The cross-linking proceeds in two steps, (1) during UV illumination a strong acid is formed, (2) which in turn initiates the thermally driven cross-linking.

Under UV exposure and in the presence of the proton donator 4-Methyl-1,3-dioxolan-2-one, triarylsulfonium hexafluoroantimonate is converted into fluoroantimonic acid ( $\text{HSbF}_6$ ) (Figure 2.21). This strong Lewis acid acts as initiator for the cationic ROP. As triarylsulfonium hexafluoroantimonate can also undergo UV induced side reactions that do not yield initiator (Figure 2.22) it is crucial to adjust the light dose in order to minimize the rate for alternative reaction paths.

Cross-linking via ROP is initiated by  $\text{HSbF}_6$  in the subsequent so-called post exposure bake (PEB) step where the photoresist is cured at elevated temperatures (Figure 2.23). In the first reaction step an epoxide group of EPON®SU-8 is protonated by  $\text{HSbF}_6$  which promotes the nucleophilic addition of a second SU-8 molecule via its hydroxy group. This leads to the opening of the epoxide ring. Deprotonation of the addition product regenerates the catalyst  $\text{HSbF}_6$  and enables numerable repetitions of the reaction cycle

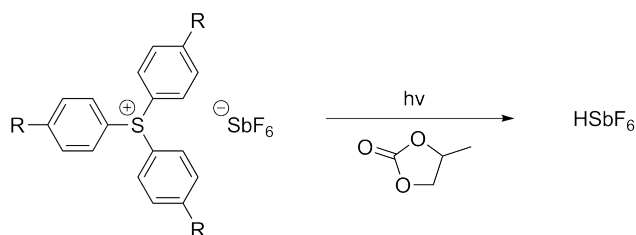


Figure 2.21: Formation of fluoroantimonic acid by photochemical reaction of triarylsulfonium hexafluoroantimonate.

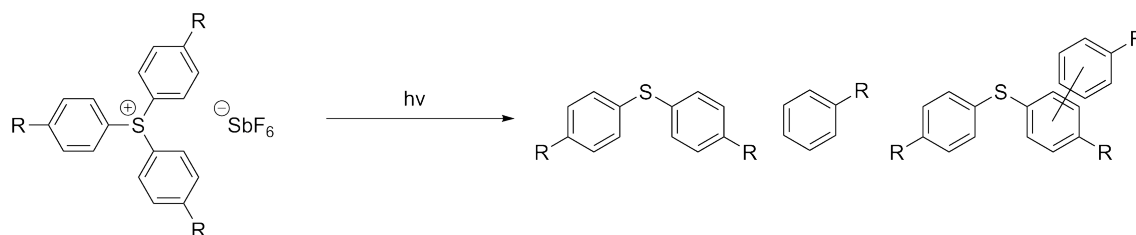


Figure 2.22: Photochemical side reaction of triarylsulfonium hexafluoroantimonate.

yielding a highly cross-linked material.

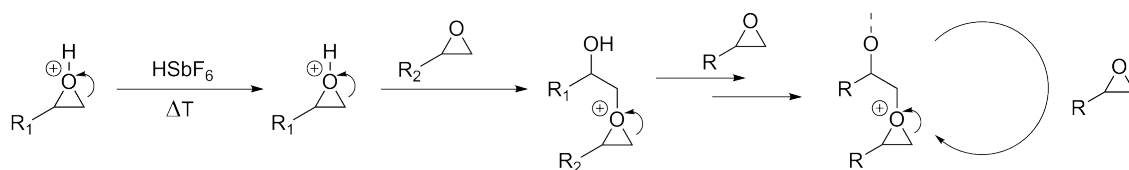


Figure 2.23: Mechanism of photoinitiated ROP of EPON®SU-8.

The molding material used in this thesis for replication is poly(dimethylsiloxane) in form of Sylgard®184 from Dow Corning. Sylgard®184 is a combination of the base polymer poly(dimethylsiloxane) with vinyl end groups and the curing agent hydrogenmethyl siloxane with a dihydrogenhexachloroplatinat(IV) ( $\text{H}_2\text{PtCl}_6$ ) complex as catalyst (Figure 2.24).

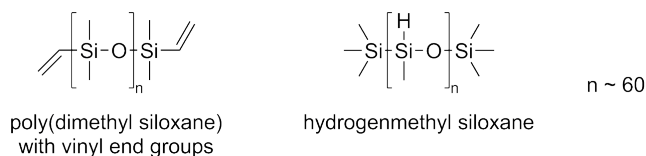


Figure 2.24: Chemical structures of Sylgard®184 base polymer (left) and curing agent (right).

Cross-linking is accomplished by hydrosilylation of the vinyl end groups of the base polymer at elevated temperatures and in the presence of a platinum catalyst. The mechanism of the catalyzed hydrosilylation is based on oxidative addition and reductive elimination steps. The oxidative addition of hydrogenmethyl siloxane via Si-H to the platinum base polymer complex is followed by migratory insertion of the vinyl group into the Pt-H

bond. The resulting complex undergoes reductive elimination by formation of the Si-C bond and regeneration of the platinate catalyst (Figure 2.25).<sup>[67]</sup>

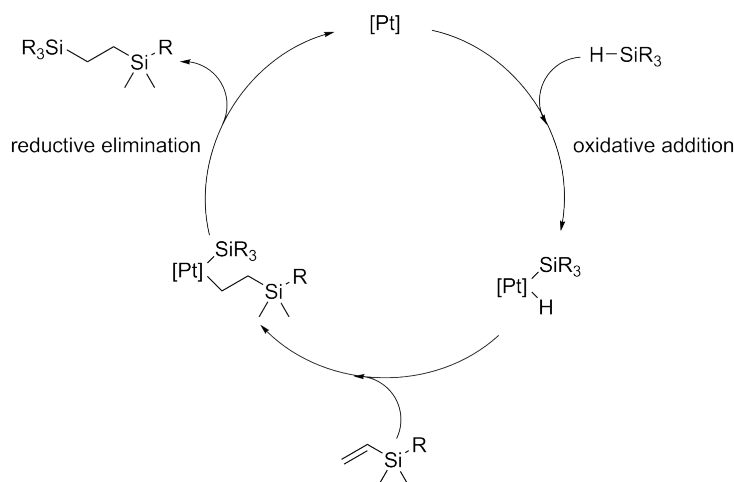


Figure 2.25: Mechanism of platinum catalyzed hydrosilylation of alkenes.

The curing process usually results in a homogeneous elastomeric material and volume shrinking is negligible ( $\sim 1\%$ ).<sup>[68]</sup>

In order to activate the PDMS surface air or oxygen plasma is applied. In this process active oxygen species bind to surface sites all over the material (Figure 2.26). The so introduced silanol group form e. g. covalent Si-O-Si or Si-O-Ti bonds when brought into contact with another surface bearing silanol or titanol groups.



Figure 2.26: Activation of PDMS by plasma treatment.

### 2.3.2 Scanning electron microscopy

SEM is a sophisticated technique for high resolution depictions of surfaces and analysis of their elemental composition. The principle of electron microscopy is comparable to traditional light microscopy. Whereas in light microscopy photons are used for imaging, SEM is based on the raster scan irradiation of a specimen with a focused electron beam.<sup>[69,70]</sup> The advantages of SEM opposite to conventional light microscopy are an immense depth of field and high resolution in the order of several nanometers. Furthermore, compared to transmission electron microscopy (TEM) sample preparation is less time consuming and images obtained by SEM can selectively show the surface structure of the specimen by using different contrast mechanisms. For standard depictions secondary electrons and backscattered electrons are most frequently used. For analysis of the material's composition the generated x-rays can be detected by an energy or wavelength dispersive x-ray spectrometer. Additionally, the detection methods can be combined so that a complex

evaluation of the information of the sample and elucidation of the microscopic structure are possible.<sup>[70]</sup>

The primary reason for developing electron microscopes was to improve the resolution of microscopes. The resolution power, which is the minimum distance  $d$  between two adjacent object points that can still be imaged separately, is still one of the major aspects of a microscope. Historically, it was Ernst Abbe who showed that the resolution power of optical microscopes is limited by the wavelength of visible light.<sup>[69]</sup> The following equation states that the minimum distance between two objects which can be resolved is approximately half the wavelength used for depiction.

$$d = \frac{\lambda}{2NA} \quad (2.22)$$

where  $\lambda$  is the wavelength and  $NA$  is the numerical aperture.

Electrons show both particle and wave characteristics. Based on this wave-particle duality introduced by Louis de Broglie, the wavelength  $\lambda$  of an electron can be described by its particle momentum  $p$  and the Planck's constant  $h$ .<sup>[71]</sup>

$$\lambda = \frac{h}{p} \quad (2.23)$$

For electron microscopy the electrons are accelerated through a potential drop  $U$  imparting the momentum to the electron whereby the final kinetic energy of the electron has to be equal to the potential energy of the electron when emitted from the cathode. Thereby the electron wavelength can also be related to the accelerating voltage  $U$ . By increasing the accelerating voltage the wavelength of the electrons is decreased.

$$\lambda = \frac{h}{\sqrt{2m_e eU}} \quad (2.24)$$

where  $m_e$  is the mass of an electron and  $e$  is the charge of an electron. As the wavelength of electrons is several magnitudes smaller than the one of visible light, electron microscopy led to a significant improvement of the resolution power. Nevertheless, it has to be stated that the best resolution achieved with SEM is strongly dependent on the quality of instrumental components, e. g. lens aberration, and always poorer than the theoretically calculated resolution. Furthermore, the resolution is affected by the analyzed material and especially for polymers it is difficult to achieve excellent results. This is due to their sensitivity to high electron irradiation and the fact that they show in general low contrast.<sup>[69]</sup>

**Electron interaction** In scanning electron microscopy signals are generated by the interaction product of the incident primary electrons and the surface layer of the specimen.

Thereby the dimension of the interaction volume in the specimen depends on the probe energy. When accelerated electrons enter a bulk specimen both inelastic and elastic scattering occurs at the atoms. Inelastic scattering is referred to electrons that interact with atomic electrons generating secondary electrons (SE) whereas elastic scattering results from electrostatic interactions with atomic nuclei so-called backscattered electrons (BSE). SE can be further divided into SE1 which are the direct product of the interaction between the primary electron beam and the atomic electrons, SE2 that result from interactions between BSE and atomic electrons and SE3 which are generated when BSE hit chamber components outside the specimen.

The inelastic scattering process is characterized by a loss of energy during the interaction while elastic means that the energy of the primary electron remains ideally constant. When electrons are scattered in an inelastic manner they gradually lose portions of their kinetic energy until they are eventually “at rest” and incorporated into the sample. The depth how far such electrons can penetrate the specimen defines the pear-shaped interaction volume. In addition to the above-mentioned initial energy of the electrons, the atomic number of the constituent elements and the density of the sample also affect the interaction volume. Generally, the interaction volume decreases with increasing atomic number. On the other hand the volume increases with acceleration voltage as high energetic electrons need more inelastic scattering processes to lose their complete energy and are less prone to inelastic collisions (Figure 2.27).

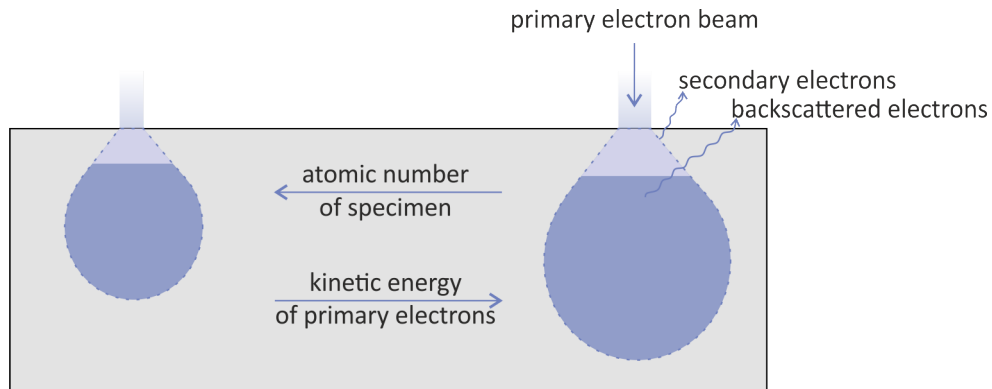


Figure 2.27: Schematic illustration of the excitation volume in dependence on the kinetic energy of incident electrons and the atomic number of specimen.

Backscattered electrons result from primary electrons that interact with the electric field of an atomic nucleus. They are deflected by the so called Rutherford scattering and thus move in parabolic trajectories. The intensity of the deflection increases with the atomic number of the involved atoms and decreasing distance between electron and nucleus. The energy of primary electrons that are elastically scattered in this way remains approximately the same. Electrons that are subject to strong interactions can significantly change their trajectory so that they can even be guided back on their original path and leave the specimen again.<sup>[69]</sup>

Secondary electrons are the product of inelastic scattering processes. These processes refer to the interaction of the primary electrons with electrons of the atom shell. The scattering follows the principle of conservation of energy so that the primary incident electron's loss of energy is retrieved at some atomic electrons participating in the inelastic collision. The energy intake is split into potential energy to release the electron from the nucleus and kinetic energy that enables those so-called secondary electrons to move through the specimen. As the initial kinetic energy is in the order of maximum 50 eV, subsequent inelastic scattering events that let these electrons come to rest are very likely and their mean free path is only a few nanometers. For this reason only secondary electrons created close to the specimen's surface are able to escape into the vacuum. Detectors that selectively depict the surface structure to yield images with small details exploit the small escape depth. On one hand the yield of secondary electrons can be adjusted by the energy of the incident beam as inelastic scattering and thereby creation of secondary electrons is inversely dependent on the kinetic energy of primary electrons. On the other hand the angle between incident electrons and the surface plays an important role. The lowest SE yield is obtained for perpendicularly incident electrons and is increasing with the angle between electron beam and the surface-normal. The reason for this dependence is depicted in Figure 2.28.

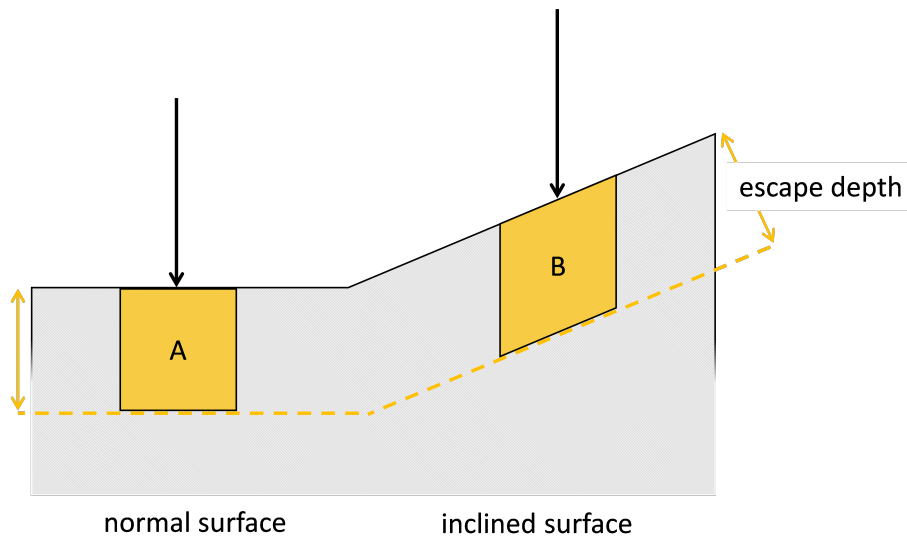


Figure 2.28: Schematic illustration of escape depth of secondary electrons.

When the electron beam incides on an inclined surface (B) the volume from which secondary electrons can escape defined by the escape depth is higher than for a normal surface (A). This orientation dependence is responsible for the three-dimensional impression of images acquired by SE detectors. The so-called edge-effect occurs at the edges of a sample. As the interaction volume borders to a larger surface area more SEs escape into the vacuum and contribute to the signal. For this reason edges of a sample always appear brighter in SE detection modes.<sup>[69,70]</sup>

**Instrumentation.** The arrangement of the basic components of an SEM is illustrated in Figure 2.29. Electrons are emitted from a thermionic or a field-emission source and accelerated by a high potential. A system of electromagnetic lenses forms the electron beam and focuses it on the surface of a sample whereby the electron probe scans the sample line by line. Interactions between the beam and the sample are detected electronically and form a signal which is displayed as brightness modulation on a screen.<sup>[69]</sup>

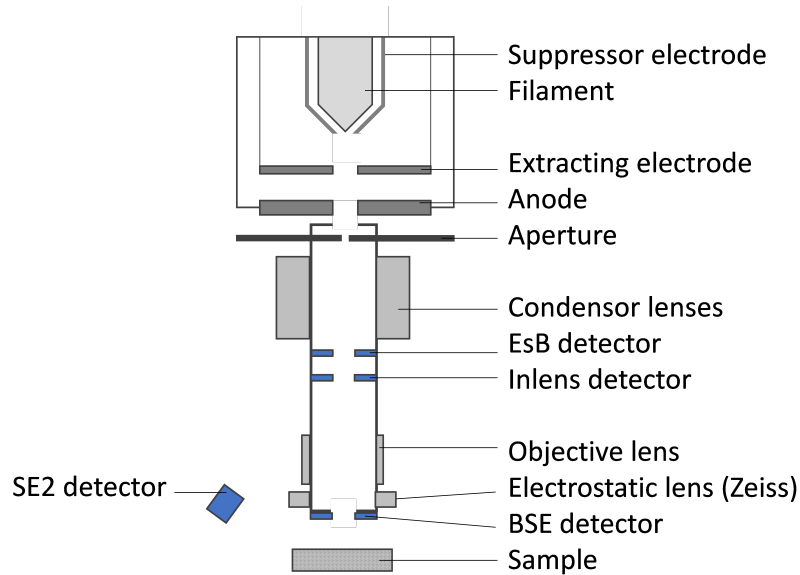


Figure 2.29: Schematic illustration of a scanning electron microscope.

**Electron source.** The electron source is located at the top of the microscope column. Electrons can be generated in different types of cathode systems which are classified into thermal emission and field-emission electron guns. Subsequently the electrons are accelerated between the cathode and anode. A typical acceleration potential of a scanning electron microscope lies between 100 V and 30 kV. Thermal electron guns consist of a tungsten or LaB<sub>6</sub> filament that is heated electrically so that electrons receive sufficient thermal energy to surmount the work function of the filament/vacuum interface and leave the cathode. The limitations of thermionic emission lie in the energy spread of the electrons and the coherence of the current density. Field-emission electron guns are used in a high-resolution scanning electron microscope as the diameter of the produced electron beam is in the order of 5 to 10 nm. The principle of such systems is electron extraction through quantum tunneling, which occurs when a high electric field is applied to metal surfaces. Thereby, electrons are emitted from the tip of a tungsten single crystal placed opposite to a positively biased extracting electrode. A further acceleration electrode behind the extracting electrode is used to adjust the energy of the electron beam. An advantage of field-emission systems is that the emitter is not heated resulting in a low energy spread (chromatic aberration) and thus a better resolution. Schottky-emission electron guns are based on the Schottky-emission effect. A heated tungsten single crystal

coated with ZrO constituting the emitter is exposed to a high electric field. This leads to a diffusion of ZrO towards the tip of the cathode. The reduced work function of ZrO provides a selective emission of electrons from the tip. The overall construction closely resembles the field-emission systems except an additional build in suppressor that shields thermoelectrons that would disperse the energetic distribution of the electron beam. An advantage of Schottky-emitters is the both constant and larger electron beam current due to the increased temperature that prevents gas adsorption at the emitter. For this reason the electric field requirements and the demanding vacuum requirements of a conventional field-emission gun can be reduced. However a higher energy spread than for field-emission guns has to be accepted.<sup>[69,70]</sup>

**Electromagnetic lenses.** In order to regulate and guide the accelerated electrons through the beam path electromagnetic lenses with rotationally symmetric magnetic fields are used in an electron microscope. Usually, in a scanning electron microscope several condenser lenses and a final objective lens are used. The electron beam created by the electron gun has a certain diameter, which has to be reduced in order to form a focused electron probe that is required for a reasonable resolution. For this purpose condenser lenses are installed that adjust the beam current and scale down the beam diameter. The magnetic field  $B$  exerts a Lorentz force  $F$  on electrons with a charge  $e$  that enter the magnetic field off-axis with a velocity  $v$ . This force is perpendicular to both  $B$  and  $v$  and is described by

$$F = evB \cdot \sin\theta \quad (2.25)$$

Due to this deflection the electron obtains a component of velocity in a circumferential direction  $v_c$  around the optical axis. It therefore experiences another force perpendicular to  $v_c$  and  $B$  which pulls the electron towards the axis. The combination of these forces yields a helical trajectory of the electrons.<sup>[71]</sup>

The final objective lens guides the electron beam on the sample and is therefore a crucial component that determines the resolution. When the electron beam passes through the lens the beam does not converge exactly on one point but blurs which is called aberration. The total aberration of a lens is the sum of spherical and chromatic contribution and degrades the resolving power of a lens. Spherical aberration (Figure 2.30 (a)) refers to the effect that electrons entering the magnetic lens field are inhomogeneously bent. Thereby the further off axis the electron is, the more strongly it is bent back toward the axis. For this reason a point object is imaged as a disk of finite size which limits the ability to magnify details and eventually reduces the resolution. The error due to spherical aberration  $\delta_s$  which describes the image diameter of a point is dependent on the semiangle of collection of the lens  $\beta$  and the spherical aberration coefficient of the particular lens  $C_s$ .<sup>[71]</sup>

$$\delta_s = 2C_s\theta^3 \quad (2.26)$$

Chromatic aberration (Figure 2.30 (b)) relates to a lens defect arising from electrons with different energies and hence different wavelengths. Usually the variation of the electron energy in the emitted electron beam is very small so that chromatic aberration could be ignored for the illumination system. However, when the electrons interact with the specimen by inelastic scattering the detected electrons cover a wide range of energies which leads to blurring of points into disks as described for spherical aberration above. A measure for the blurring by chromatic aberration is given by

$$\delta_c = C_c \cdot \frac{\Delta E}{E_0} \cdot \beta \quad (2.27)$$

where  $C_c$  is the chromatic aberration coefficient of the lens,  $\Delta E$  is the energy loss of the electrons,  $E_0$  is the initial electron energy and  $\beta$  is the semiangle of collection of the lens. Thereby the energy loss of the electron is dependent on the specimen thickness so that chromatic aberration increases with increasing thickness.<sup>[69,71]</sup>

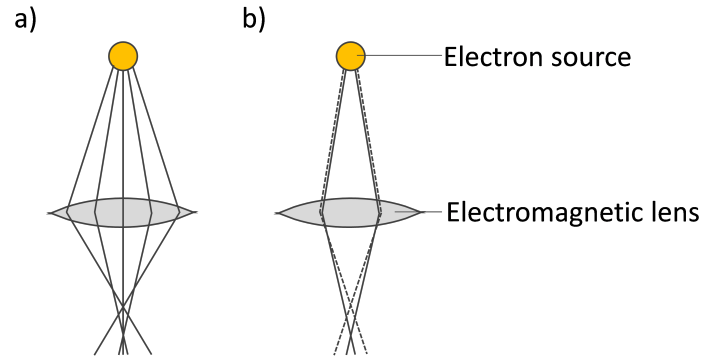


Figure 2.30: Schematic illustration of (a) spherical aberration and (b) chromatic aberration.

Astigmatism is a result of inhomogeneous magnetic fields that affect the helical trajectory of the electrons. As the polepieces in magnetic lenses cannot be produced perfectly cylindrically symmetrical throughout the hole where the electron travel through local variations of the magnetic field are present. Furthermore, apertures that are not precisely centered around the axis or contamination deflect the electron beam and hence contribute to astigmatism. The relationship between the distortion of the image due to astigmatism and the maximum difference in focus induced by astigmatism  $\Delta f$  is

$$\delta_a = \beta \cdot \Delta f \quad (2.28)$$

Though, astigmatism can be easily corrected by means of stigmators that introduce a compensating field. By using quadrupole or octupole electromagnetic coils it is possible

to generate an oval field instead of a circularly symmetrical field to compensate for the elliptical field distribution of an astigmatic lens.<sup>[72]</sup> As both condenser lenses and the objective lens are affected by astigmatism there are stigmators installed in the illumination system and imaging system.<sup>[71]</sup>

**Detectors.** The inlens detector is preferably used to detect SE that were generated near the spot center. Due to their low energy they have origin only from a slight penetration depth and contribute to the selective depiction of the sample surface. The detector is located above the objective lens inside the beam path. The electrostatic field that moderates the energy from the electron beam simultaneously works as collector and accelerator for newly generated electrons on the sample surface. These electrons are post-accelerated towards the inlens detector. High signal-to-noise ratios are realized by small working distances. This enables acquiring high-resolution pictures with the inlens detector as only SE1 contribute to the measured signal.<sup>[70]</sup>

The SE2 detector is also known as Everhardt-Thornley detector. It is installed at the chamber wall, thus viewing the sample sidewise. The secondary electrons that escape the sample possess energies of up to only 50 eV. In order to detect these electrons with high efficiency there is a collector in form of a grid electrode installed. By applying a certain positive potential in the range of 300 V the resulting electric field is able to attract low energy electrons so that independent on their moving direction they are drawn towards the detector. In the case that the collector potential is set to negative potentials secondary electrons with low energies are deflected. High energetic backscattered electrons are hardly influenced by the electric field and only those leaving the sample in direction of the SE2 detector contribute to the signal. With this setting an image is generated solely by backscattered electrons showing a high topographical contrast but lacking of surface morphology. Restrictions of the SE2 detector concern primary electrons with low energies and small working distances which both reduce the efficiency of detection. A small working distance leads to shadowing as electrons are likely to be attracted by the electrostatic field of the lens, though the critical distance is dependent on the type of instrument used. This reduces the yield of electrons so that there exists a critical potential where the signal to noise ratio determines the application. However, it is often reasonable to operate the SE2 detector at the bottom limit as more surface information can be gathered in this mode. At higher potentials thin top layers might be completely penetrated by the electron beam thus losing information about the surface structure.<sup>[69]</sup>

The BSE detector is positioned directly beneath the objective lens and is operated as a reverse-biased diode in which high energetic backscattered electrons induce electron-hole pairs which eventually are detected as current flow. An outer thin metal layer absorbs electrons with low energies. The BSE detector is separated in different segments. The signals of the segments are recorded individually and can be combined. Thus the detector can be operated either in a mode that shows the compositional or the topographical

contrast of the specimen. The principle of both modes is shown in Figure 2.31. They are based on addition or subtraction of the signals of the different detector segments whereby particular information of the sample are enhanced.<sup>[69]</sup>

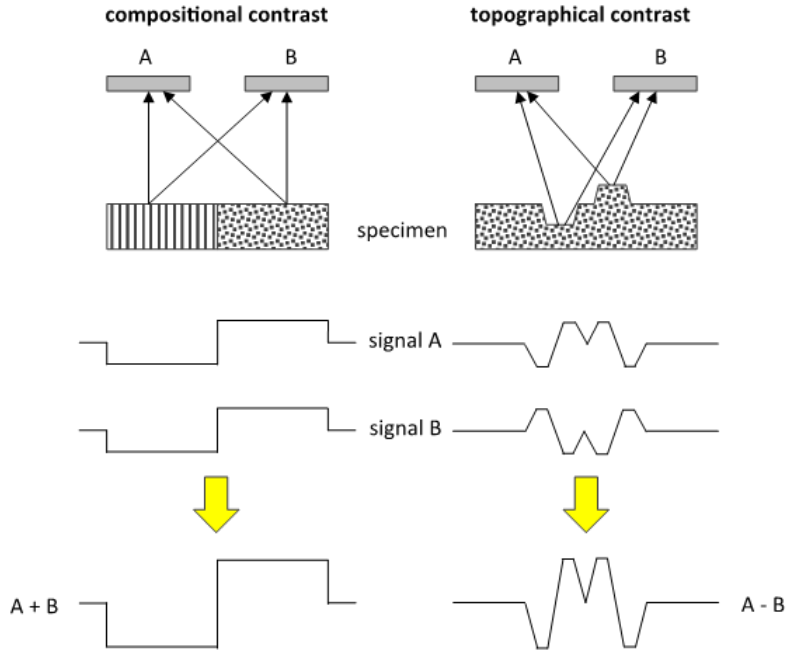


Figure 2.31: Generation of compositional and topographical contrast.

The energy selective backscattered electrons (EsB) detector is a modification of the conventional BSE detector consisting of a scintillator instead of a semi-conductor. In contrast to the BSE detector it is not positioned beneath the objective lens but inside the microscope column. For this reason the EsB detector does not influence the field of the objective lens and analysis with small working distances is possible. Furthermore, it selectively detects BSE that escape the specimen in a sharp angle referred to the primary electron beam and thereby takes advantage of the beam booster at low acceleration potentials. BSE entering the column are accelerated toward the EsB detector so that even for low energies a good efficiency is obtained. Another feature of the EsB detector is a grid electrode to which a potential can be applied in order to detect only BSE within a certain range of kinetic energy while others are deflected by the resulting electric field. By means of this setting the compositional contrast can be either enhanced or supplied with surface specific information originating from SE that also partly reach the detector.<sup>[69]</sup>

All detectors have in common that the collected electrons strike a scintillator whereby their kinetic energy is used to emit photons. A light pipe guides the photons to a photomultiplier where photoelectrons are generated and amplified finally producing an electronic signal that is proportional to the number of collected electrons.<sup>[69,70]</sup>

## References

- [1] Matyjaszewski, K.; Davis, T. P. *Handbook of radical polymerization*; John Wiley & Sons, 2003.
- [2] Chern, C. *Principles and Applications of Emulsion Polymerization*; Wiley, 2008.
- [3] Immergut, E.; Vollmert, B. *Polymer Chemistry*; Springer Berlin Heidelberg, 2012.
- [4] Harkins, W. D. A General Theory of the Mechanism of Emulsion Polymerization. *Journal of the American Chemical Society* **1947**, *69*, 1428–1444.
- [5] Smith, W. V.; Ewart, R. H. Kinetics of Emulsion Polymerization. *The Journal of Chemical Physics* **1948**, *16*, 592–599.
- [6] Goodwin, J. W.; Hearn, J.; Ho, C. C.; Ottewill, R. H. Studies on the preparation and characterisation of monodisperse polystyrene latices. *Colloid and Polymer Science* **1974**, *252*, 464–471.
- [7] Hansen, F. K.; Ugelstad, J. Particle nucleation in emulsion polymerization. I. A theory for homogeneous nucleation. *Journal of Polymer Science: Polymer Chemistry Edition* **1978**, *16*, 1953–1979.
- [8] Derjaguin, B.; Landau, L. Theory of the stability of strongly charged lyophobic sols and the adhesion of strongly charged particles in solutions of electrolytes. *Acta Physicochimica USSR* **1941**, *14*, 633–662.
- [9] Verwey, E.; Overbeek, J. *Theory of the Stability of Lyophobic Colloids: The Interaction of Sol Particles Having an Electric Double Layer*; Elsevier Publishing Company, 1948.
- [10] Butt, H.-J.; Graf, K.; Kappl, M. *Physics and Chemistry of Interfaces*; Wiley-VCH Verlag GmbH & Co. KGaA, 2004.
- [11] Tadros, T. *Colloid Stability*; Wiley-VCH Verlag GmbH & Co. KGaA, 2006.
- [12] Li, Q.; Jonas, U.; Zhao, X. S.; Kappl, M. The forces at work in colloidal self-assembly: a review on fundamental interactions between colloidal particles. *Asia-Pacific Journal of Chemical Engineering* **2008**, *3*, 255–268.
- [13] Hiemenz, P.; Rajagopalan, R. *Principles of Colloid and Surface Chemistry, Third Edition, Revised and Expanded*; Undergraduate Chemistry: A Series of Textbooks; Taylor & Francis, 1997.
- [14] Pieranski, P. Two-Dimensional Interfacial Colloidal Crystals. *Physical Review Letters* **1980**, *45*, 569–572.
- [15] Sheppard, E.; Tchekdjian, N. Monolayer studies. *Journal of Colloid and Interface Science* **1968**, *28*, 481 – 486.

- [16] Wenzel, R. N. RESISTANCE OF SOLID SURFACES TO WETTING BY WATER. *Industrial & Engineering Chemistry* **1936**, *28*, 988–994.
- [17] Cassie, A. B. D.; Baxter, S. Wettability of porous surfaces. *Transactions of the Faraday Society* **1944**, *40*, 546–551.
- [18] Atkins, P.; De Paula, J. *Physikalische Chemie*; Wiley-VCH-Lehrbuchkollektion 1; Wiley-VCH, 2013.
- [19] McGorty, R.; Fung, J.; Kaz, D.; Manoharan, V. N. Colloidal self-assembly at an interface. *Materials Today* **2010**, *13*, 34 – 42.
- [20] Binks, B.; Horozov, T. *Colloidal Particles at Liquid Interfaces*; Cambridge University Press, 2006.
- [21] Kralchevsky, P. A.; Nagayama, K. Capillary interactions between particles bound to interfaces, liquid films and biomembranes. *Advances in Colloid and Interface Science* **2000**, *85*, 145 – 192.
- [22] Nemiroski, A.; Gonidec, M.; Fox, J. M.; Jean-Remy, P.; Turnage, E.; Whitesides, G. M. Engineering Shadows to Fabricate Optical Metasurfaces. *ACS Nano* **2014**, *8*, 11061–11070.
- [23] Romanov, S. G.; Vogel, N.; Bley, K.; Landfester, K.; Weiss, C. K.; Orlov, S.; Korovin, A. V.; Chuiko, G. P.; Regensburger, A.; Romanova, A. S.; Kriesch, A.; Peschel, U. Probing guided modes in a monolayer colloidal crystal on a flat metal film. *Physical Review B* **2012**, *86*, 195145.
- [24] Vogel, N.; Weiss, C. K.; Landfester, K. From soft to hard: the generation of functional and complex colloidal monolayers for nanolithography. *Soft Matter* **2012**, *8*, 4044–4061.
- [25] Li, Y.; Cai, W.; Duan, G. Ordered Micro/Nanostructured Arrays Based on the Monolayer Colloidal Crystals. *Chemistry of Materials* **2008**, *20*, 615–624.
- [26] Yang, S. M.; Jang, S. G.; Choi, D. G.; Kim, S.; Yu, H. K. Nanomachining by colloidal lithography. *Small* **2006**, *2*, 458–75.
- [27] Ai, B.; Yu, Y.; Möhwald, H.; Zhang, G.; Yang, B. Plasmonic films based on colloidal lithography. *Advances in Colloid and Interface Science* **2014**, *206*, 5–16.
- [28] Cumpston, B. H. et al. Two-photon polymerization initiators for three-dimensional optical data storage and microfabrication. *Nature* **1999**, *398*, 51.
- [29] Vogel, N.; Retsch, M.; Fustin, C. A.; Del Campo, A.; Jonas, U. Advances in colloidal assembly: the design of structure and hierarchy in two and three dimensions. *Chemical Reviews* **2015**, *115*, 6265–311.

- [30] Vogel, N.; Goerres, S.; Landfester, K.; Weiss, C. K. A Convenient Method to Produce Close- and Non-close-Packed Monolayers using Direct Assembly at the Air-Water Interface and Subsequent Plasma-Induced Size Reduction. *Macromolecular Chemistry and Physics* **2011**, *212*, 1719–1734.
- [31] Retsch, M.; Zhou, Z.; Rivera, S.; Kappl, M.; Zhao, X. S.; Jonas, U.; Li, Q. Fabrication of Large-Area, Transferable Colloidal Monolayers Utilizing Self-Assembly at the Air/Water Interface. *Macromolecular Chemistry and Physics* **2009**, *210*, 230–241.
- [32] Weekes, S. M.; Ogrin, F. Y.; Murray, W. A.; Keatley, P. S. Macroscopic Arrays of Magnetic Nanostructures from Self-Assembled Nanosphere Templates. *Langmuir* **2007**, *23*, 1057–1060.
- [33] Dubois, J. *Useful Quasicrystals*; World Scientific, 2005.
- [34] Kramer, P.; Neri, R. On periodic and non-periodic space fillings of  $E^m$  obtained by projection. *Acta Crystallographica Section A* **1984**, *40*, 580–587.
- [35] Duneau, M.; Katz, A. Quasiperiodic Patterns. *Physical Review Letters* **1985**, *54*, 2688–2691.
- [36] Piróth, A.; Sólyom, J. *Fundamentals of the Physics of Solids: Volume 1: Structure and Dynamics*; Fundamentals of the Physics of Solids; Springer Berlin Heidelberg, 2007.
- [37] Elser, V. The diffraction pattern of projected structures. *Acta Crystallographica Section A* **1986**, *42*, 36–43.
- [38] Elser, V. Indexing problems in quasicrystal diffraction. *Physical Review B* **1985**, *32*, 4892–4898.
- [39] Hoggatt, V. *Fibonacci and Lucas numbers*; Houghton Mifflin mathematics enrichment series; Houghton Mifflin, 1969.
- [40] Levine, D.; Steinhardt, P. J. Quasicrystals. I. Definition and structure. *Physical Review B* **1986**, *34*, 596–616.
- [41] Socolar, J. E. S.; Steinhardt, P. J.; Levine, D. Quasicrystals with arbitrary orientational symmetry. *Physical Review B* **1985**, *32*, 5547–5550.
- [42] Gahler, F.; Rhyner, J. Equivalence of the generalised grid and projection methods for the construction of quasiperiodic tilings. *Journal of Physics A: Mathematical and General* **1986**, *19*, 267.
- [43] Shechtman, D.; Blech, I.; Gratias, D.; Cahn, J. W. Metallic Phase with Long-Range Orientational Order and No Translational Symmetry. *Physical Review Letters* **1984**, *53*, 1951–1953.

- [44] Bendersky, L. Quasicrystal with One-Dimensional Translational Symmetry and a Tenfold Rotation Axis. *Physical Review Letters* **1985**, *55*, 1461–1463.
- [45] Ishimasa, T.; Nissen, H.-U.; Fukano, Y. New ordered state between crystalline and amorphous in Ni-Cr particles. *Physical Review Letters* **1985**, *55*, 511–513.
- [46] Wang, N.; Chen, H.; Kuo, K. H. Two-dimensional quasicrystal with eightfold rotational symmetry. *Physical Review Letters* **1987**, *59*, 1010–1013.
- [47] Tsai, A.-P. "Back to the Future" - An Account Discovery of Stable Quasicrystals. *Accounts of Chemical Research* **2003**, *36*, 31–38.
- [48] Tsai, A. P. Icosahedral clusters, icosahedral order and stability of quasicrystals: a view of metallurgy. *Science and Technology of Advanced Materials* **2008**, *9*, 013008.
- [49] Steurer, W.; Deloudi, S. *Crystallography of Quasicrystals: Concepts, Methods and Structures*; Springer Series in Materials Science; Springer Berlin Heidelberg, 2009.
- [50] Tsai, A.-P. Discovery of stable icosahedral quasicrystals: progress in understanding structure and properties. *Chemical Society Reviews* **2013**, *42*, 5352–5365.
- [51] Zeng, X.; Ungar, G.; Liu, Y.; Percec, V.; Dulcey, A. E.; Hobbs, J. K. Supramolecular dendritic liquid quasicrystals. *Nature* **2004**, *428*, 157–160.
- [52] Takano, A.; Kawashima, W.; Noro, A.; Isono, Y.; Tanaka, N.; Dotera, T.; Matsushita, Y. A mesoscopic Archimedean tiling having a new complexity in an ABC star polymer. *Journal of Polymer Science Part B: Polymer Physics* **2005**, *43*, 2427–2432.
- [53] Fischer, S.; Exner, A.; Zielske, K.; Perlich, J.; Deloudi, S.; Steurer, W.; Lindner, P.; Foerster, S. Colloidal quasicrystals with 12-fold and 18-fold diffraction symmetry. *Proceedings of the National Academy of Sciences of the United States of America* **2011**, *108*, 1810–1814.
- [54] Zhang, J.; Bates, F. S. Dodecagonal Quasicrystalline Morphology in a Poly(styrene-*b*-isoprene-*b*-styrene-*b*-ethylene oxide) Tetrablock Terpolymer. *Journal of the American Chemical Society* **2012**, *134*, 7636–7639, PMID: 22506899.
- [55] Gillard, T. M.; Lee, S.; Bates, F. S. Dodecagonal quasicrystalline order in a diblock copolymer melt. *Proceedings of the National Academy of Sciences* **2016**, *113*, 5167–5172.
- [56] Xiao, C.; Fujita, N.; Miyasaka, K.; Sakamoto, Y.; Terasaki, O. Dodecagonal tiling in mesoporous silica. *Nature* **2012**, *487*, 349–353.
- [57] Foerster, S.; Meinel, K.; Hammer, R.; Trautmann, M.; Widdra, W. Quasicrystalline structure formation in a classical crystalline thin-film system. *Nature* **2013**, *502*, 215–218.

- [58] Urgel, J. I.; Écija, D.; Lyu, G.; Zhang, R.; Palma, C.-A.; Auwärter, W.; Lin, N.; Barth, J. V. Quasicrystallinity expressed in two-dimensional coordination networks. *Nature Chemistry* **2016**, *8*, 657–662.
- [59] Wasio, N. A.; Quardokus, R. C.; Forrest, R. P.; Lent, C. S.; Corcelli, S. A.; Christie, J. A.; Henderson, K. W.; Kandel, S. A. Self-assembly of hydrogen-bonded two-dimensional quasicrystals. *Nature* **2014**, *507*, 86–89.
- [60] Passens, M.; Caciuc, V.; Atodiresei, N.; Feuerbacher, M.; Moors, M.; Dunin-Borkowski, R. E.; Bluegel, S.; Waser, R.; Karthaeuser, S. Interface-driven formation of a two-dimensional dodecagonal fullerene quasicrystal. *Nature Communications* **2017**, *8*, 15367.
- [61] Talapin, D. V.; Shevchenko, E. V.; Bodnarchuk, M. I.; Ye, X.; Chen, J.; Murray, C. B. Quasicrystalline order in self-assembled binary nanoparticle superlattices. *Nature* **2009**, *461*, 964–967.
- [62] Bodnarchuk, M. I.; Erni, R.; Krumeich, F.; Kovalenko, M. V. Binary Superlattices from Colloidal Nanocrystals and Giant Polyoxometalate Clusters. *Nano Letters* **2013**, *13*, 1699–1705, PMID: 23488858.
- [63] Yang, Z.; Wei, J.; Bonville, P.; Pileni, M.-P. Beyond Entropy: Magnetic Forces Induce Formation of Quasicrystalline Structure in Binary Nanocrystal Superlattices. *Journal of the American Chemical Society* **2015**, *137*, 4487–4493, PMID: 25785302.
- [64] Ye, X.; Chen, J.; Irrgang, M. E.; Engel, M.; Dong, A.; Glotzer, S. C.; Murray, C. B. Quasicrystalline nanocrystal superlattice with partial matching rules. *Nature Materials* **2017**, *16*, 214–219.
- [65] Dotera, T.; Oshiro, T.; Zihlerl, P. Mosaic two-lengthscale quasicrystals. *Nature* **2014**, *506*, 208–211.
- [66] Wei, J.; Schaeffer, N.; Pileni, M.-P. Ligand Exchange Governs the Crystal Structures in Binary Nanocrystal Superlattices. *Journal of the American Chemical Society* **2015**, *137*, 14773–14784.
- [67] Marciniak, B. *Hydrosilylation: A Comprehensive Review on Recent Advances*; Advances in Silicon Science; Springer, 2008.
- [68] Lee, S.; Lee, S. Shrinkage ratio of PDMS and its alignment method for the wafer level process. *Microsystem Technologies* **2008**, *14*, 205–208.
- [69] Michler, G. *Electron Microscopy of Polymers*; Springer Laboratory; Springer Berlin Heidelberg, 2008.
- [70] Ackermann, J. *Handbuch fuer die Rasterelektronenmikroskope SUPRA und ULTRA*. Carl Zeiss NTS GmbH, 2004.

- [71] Williams, D.; Carter, C. *Transmission Electron Microscopy: A Textbook for Materials Science*; Cambridge library collection Bd. 3; Springer, 2009.
- [72] Chescoe, D.; Goodhew, P. *The Operation of Transmission and Scanning Electron Microscopes*; Microscopy handbooks; Oxford University Press, 1990.



### 3 Synthesis of colloidal polymer particles

This section describes the synthesis of monodisperse polymer particles. Monodispersity of the particles is crucial for the assembly of colloidal crystals with a high order. In this thesis, self-assembly experiments were accomplished both with commercial and self-made particles. Commercial particles are available with a great variety of sizes and materials, though they are comparable expensive. By contrast, the own synthesis of particles has the advantage of a precise control of the particle size and composition using a low effort and a low cost synthesis procedure. However, the accessible size range of self-made particles is limited to approximately 200 – 1000 nm for the presented procedure.

Monodisperse polystyrene (PS) particles with acrylic acid as co-monomer were prepared by emulsifier-free emulsion polymerization. The synthesis procedure was adapted from Ottewill *et al.*<sup>[1]</sup> They reported that the particle size can be adjusted by various parameters including monomer and co-monomer concentration, temperature and ionic strength.

#### 3.1 Variation of co-monomer concentration

The prepared PS particles were co-polymerized with acrylic acid. Acrylic acid is an unsaturated carboxylic acid and therefore introduces charges to the particles in aqueous media. These charges contribute to the electrostatic stabilization of the particles. As a consequence, different particle sizes can be realized in dependence on the amount of co-monomer. Table 3.1 shows three sets of experiments, in which the amount of acrylic acid was systematically varied. The different sets are the result of syntheses with three different batches of acrylic acid. Set A was synthesized by F. A. Nutz (Physical Chemistry I – Polymer Systems, University of Bayreuth).

The dependence of the particle size on the concentration of acrylic acid is shown in Figure 3.1. The SEM images on the right side show three syntheses from set C with increasing particle diameter. Within the individual sets, the dependence follows the expected trend. The particles are electrostatically stabilized by the sulfate moieties of the initiator and the dissociated carbonate groups of the co-monomer. An increasing number of charged groups in the polymer chains can stabilize smaller particles, so that the final diameter decreases with increasing concentration of acrylic acid. However, if the three sets are considered together, this trend is not consistent. Overall, the acrylic acid batch used in set A yielded larger particles, which could not be reproduced in set B or C. A further result from the experimental sets B and C is that the particle size slightly decreased for a reduced styrene concentration (Table 3.1, B01/C01 and B02/C02).

Table 3.1: Syntheses of polystyrene particles in 250 mL water.

#	styrene / mL	acrylic acid / mL	potassium peroxodisul- fate (KPS) / mg	diameter / nm
A01	30	0.50	100	$800 \pm 8$
A02	30	6.00	100	$334 \pm 5$
B01	30	0.50	100	$447 \pm 10$
B02	30	0.25	100	$469 \pm 12$
C01	25	0.50	100	$403 \pm 8$
C02	25	0.25	100	$453 \pm 3$
C03	25	0.13	100	$497 \pm 3$
C04	25	0.00	100	$512 \pm 6$

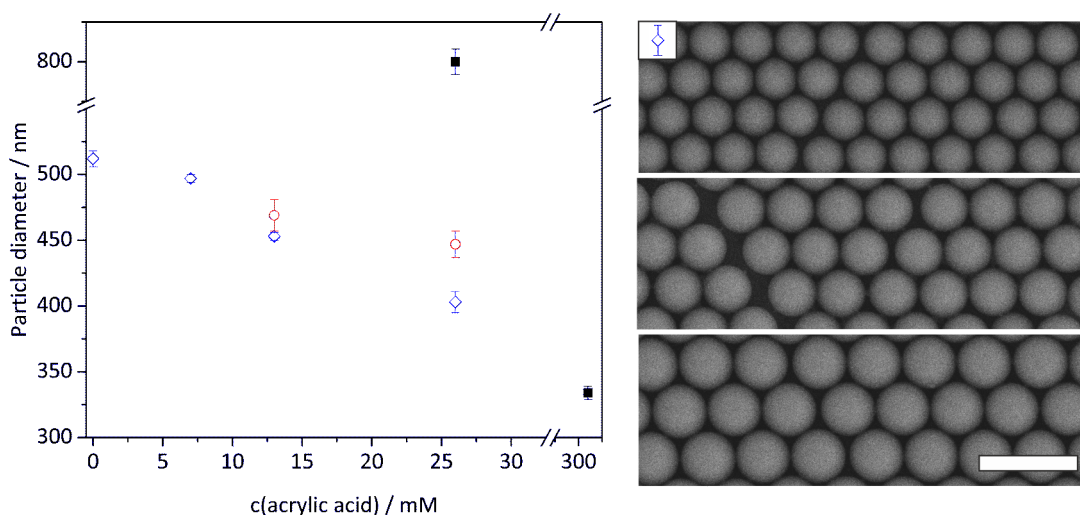


Figure 3.1: Dependence of the colloidal particle diameter on the concentration of acrylic acid. Solid squares represent polymerizations from set A in Table 3.1. Open circles represent polymerizations from set B in Table 3.1. Open rhombs represent polymerizations from set C in Table 3.1. SEM images on the right side show particles with increasing diameter from set C. Scale bar  $1 \mu\text{m}$ .

As particles with larger diameters ( $> 700 \text{ nm}$ ) were relevant for some parts of this work, further reaction parameters, such as temperature and ionic strength, were considered to tune the particle size over a wider range.

### 3.2 Variation of reaction temperature

The reaction temperature was studied at fixed concentrations of the individual components. The volume ratio of styrene and acrylic acid was set to 100 : 1 for all experiments. Three polymerizations at temperatures between 60 °C and 80 °C were carried out. Table 3.2 and Figure 3.2 present the results for the particle sizes in dependence on the polymerization temperatures. With decreasing temperature the particle size increased. This is reasonable as the decay rate of the initiator is temperature dependent. At a lower temperature less initiator is available at the stage of nucleation. This results in fewer particle nuclei, which in turn can grow larger as the same amount of monomer is available. However, it has to be noticed that for temperatures lower than 70 °C the reaction time has to be significantly increased to obtain a comparable conversion. The polymerization at 60 °C was quenched after more than two days so that the conversion amounted to approximately 50 %. For higher reaction temperatures, conversions in the order of 60 – 70 % are commonly observed in less than half of the reaction time.

Table 3.2: Syntheses of polystyrene particles with 10 mL styrene, 0.1 mL acrylic acid and 40 mg KPS in 100 mL water.

#	T / °C	diameter / nm
D01	60	522 ± 6
D02	70	481 ± 7
D03	80	422 ± 4

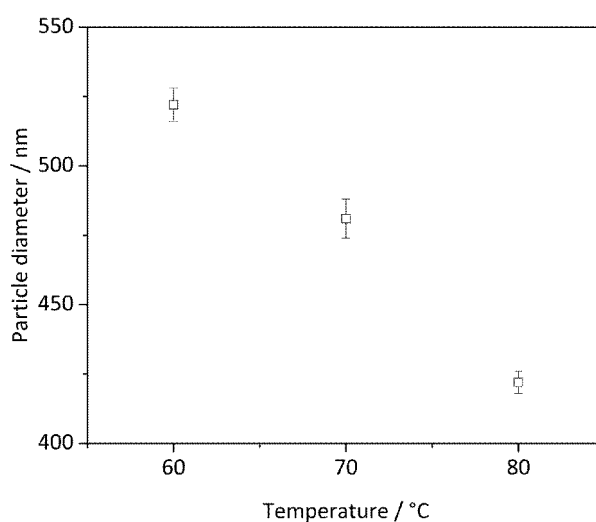


Figure 3.2: Dependence of the colloidal particle diameter on the reaction temperature.

### 3.3 Variation of the ionic strength

Besides monomer concentration and reaction temperature, the particle size can also be influenced by the addition of electrolytes. In this work, the polymerization protocol was modified by adding NaCl to the reaction medium. NaCl has the advantage that it only affects the particle stability by adjusting the ionic strength, but keeps the pH of the aqueous phase constant. The results of the influence of the ionic strength on the particle size are shown in Table 3.3 and Figure 3.3.

Table 3.3: Syntheses of polystyrene particles with 10 mL styrene, 0.1 mL acrylic acid and 40 mg KPS in 100 mL water at 70 °C.

#	NaCl / mg	diameter / nm
E01	0	481 ± 7
E02	6	560 ± 7
E03	12	621 ± 6
E04	18	751 ± 11
E05	50	941 ± 20

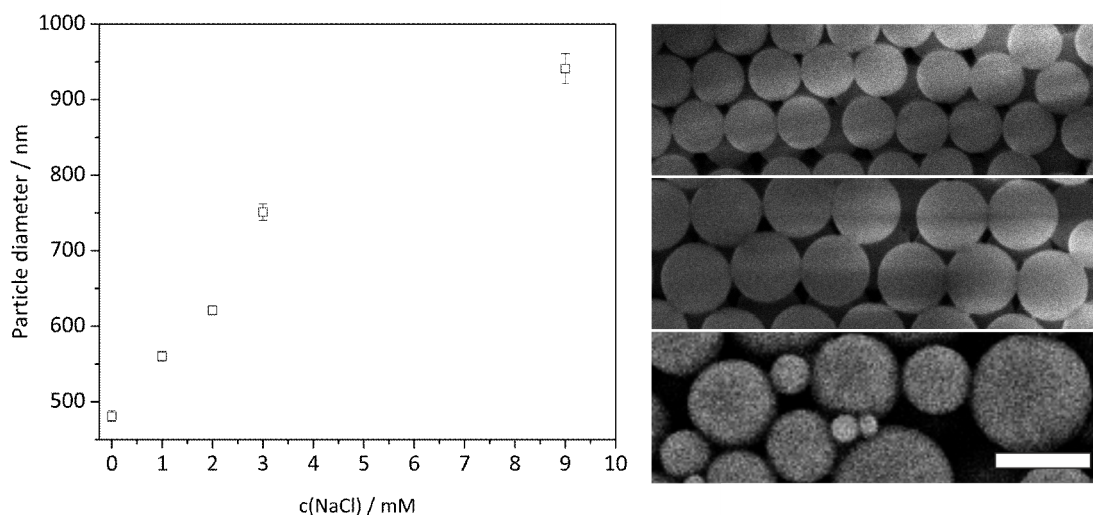


Figure 3.3: Dependence of the colloidal particle diameter on the ionic strength of the reaction mixture. SEM images on the right side show synthesized particles for increasing NaCl concentration. With increasing particle size a gradual loss of monodispersity is observed. Scale bar 1  $\mu\text{m}$ .

The particle size increased gradually with NaCl concentration and ranged from 481 nm to 941 nm. This is a consequence of the altered particle stabilization in the presence of electrolytes. With increasing electrolyte concentration, the thickness of the diffuse part of the

electrical double layer is gradually compressed. The interparticle repulsion is reduced and particle coagulation takes place. In comparison to the polymerization experiments with varying monomer concentrations and reaction temperatures, the variation of the NaCl concentration yields significantly larger particle sizes. Indeed, for concentrations  $c(\text{NaCl}) > 2 \text{ mM}$  the particle size rises over 700 nm. Though, the standard deviation of the particle size obtained from the scanning electron microscopy (SEM) images indicated that the monodispersity is gradually lost. For this reason NaCl cannot be used without limitations. Furthermore, the presence of NaCl in the polymerization mixture is disadvantageous for the particle assembly in the further projects of this thesis. As assembly experiments are very sensitive to the presence of an electrolyte, the added NaCl has to be completely removed after synthesis. This involves additional dialysis for several days to weeks.

In conclusion, it was shown that the particle size can be tuned by various parameters. Whereas an increase of co-monomer concentration and temperature yields smaller particles, higher concentrations of monomer or electrolyte leads to larger particles. Overall, the preferred parameters to tune the particle size are the co-monomer concentration and the reaction temperature. The addition of electrolytes causes a significantly higher effort during purification and is not suitable for particles for self-assembly.

## References

- [1] Goodwin, J. W.; Hearn, J.; Ho, C. C.; Ottewill, R. H. Studies on the preparation and characterisation of monodisperse polystyrene latices. *Colloid and Polymer Science* **1974**, *252*, 464–471.

## 4 Preparation of two-dimensional Bravais lattices by colloidal self-assembly

The aim of this thesis is the preparation of ordered structures with symmetries other than hexagonally close-packed. For this purpose, the synthesized polymer particles with are processed using a modified self-assembly technique.

Two dimensional particle arrays on solid substrates are widely used for the fabrication of functional surfaces and thin film devices. One of their major applications is colloidal lithography.<sup>[1-4]</sup> Besides this, monolayer colloidal crystals are applied in optics<sup>[5]</sup>, in photonics<sup>[6]</sup>, as high-density data storage<sup>[7]</sup> as well as adhesive/non-adhesive surfaces<sup>[8]</sup>. With the development of procedures for the synthesis of highly monodisperse colloidal particles, self-assembly became a convenient method to fabricate colloidal crystals. Available fabrication methods can be divided into direct assembly of colloidal particles on solid substrates and liquid interface-mediated assembly.<sup>[9]</sup> A common feature of all these techniques is that they yield ordered particle arrays with a hexagonally close-packed (hcp) alignment. After the establishment of these robust and reliable methods, a logical consequence was the desire to prepare also non-close-packed particle arrays with tunable interparticle distances, and non-hexagonal symmetries. The motivation for the increasing interest was to control the optical, adhesive or magnetic surface properties for new applications, e.g., anti-reflective coatings<sup>[10]</sup> or photonic band gap devices<sup>[11]</sup>.

The difference to the established hcp structures, is that in general ordered non-close-packed particle arrays are not readily accessible via colloidal self-assembly. One of the major obstacles are capillary forces that lead to a strong attraction between particles, which finally result in the formation of lattices with the highest density, thus hcp symmetry. However, there have been various approaches explored that circumvent this limitation. These approaches either shift the balance between attractive and repulsive forces during assembly, or rely on post-processing to convert initial hcp into non-close-packed structures.

An example of the first approach is the assembly of colloidal particles at the water/oil interface. The balance between attractive and repulsive forces is significantly different for water/air and water/oil interfaces, which leads to the appearance of non-close-packed structures in the latter case. This can be attributed to both a different contact angle of the particles at the water/oil interface and a minor amount of surface charges stabilized in the oil phase by small water residues on the particle surfaces. In total, this reduces capillary forces and strengthens electrostatic repulsion. Accordingly, interparticle distances up to several times the particle diameter can be realized by simply adjusting the number of particles at the interface.<sup>[12,13]</sup> A major drawback of this technique is that the colloidal assembly loses its non-close-packed character during transfer from the oil/water interface to a solid substrate due to the onset of attractive capillary forces upon drying.

An example of the fabrication of non-close-packed structures by post-processing is the reduction of the particle size. Thereby, the initial hcp structures are obtained by standard preparation techniques. Subsequently, the particle diameter is reduced, e. g., in a plasma atmosphere, whereby the particle position is not affected.<sup>[9,14]</sup> Limitations of this process are that the interparticle distance is predetermined by the initial particle diameter and the maximal reduction of the particle diameter is restricted by the nature of the etching process.<sup>[15,16]</sup> Alternative routes to transform close-packed arrays into non-close packed arrays include shrinking of close-packed particles<sup>[17,18]</sup> or degradation of a polymer shell of core/shell particles<sup>[19,20]</sup>. However, all these approaches have in common that they are based on hcp structures and as they do not change the relative arrangement of the particles, the results are again hexagonal arrays.

The challenge to fabricate non-close-packed ordered arrays with non-hexagonal symmetries on solid substrates has only been addressed by a few approaches. One of these approaches is based on structured substrates, which are used as templates. The particles then assemble in the foreseen positions, which can be close-packed or non-close-packed arrays with various lattice geometries.<sup>[21-23]</sup> However, the patterned substrate used as template has to be prepared typically by some kind of lithography, which limits the versatility of the technique to some extent. Another strategy works on the basis of hcp structures on flexible substrates. By a combination of isotropic swelling and anisotropic stretching the initial hcp arrays are transformed into various non-close-packed structures. Depending on the individual stretching steps, the particles are separated along given directions yielding a wide range of lattice geometries.<sup>[24,25]</sup> Finally, in an additional step, the stretched structures have to be transferred onto a second rigid substrate in order to preserve the generated arrangement.

In conclusion, the available methods for the fabrication of non-close-packed structures are either restricted to hexagonal symmetries or require complex, multi-step procedures, that restrict the flexibility of the approaches. As a consequence, there exists currently no simple method that produces ordered non-close-packed arrays with non-hexagonal symmetry in a controlled manner.

## 4.1 Preparation of colloidal monolayers

This thesis presents a newly developed method for the preparation of non-close-packed colloidal monolayers. Thereby, special attention is directed on the fabrication of particle arrays with any of the possible two-dimensional Bravais lattice symmetries. In principle, the method is based on the transformation of hcp monolayers into non-close-packed structures via stretching. The assembly of hcp monolayers at the water/air interface can be readily accomplished by a variety of different techniques.<sup>[9,14,26,27]</sup> In this work, freely floating monolayers at the water/air interface are prepared via a method established by Retsch *et al.*<sup>[26]</sup> The general process of this method is depicted in Figure 4.1.

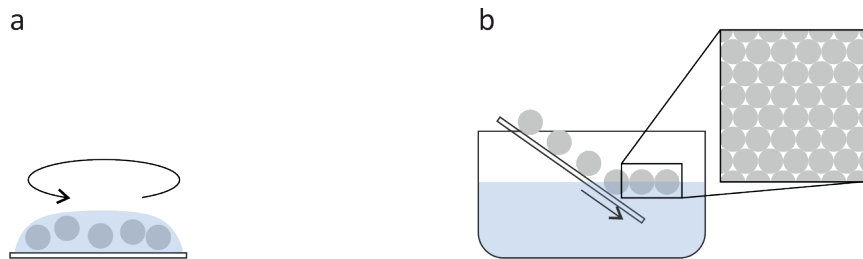


Figure 4.1: Fabrication of hcp monolayers by interfacial self-assembly. (a) A particle dispersion is spin-coated on cationically functionalized glass slides. (b) Slow immersion of the glass slide into an aqueous solution of SDS at high pH yields a hcp monolayer at the water/air interface.

Basically, this procedure is compatible with a variety of colloids. For the major part of experiments, poly(*n*-butyl acrylate-co-methyl methacrylate) (P(nBA-co-MMA)) was chosen as model particles. In the first step, aqueous particle dispersions with a concentration of 2.5 wt% were spin-coated on cationically functionalized glass slides (Figure 4.1 a). Due to the partially negatively charged particle surface, a single layer of particles is formed, within which the particles are individually attached to the positively charged moieties on the glass. This glass slide was subsequently immersed into an aqueous solution of sodium dodecyl sulfate (SDS) and ammonia (pH 12). At the three phase contact line, the particles detached from the glass surface and were transferred to the water/air interface (Figure 4.1 b). Trapped at the interface, the particles formed a hcp monolayer with large single-crystalline domains apparent from the intense iridescent colors (Figure 4.2 a).

In order to verify the hcp structure at the water/air interface, the monolayer was transferred onto a conventional, hydrophilic substrate (untreated glass). Thereby, the substrate was positioned beneath the monolayer in the subphase and upon moving out of the water the particles were collected on the surface of the substrate (Z-type deposition<sup>[28]</sup>). As expected, the scanning electron microscopy (SEM) image showed the formation of an ordered hcp structure (Figure 4.2 b).<sup>[26]</sup>

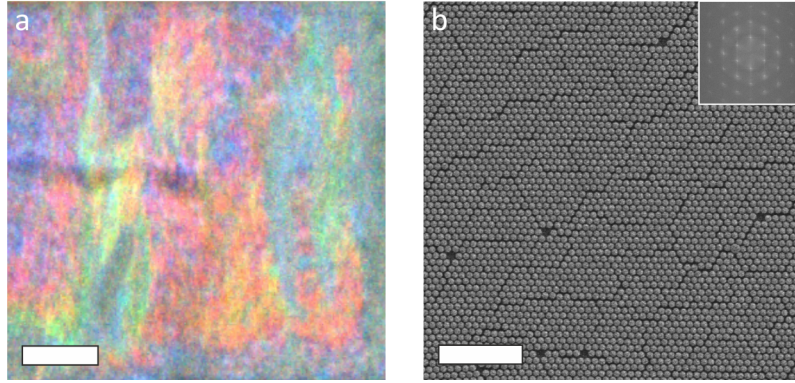


Figure 4.2: (a) Microscopic image of a hcp monolayer at the water/air interface. Scale bar is  $100 \mu\text{m}$ . (b) SEM image of a particle monolayer on a hydrophilic glass substrate with an ordered hcp structure. The inset shows the corresponding FFT. Scale bar is  $5 \mu\text{m}$ .

## 4.2 Transfer of colloidal monolayers onto hydrophobic substrates

As opposed to this, the preparation of non-close-packed arrays by stretching requires transferring the monolayer onto a hydrophobic substrate by immersion into water (X-type deposition<sup>[28]</sup>). For this purpose, the contact angle of the substrate has to be larger than a certain critical angle  $\theta_c$ . In our experimental setup, the collection of particles was possible for substrates with a contact angle larger than  $\theta_c \sim 65^\circ$ . The general procedure of this newly developed method for the fabrication of non-close-packed monolayers is depicted in Figure 4.3. During immersion, the particles at the interface attached successively to the lower side of the substrate (Figure 4.3 a). As a result, the transfer to the substrate induced a controlled, one dimensional stretching of the hcp array leading to a variety of symmetries depending on the transfer angle and degree of stretching.

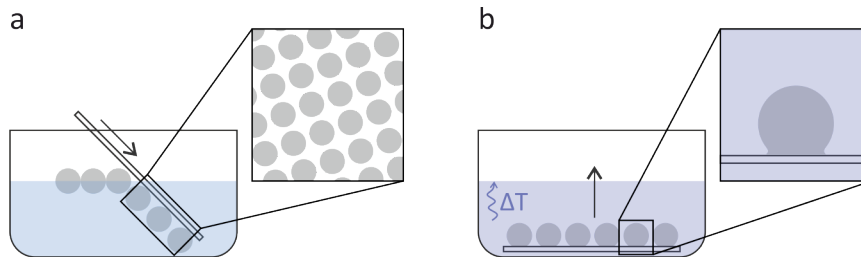


Figure 4.3: Fabrication of non-close-packed monolayers. (a) The monolayer is transferred to the lower side of a hydrophobic substrate by submerging the substrate through the monolayer into the subphase. Thereby, the particle monolayer is stretched into a non-close-packed array. (b) The particles are immobilized on the substrate via thermal fixation near the glass transition temperature of the particles. After fixation, the substrate with the monolayer can be recovered from the solution, while the non-close-packed structure is preserved.

This behavior can be explained by flow patterns that emerged during immersion of a substrate. For hydrophobic substrates with contact angles  $\theta > \theta_c$  the monolayer flows towards the contact line, typically at a velocity smaller than the immersion velocity of the substrate. Consequently, the ratio between immersed substrate area  $A_{sub}$  and transferred monolayer area  $A_{mon}$  is larger than 1. The result is a one dimensional stretching of the original hcp particle array along the immersion direction.<sup>[28]</sup>

The formed non-close-packed structure is now stable as long as the monolayer on the substrate is completely immersed in water. However, upon removal of the substrate from the aqueous phase, the non-close-packed structure collapsed and formed smaller particle assemblies with local hexagonal order (Figure 4.4). This is a result of attractive capillary forces during drying. On the removed substrate, the particles are initially situated in a thin film of water. Though, the water continuously evaporates, so that the particles eventually approach the water/air interface. The contact angle of the particles deforms the fluid interface between the particles and following that immersion forces drag the particles together.

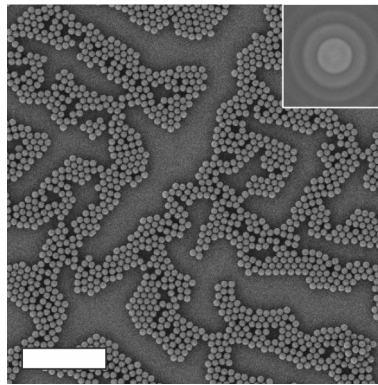


Figure 4.4: SEM image of a particle monolayer on a hydrophobic substrate. After drying the non-close-packed structure collapsed due to immersion forces. The inset shows the corresponding FFT. Scale bar is  $5 \mu\text{m}$ .

A visible indication of this process is the loss of iridescent colors on the dried substrate (Figure 4.5 a). On contrary, laser diffraction at the monolayer showed four broad Bragg peaks, which indicates a certain kind of order in the monolayer (Figure 4.5 b). Indeed a closer inspection of the SEM image (Figure 4.4) reveals a preferential alignment along the diagonals of the image. It follows that the particles, which were located in non-close-packed, tetragonal arrays, rearranged and collapsed into the more stable, hexagonal substructures. Thereby, the local tetragonal arrangement was lost, but remained present at larger scales in form of the alignment of the hexagonal substructures.

In order to suppress the collapse of the non-close-packed structure, the occurring immersion forces need to be counter-balanced. In an untreated sample the particles can be considered as ideal spheres on a flat surface (Figure 4.6 a). Their small contact area to the substrate makes them prone to external forces, which change the positional order. One

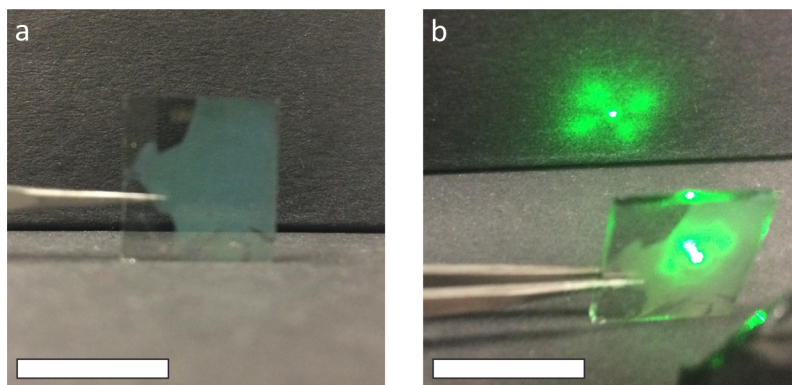


Figure 4.5: Non-immobilized particle monolayer. (a) Photograph of a non-immobilized particle monolayer on a hydrophobic substrate. After drying the iridescent color of the monolayer is lost due to capillary forces that lead to shifts of the particles positions. (b) Laser diffraction of a non-immobilized particle monolayer. Despite the loss of the short-range positional order of the particles after drying, a weak long-range orientational correlation is apparent from the four blurred peaks in the diffraction pattern. Scale bars are 1 cm.

possibility to prevent this is the immobilization of the particles on the substrate prior to their removal from the aqueous phase. In this concern, a straightforward process is the thermal fixation. More exactly, either the particles or the substrate possess a moderate glass transition temperature ( $T_g$ ). Heating near the corresponding  $T_g$  increases the adhesive contact area of the particles on the substrate and immobilizes them on their position in the non-close-packed structure (Figure 4.6 b). It can be seen that indeed the adhesive area is increased, but the overall spherical shape of the particles stays intact.

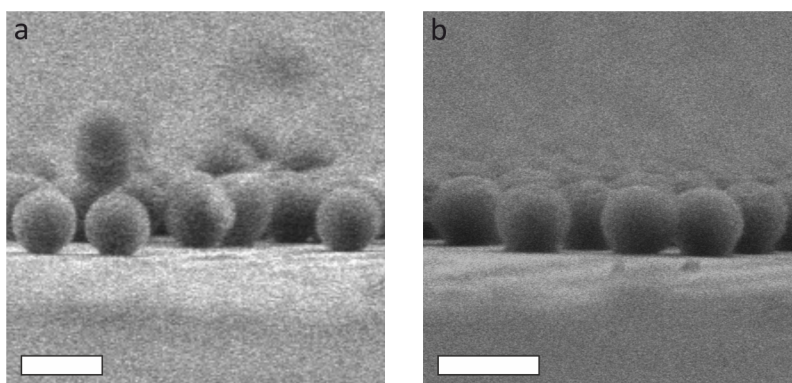


Figure 4.6: Side view SEM images of (a) non-immobilized and (b) immobilized particles. Without thermal fixation, the particles can be viewed as hard spheres, which feature a minimal contact area on the substrate. Upon drying of the monolayer, these particles are subject to capillary forces. Thermal fixation of the particles near their  $T_g$  leads to an increase of the contact area on the substrate. In the viscous state, the particles fuse onto the substrate and become immobilized at their positions even under capillary stress. Scale bars are 500 nm.

For polymer particles with a  $T_g \ll 100^\circ\text{C}$ , the thermal fixation can be conveniently accomplished by heating the monolayer on the substrate in the aqueous solution prior to removal (Figure 4.3 b). Subsequently, the substrate can be recovered from the aqueous solution without affecting the particle positions in the non-close-packed structures (Figure 4.7).

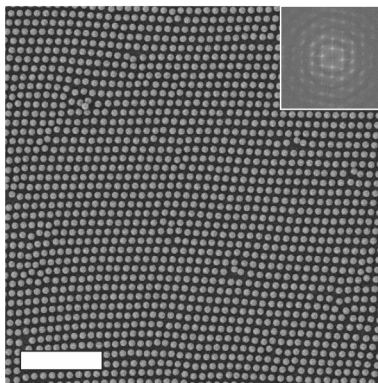


Figure 4.7: SEM image of a particle monolayer on a hydrophobic substrate with an ordered, non-close-packed structure. The inset shows the corresponding FFT. Scale bar is  $5\ \mu\text{m}$ .

The preserved non-close-packed structure is also manifested by the iridescent colors of the monolayer on the substrate (Figure 4.8 a). Laser diffraction at substrates, which have been thermally fixated, showed the presence of large single-crystalline domains with long-range order (Figure 4.8 b). In summary, this demonstrates that a transfer of hcp structures onto hydrophobic substrate generates non-close-packed particle arrays. Moreover, these non-close-packed structures are susceptible to capillary forces, why fixation is necessary to obtain permanently stable structures.

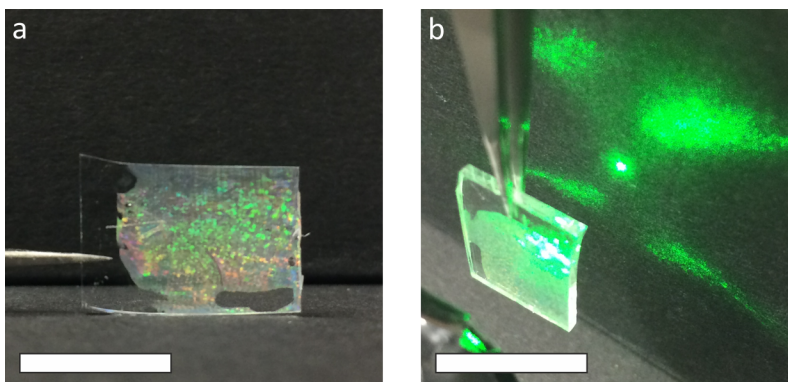


Figure 4.8: Immobilized particle monolayer. (a) Photograph of an immobilized particle monolayer on a hydrophobic substrate. The iridescent color preserved after drying of the monolayer indicates an intact positional arrangement of the particles. (b) Laser diffraction of an immobilized particle monolayer. The sharp peaks confirm the high order of the particles in the monolayer. Scale bars are 1 cm.

An alternative to polymer particles with an appropriate  $T_g$  for the fabrication of non-close-packed structures is the application of hydrophobic substrates with a  $T_g \ll 100^\circ\text{C}$ . By this means, arbitrary polymer and inorganic particles can be processed to monolayers with non-close-packed structures. For this purpose, polymers with hydrophobic character and a glass transition temperature  $20^\circ\text{C} < T_g \ll 100^\circ\text{C}$  were synthesized. As model polymer poly(*n*-butyl acrylate-co-styrene) (P(nBA-co-S)) with a  $T_g = 54^\circ\text{C}$  and a contact angle  $\theta = 86^\circ$  was chosen. P(nBA-co-S) was spin-coated on glass substrates to render the surface hydrophobic and used these substrates in the same way as described in Figure 4.3. As particles two types of polystyrene (PS) colloids were applied: in-house synthesized particles with a diameter of 453 nm (C02) and commercially available particles with a diameter of 2560 nm (microparticles GmbH). Besides the different size, the particles are characterized by different co-monomers for electrostatic stabilization.

Consistent with the results for the polymer particles of P(nBA-co-MMA) with a low  $T_g$ , for both PS particles non-close-packed structures were obtained on the P(nBA-co-S) substrates (Figure 4.9). The structural difference of both samples, oblique (Figure 4.9 a) and rectangular (Figure 4.9 b), is the result of the discrete orientation of the respective hcp domain in the monolayer at the water/air interface with respect to the immersion direction.

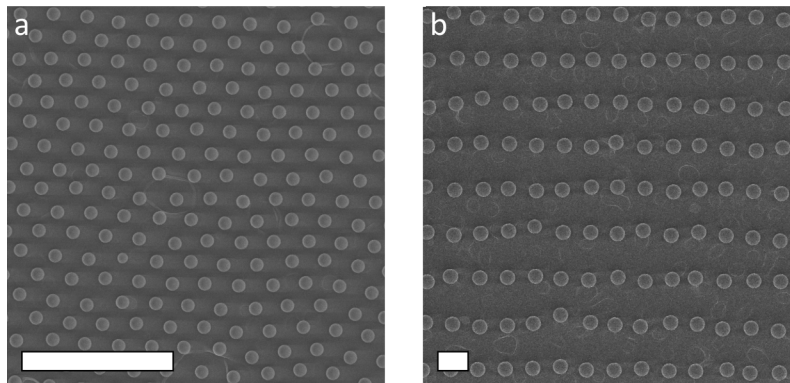


Figure 4.9: SEM images of PS particle monolayers on hydrophobic P(nBA-co-S) substrates with ordered, non-close-packed structures: (a) oblique and (b) rectangular. Scale bars are  $5\ \mu\text{m}$ .

In conclusion, the transfer method is compatible with a wide range of particles, as the thermal fixation can be both accomplished via the particles themselves and the hydrophobic substrate. Furthermore, the versatility of the presented technique has a broad implication for the fabrication of non-close-packed particle arrays. The obtained structure is completely defined by the transfer direction and the stretching factor and independent of the particle type or size.

### 4.3 Theoretical analysis of monolayer stretching

Due to the definedness of the presented process, it is possible to derive a mathematical description for the stretching of a hcp structure. Starting with a conventional hcp particle array, the base vectors  $\vec{e}_1$  and  $\vec{e}_2$  of the hexagonal unit cell (Figure 4.10) are given as

$$\vec{e}_1 = \begin{pmatrix} 1 \\ 0 \end{pmatrix} \quad (4.1)$$

$$\vec{e}_2 = \begin{pmatrix} -0.5 \\ -0.5\sqrt{3} \end{pmatrix} \quad (4.2)$$

From this point, the actual orientation of the hcp structure at the water/air interface with respect to the immersion direction is specified by the rotation angle  $\delta$  as shown in Figure 4.10.

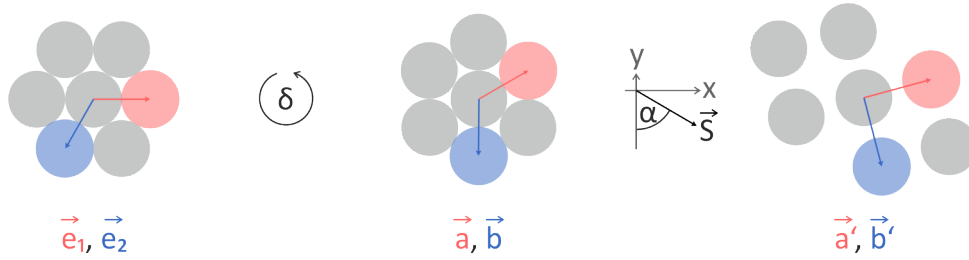


Figure 4.10: Definition of the initial hcp domain orientation angle  $\delta$ , stretching angle  $\alpha$  and stretching vector  $\vec{S}$ .

Thereby, the base vectors  $\vec{a}$  and  $\vec{b}$  for the correctly rotated hcp structure prior to transfer can be calculated from  $\vec{e}_1$  and  $\vec{e}_2$  using a rotation matrix

$$\vec{a} = \begin{bmatrix} \cos \delta & -\sin \delta \\ \sin \delta & \cos \delta \end{bmatrix} \circ \vec{e}_1 \quad (4.3)$$

$$\vec{b} = \begin{bmatrix} \cos \delta & -\sin \delta \\ \sin \delta & \cos \delta \end{bmatrix} \circ \vec{e}_2 \quad (4.4)$$

The subsequent stretching of the vectors  $\vec{a}$  and  $\vec{b}$  is defined by the stretching vector  $\vec{S}$  (Figure 4.10). In this process, on one hand  $\vec{S}$  determines the degree of stretching as the stretching factor  $S = |\vec{S}|$  states the magnitude of stretching. On the other hand,  $\vec{S}$  points in the direction of stretching, which can be related to the angle  $\alpha$  between the stretching vector  $\vec{S}$  and the y-axis. Starting from  $\vec{a}$  and  $\vec{b}$ , the stretching process can be described mathematically as a sequence of matrix multiplications. In the first step, the hcp structure is rotated by an angle  $-\alpha$  ( $M_{-\alpha}$ , equation 4.5), so that  $\vec{S}$  points now along the y-axis. In the following step, the uniaxial stretching is accomplished parallel to the y-axis with a factor

$S$  ( $M_S$ , equation 4.6). Finally, in order to return to the original orientation, the stretched structure is back rotated by an angle  $\alpha$  ( $M_\alpha$ , equation 4.5). In mathematical terms this leads us to the following individual matrices.

$$M_\alpha = \begin{bmatrix} \cos \alpha & -\sin \alpha \\ \sin \alpha & \cos \alpha \end{bmatrix} \quad (4.5)$$

$$M_S = \begin{bmatrix} 1 & 0 \\ 0 & S \end{bmatrix} \quad (4.6)$$

A multiplication of these matrices according to the above described stretching process gives the complete stretching matrix ( $M = M_\alpha \circ M_S \circ M_{-\alpha}$ ) and the stretched vectors  $\vec{a}'$  and  $\vec{b}'$  of the final particle array.

$$M = \begin{bmatrix} \cos^2 \alpha + \sin^2 \alpha \cdot S & \sin \alpha \cdot \cos \alpha \cdot (1 - S) \\ \sin \alpha \cdot \cos \alpha \cdot (1 - S) & \cos^2 \alpha \cdot \sin^2 \alpha \end{bmatrix} \quad (4.7)$$

$$\vec{a}' = M \circ \vec{a} \quad (4.8)$$

$$\vec{b}' = M \circ \vec{b} \quad (4.9)$$

This calculation shows that the relation between the hcp structure ( $\vec{e}_1, \vec{e}_2$ ) and the stretched, non-close-packed structure ( $\vec{a}', \vec{b}'$ ) is completely determined by the parameters  $\delta, \alpha$  and  $S$ . For this reason, it is possible to theoretically predict particle arrangements after stretching for arbitrary hcp orientations and stretching vectors  $\vec{S}$ . A significant characteristic is that the obtained structures cover all of the Bravais lattice symmetries possible in two dimensional space. An overview over the accessible array symmetries is shown in Figure 4.11. For the calculation of the diagram, the two orientation angles  $\delta$  and  $\alpha$  are summarized to an angle  $\beta = \alpha - \delta$ .  $\beta$  describes the effective stretching direction with respect to the orientation of the hcp structure at the water/air interface. Due to its 6-fold rotational symmetry the considered angular range can be reduced to  $0^\circ \leq |\beta| \leq 30^\circ$ . Equivalently, the same structures evolve for all angles  $|\beta \pm n \cdot 60^\circ|$ , with  $n$  being an integer, for a constant stretching factor  $S$ .

In two-dimensional space, there exist five Bravais lattices: square, hexagonal, centered rectangular, rectangular, and oblique. These non-close-packed structures can be realized for discrete values of  $S$  and  $\beta$  as indicated in the phase diagram. An overview of realized Bravais lattice symmetries by a combination of different values of  $S$  and  $\beta$  is shown in Figure 4.12.

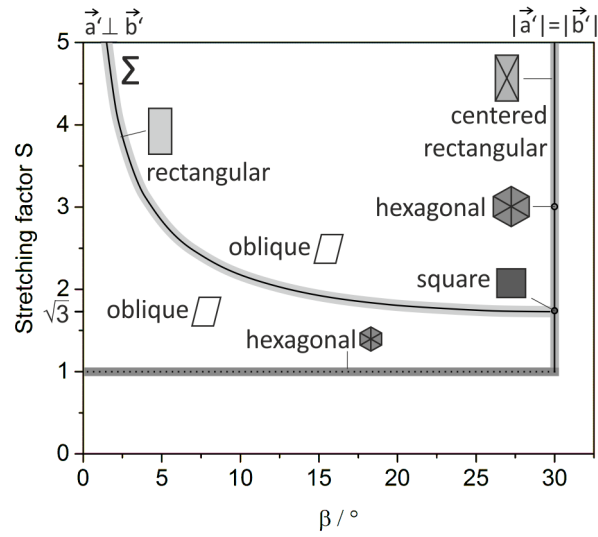


Figure 4.11: Phase diagram for accessible Bravais lattice structures in two dimensions as a function of the stretching factor  $S$  and stretching angle  $\beta$ .

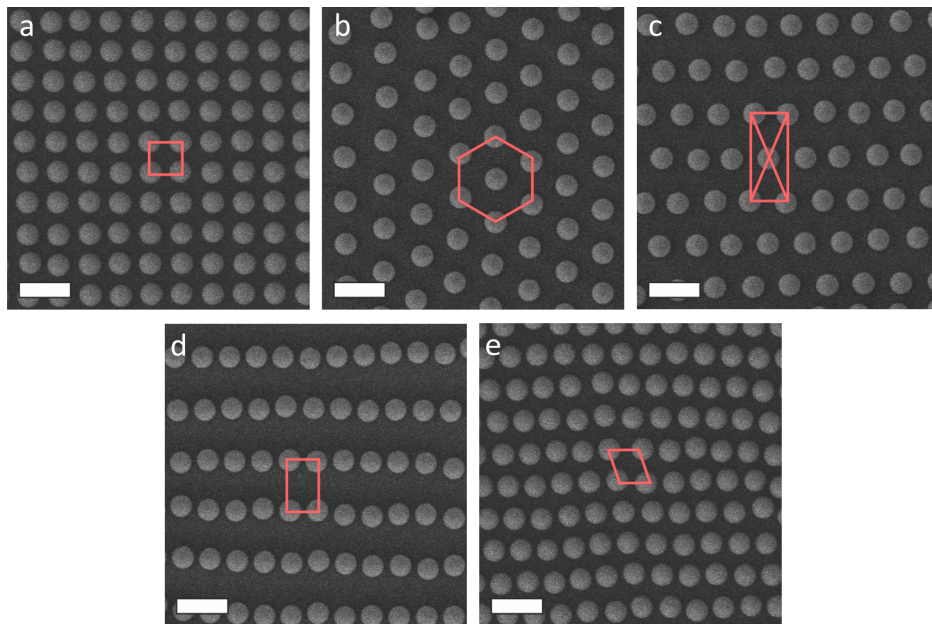


Figure 4.12: Non-close-packed particle arrays with the five possible Bravais lattices in the two-dimensional space: (a) square, (b) hexagonal, (c) centered rectangular, (d) rectangular and (e) oblique. Scale bars are  $1 \mu\text{m}$ .

A square array of particles (Figure 4.12 a) is obtained by stretching with a factor of  $S = \sqrt{3} \approx 1.73$  and a stretching direction along one of the connection vectors between the particles in the initial hcp structure ( $\beta = 30^\circ$ ). An ideal non-close-packed hexagonal array (Figure 4.12 b) can be realized by stretching with a factor of  $S = 3$  in the same direction ( $\beta = 30^\circ$ ), whereas a centered rectangular array (Figure 4.12 c) is the result for  $S \neq 1.73$  and  $S \neq 3$  at  $\beta = 30^\circ$ . Rectangular arrays (Figure 4.12 d) are the result of discrete

combinations of stretching factors and directions that fulfill the following equation

$$S = \frac{1}{\sqrt{\frac{\sin \beta \cdot (\sqrt{3} - \tan \beta)}{\sqrt{3} \cdot \sin \beta + \cos \beta}}} \quad (4.10)$$

For all other parameter combinations with  $\beta \neq 30^\circ$  oblique lattices (Figure 4.12 e) are obtained. A special case of oblique symmetry are close-packed particle lines, corresponding to highly extended oblique lattices. They can be fabricated by choosing  $\beta = 0^\circ$  and arbitrary  $S$ . In brief, non-close-packed particle arrays with symmetries of any of the five two-dimensional Bravais lattices (square, hexagon, rectangular, centered rectangular, oblique) can be prepared by a uniaxial stretching of hcp structures.

It has to be mentioned that the presented phase diagram in Figure 4.12 is only an extract of the complete phase diagram. It shows the first stretching branch  $\Sigma$ , which summarizes accessible structures for the lowest values of  $S$ . A consideration of higher stretching factors  $S > 5$  yields an expanded phase diagram with more stretching branches,  $\Phi$ ,  $\Psi$ ,  $\Omega$ . These branches feature repeatedly the same Bravais lattice symmetries for higher values of  $S$ . Thereby, the structures of each stretching branch are based on a different pair of base vectors ( $\vec{a}'_i, \vec{b}'_i$ ; with  $i = \Phi, \Psi, \Omega$ ). These vectors have in common that they are all described by linear combinations of  $\vec{a}'$  and  $\vec{b}'$ .

Figure 4.13 shows the expanded phase diagram divided into two parts. The upper diagram displays the angle between the base vectors as a function of  $S$  and  $\beta$  (Figure 4.13 a) and the lower diagram screens the relative length of the base vectors (Figure 4.13 b). As the unit cells of the Bravais lattices are specified according to the angle between the base vectors  $\vec{a}'_i$  and  $\vec{b}'_i$  of the regarded structure and the ratio of the vector lengths, the five symmetries can be identified for the additional branches using the combination of the expanded phase diagrams.

Each lattice symmetry can be described by two conditions, vector lengths and angle between two unit cell vectors (Figure 4.14): square ( $\vec{a}'_i = \vec{b}'_i$  and  $\angle \vec{a}'_i, \vec{b}'_i = 90^\circ$ ), hexagonal ( $\vec{a}'_i = \vec{b}'_i$  and  $\angle \vec{a}'_i, \vec{b}'_i = 60^\circ$ ), centered rectangular ( $\vec{a}'_i = \vec{b}'_i$  and  $\angle \vec{a}'_i, \vec{b}'_i \neq 60^\circ$  and  $\neq 90^\circ$ ), rectangular ( $\vec{a}'_i \neq \vec{b}'_i$  and  $\angle \vec{a}'_i, \vec{b}'_i = 90^\circ$ ), oblique ( $\vec{a}'_i \neq \vec{b}'_i$  and  $\angle \vec{a}'_i, \vec{b}'_i \neq 90^\circ$ ).

The mathematical description above represents a detailed tool for the prediction of possible non-close-packed structures starting from hcp particle arrays. In the opposite case experimentally observed particle arrangements can be also assigned to a distinct stretching process. Then, the stretching direction  $\alpha$  and magnitude  $S$  are determined by the following equations.

$$\alpha = \cot^{-1} \left( \frac{y' - y(\delta)}{x' - x(\delta)} \right) \quad (4.11)$$

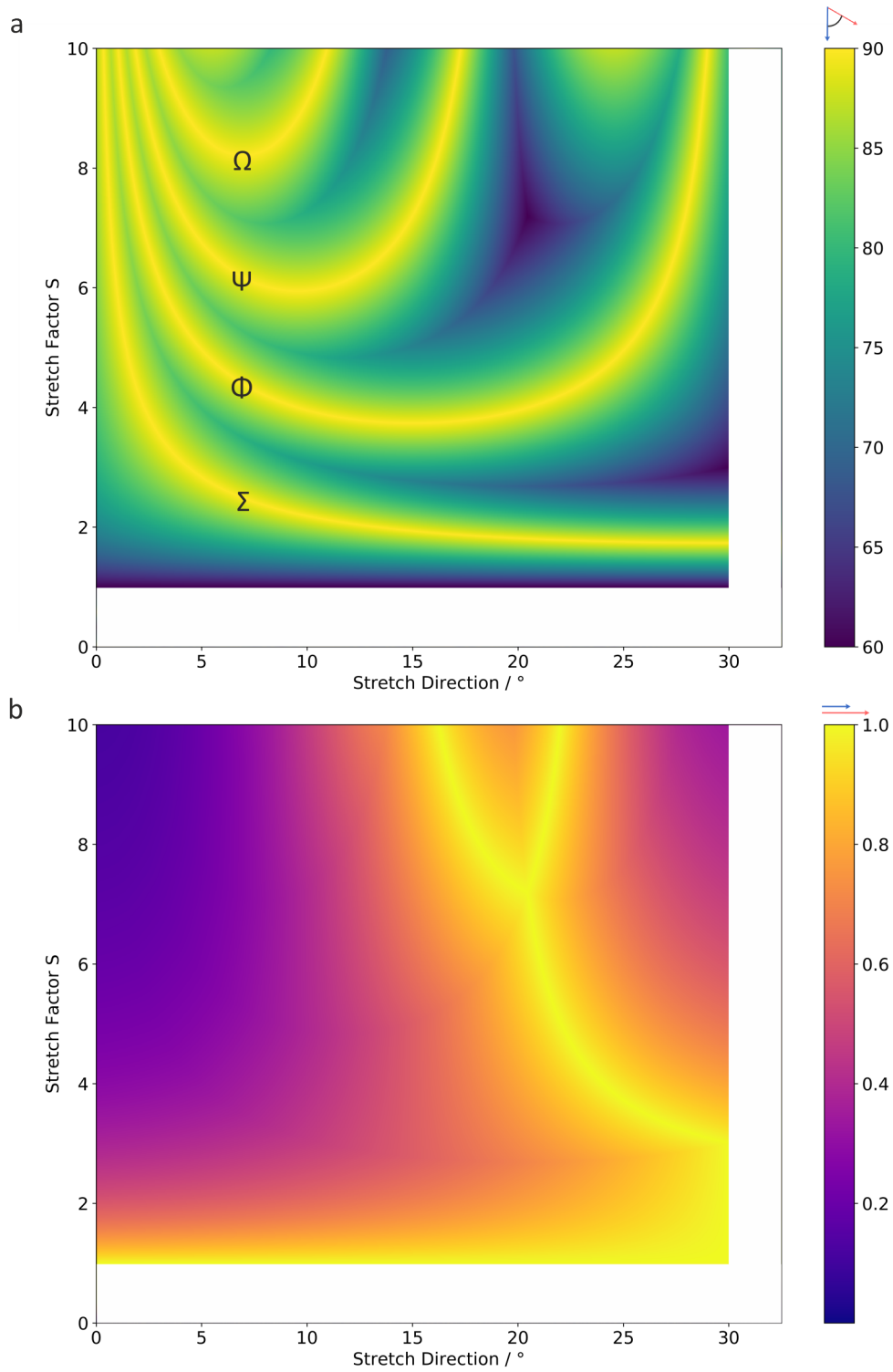


Figure 4.13: Expanded phase diagram as a function of the stretching factor  $S$  and stretching direction  $\beta$ . (a) Phase diagram with the color bar showing the angle between the base vectors of the individual stretching branches ( $\Sigma$ ,  $\Phi$ ,  $\Psi$ ,  $\Omega$ ). (b) Phase diagram with the color bar showing the ratio between the lengths of the base vectors.

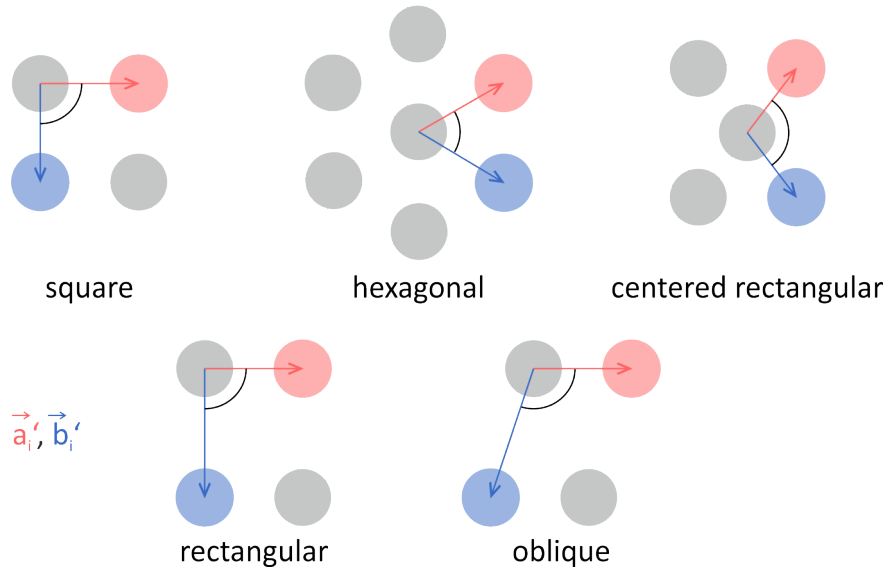


Figure 4.14: Definition of Bravais lattices in two dimensions.

$$S = \frac{x' - x(\delta) \cdot \cos^2 \alpha + y(\delta) \cdot \sin \alpha \cdot \cos \alpha}{x(\delta) \cdot \sin^2 \alpha + y(\delta) \cdot \sin \alpha \cdot \cos \alpha} \quad (4.12)$$

where  $x'$ ,  $y'$  are the coordinates of the stretched vectors  $\vec{a}'$  and  $\vec{b}'$ , and  $x(\delta)$ ,  $y(\delta)$  are the coordinates of the initial vectors  $\vec{a}$  and  $\vec{b}$ . For this purpose, the stretched vectors  $\vec{a}'$  and  $\vec{b}'$  with the coordinates are associated with particle positions in SEM images. As the initial vectors are unknown, the calculation of  $\alpha$  and  $S$  is dependent on a screening of the parameter  $\delta$ , which defines the orientation of the original hcp structure,  $x(\delta)$  and  $y(\delta)$ . An exemplary calculation of the reconstruction of a stretching process is shown in Figure 4.15 and Table 4.1.

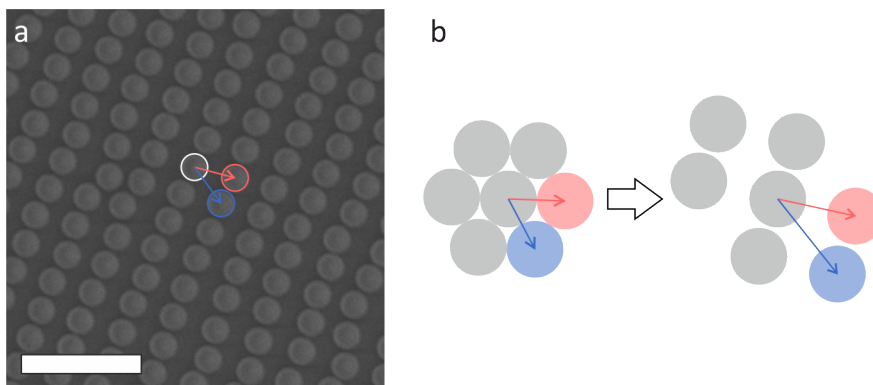


Figure 4.15: Reconstruction of stretching parameters from SEM image. (a) SEM image of stretched particle array symmetries with highlighted vectors. Scale bar is  $2 \mu\text{m}$ . (b) Schematic illustration of initial hcp structure with  $\delta = -2^\circ$  and stretched structure as a result of a stretching process with  $\alpha = 132^\circ$  and  $S = 1.73$ .

Table 4.1: Calculation of stretching parameters for SEM image in Figure 4.15 with  $\vec{a}'$ :  $x = 1.412, y = -0.405$  and  $\vec{b}'$ :  $x = 0.980, y = -1.348$ .

$\delta$	$\vec{a}'$		$\vec{b}'$		$\Delta\alpha$	$\Delta S$
	$\alpha$	$S$	$\alpha$	$S$		
-180°	100°	1.48	146°	1.67	46°	0.19
...						
-4°	129°	1.65	130°	1.77	1°	0.12
-3°	130°	1.68	131°	1.75	1°	0.07
-2°	132°	1.72	132°	1.73	0°	0.01
-1°	133°	1.76	134°	1.72	1°	0.04
...						
180°	100°	1.48	146°	1.67	46°	0.19

The averaged coordinates of the indicated vectors are extracted from the SEM image and inserted into the equations for the calculation of  $\alpha$  and  $S$ . The values of  $\alpha$  and  $S$  are calculated for  $\delta = [-180^\circ; 180^\circ]$ . An extract of this calculation is given in Table 4.1. It can be seen that  $\alpha$  and  $S$  usually differ for the individual calculations with  $\vec{a}'$  and  $\vec{b}'$ . Only for one value of  $\delta$  there is a match of  $\alpha$  and  $S$ . In the present case, this is applicable for  $\delta = -2^\circ$ . Consequently, the stretching parameters  $\alpha = 132^\circ$  and  $S = 1.73$  can be assigned to the SEM image in Figure 4.15 a. This procedure can be applied to any SEM image of a stretched monolayer in order to ascertain the proceeded stretching. Furthermore, it was shown that the calculated stretching parameters are valid throughout the entire substrate (Figure 4.16). This means, that independent of the initial orientation of a domain, similar stretching parameters are applied during immersion. The domains A and B had significantly different orientations in the hcp structure,  $\delta = 23^\circ$  and  $\delta = -16^\circ$ . Nevertheless, the individually calculated values for  $\alpha$  and  $S$  match very well.

#### 4.4 Influence of the immersion direction during transfer

As already described above, the preparation of non-close-packed structures is dependent on two experimental parameters: stretching direction and stretching factor. The stretching direction is defined by the orientation of the hcp structure and the immersion direction of the substrate. For sufficiently large particles, the transfer process of the hcp monolayer from the water/air interface onto the hydrophobic substrate can be tracked by light microscopy (Figure 4.17). Thereby, the initial orientation of the hexagonal particle array can be directly associated with the non-close-packed structure on the substrate. Thus, for large domain sizes of particles visible by light microscopy, the immersion direction can be aligned with respect to the domain orientation. As a result, the stretching

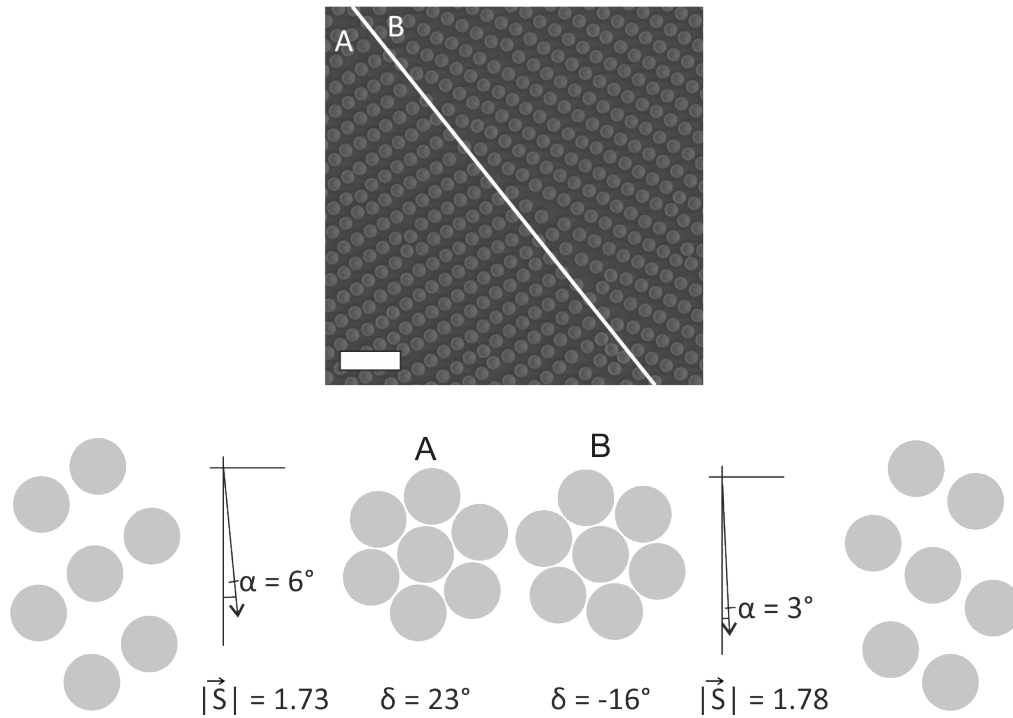


Figure 4.16: SEM image of a domain boundary with two differently oriented domains A and B. The analysis of the experimentally obtained structures shows that similar stretching parameters are applicable for both domains. The small deviations are attributed to local fluctuations of the contact line. Scale bar is  $2 \mu\text{m}$ .

direction can be individually adjusted to obtain the desired structure.

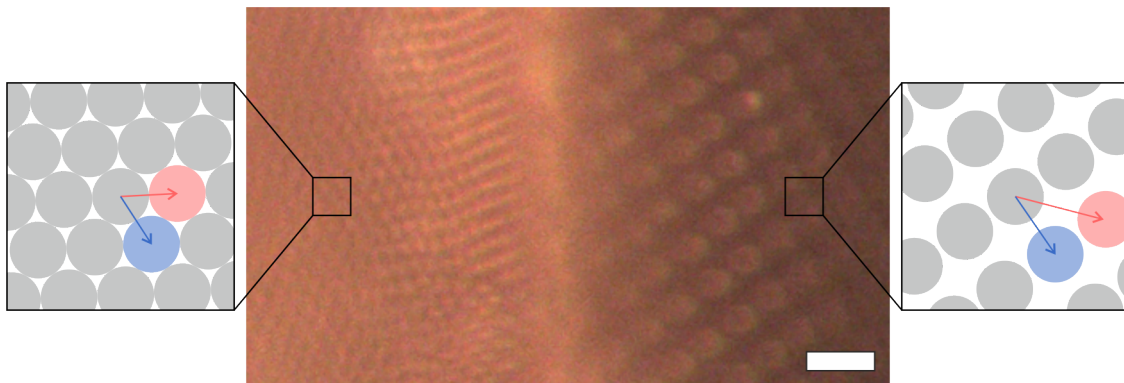


Figure 4.17: Microscope image (top view) of the transfer from a hcp structure at the water/air interface (left) onto a hydrophobic substrate (right). Scale bar is  $5 \mu\text{m}$ .

#### 4.5 Influence of the contact angle of the substrate

In addition, it was demonstrated that the stretching factor  $S$  can also be well controlled via the hydrophobic nature of the substrate. Figure 4.18 shows that the contact angle  $\theta$  of the substrate defines the magnitude of stretching. The higher the contact angle of the substrate, the lower is the stretching factor, which eventually approaches  $S = 1$ .

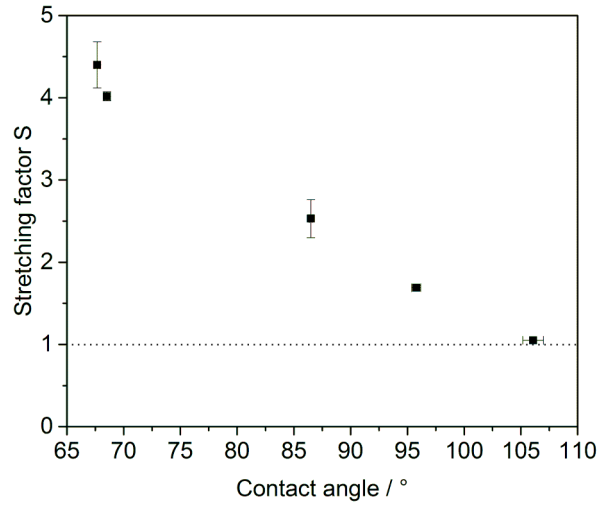


Figure 4.18: Dependence of the stretching factor  $S$  on the contact angle  $\theta$  of the substrates.

A wide range of contact angles was realized by different hydrophobic polymers used as substrates. These polymers were either spin-coated on glass slides or directly used in form of films. These substrates covered an adequate span of contact angles ranging from polytetrafluoroethylene (PTFE) ( $\theta = 106^\circ$ ), PS ( $\theta = 96^\circ$ ), P(nBA-co-S) ( $\theta = 86^\circ$ ), SU-8 photoresist ( $\theta = 69^\circ$ ) to poly(methyl methacrylate) (PMMA) ( $\theta = 68^\circ$ ). The corresponding stretching factor could thereby be adjusted between  $1 \lesssim S \lesssim 4.5$ . Using the different substrates led consequently to a large structural diversity after stretching starting from the same hcp monolayer at the water/air interface. An overview of a small selection of accessible two-dimensional arrays is depicted in Figure 4.19.

A high contact angle of the substrates (PTFE,  $\theta = 106^\circ$ ) has only a small influence on the transfer of the monolayer ( $S \sim 1$ ). The transferred structures exhibit a hcp arrangement with scarce distortion (Figure 4.19 a). For slightly lower contact angles (PS,  $\theta = 96^\circ$ ) the monolayer is moderately stretched. The observed structures feature predominantly square, rhombic or slightly oblique lattices (Figure 4.19 b) as expected from the phase diagram in Figure 4.12. Further lowering the contact angle of the substrates leads to gradually higher stretching factors. Particle arrays with rectangular, oblique and non-close-packed hexagonal domains (Figure 4.19 c) are typically found on substrates with intermediate contact angles (P(nBA-co-S),  $\theta = 86^\circ$ ). At the bottom end of contact angles that enable a hydrophobic transfer of the monolayer from the water/air interface to a substrate, the highest stretching factors were discovered. These substrates (SU-8,  $\theta = 69^\circ$ ; PMMA,  $\theta = 68^\circ$ ) promoted the formation of large tetragons and extended particle lines (Figure 4.19 d/e).

The dependence of transfer dynamics on the substrate contact angle  $\theta$  has been already observed by Cerro<sup>[28]</sup>. Cerro investigated flow patterns in the subphase during immer-

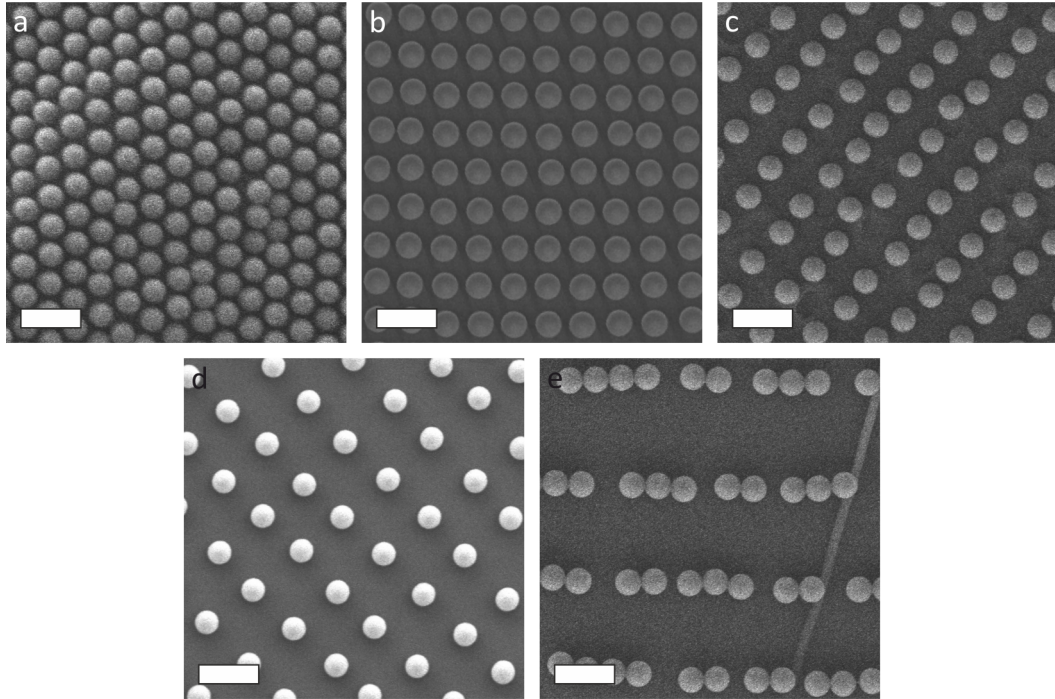


Figure 4.19: SEM images of polymer particles on substrates with different contact angles. (a) PTFE film ( $\theta = 106^\circ$ ), (b) PS ( $\theta = 96^\circ$ ), (c) P(nBA-co-S) ( $\theta = 86^\circ$ ), (d) SU-8 ( $\theta = 69^\circ$ ), (e) PMMA ( $\theta = 68^\circ$ ). Scale bars are  $1 \mu\text{m}$ .

sion of the substrate and linked the effect of contact angles to transfer phenomena at the three phase contact line.

In this work, a critical contact angle of  $\theta_c \sim 65^\circ$  was observed. For contact angles smaller than  $\theta_c$ , the subphase shows a splitting streamline (Figure 4.20 left). The split-injection streamline pattern is characterized by a liquid phase, where the liquid near the contact line is displaced by liquid from the bulk phase. As a result, the interface moves away from the immersed substrate. X-type transfer, which describes monolayers deposited during immersion, is therefore impossible for  $\theta < \theta_c$ . This flow pattern is typically observed for deposition on glass by immersion through the water/air interface due to the small contact angle.

In the opposite case for  $\theta > \theta_c$ , the interface moves towards the three phase contact line (Figure 4.20 right). Such conditions can be realized by treating glass with hydrophobic agents or application of hydrophobic polymers. For these substrates X-type transfer takes place. However, it is crucial to notice that the interface moves not necessarily at the same speed as the substrate does. Thereby, the velocity of the interface is not dependent on the immersion speed, but rather on the contact angle of the substrate. For contact angles  $\theta \sim \theta_c$  the interface hardly moves towards the contact line, so that the transfer ratio is very low. In other words, this signifies a large stretching factor as the ratio between the immersed substrate area  $A_{sub}$  and transferred monolayer area  $A_{mon}$  is high ( $S = A_{sub}/A_{mon}$ ). Increasing the contact angle beyond  $\theta_c$ , leads to higher flow ve-

locities of the monolayer towards the substrate, thus decreasing the stretching factor. For large contact angles ( $\theta \simeq 105^\circ$ ) the transfer ratio approaches unity, as the velocity of the substrate and the interface eventually become equal. Consequently, the stretching factor becomes  $S \sim 1$ .

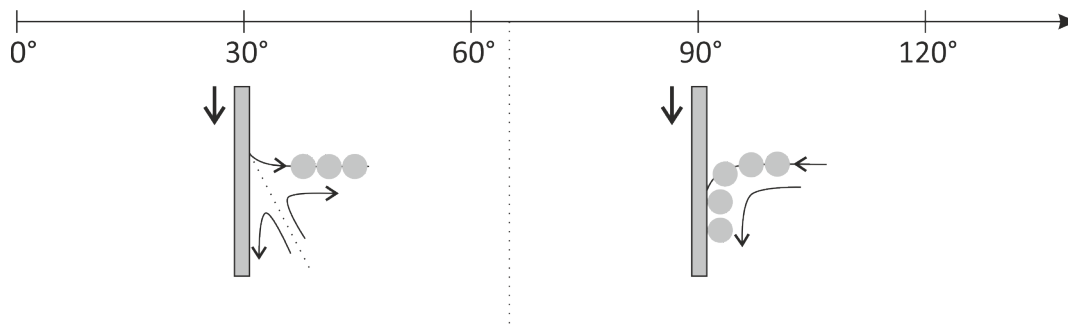


Figure 4.20: Streamline profiles upon immersion of a solid substrate at different contact angles. The dotted line indicates the critical angle  $\theta_c$  below which an X-type is impossible. Adapted from *Journal of Colloid and Interface Science*, 257 (2), R. L. Cerro, Moving contact lines and Langmuir–Blodgett film deposition, 276-283, Copyright 2003, with permission from Elsevier.<sup>[28]</sup>

The robustness of the method is further characterized by the fact that the immersion velocity of the substrate ( $1 \text{ mm min}^{-1} - 10 \text{ mm s}^{-1}$ ) and the immersion angle ( $30^\circ - 90^\circ$ ) have no significant influence on the stretching process. The effect that polycrystallinity leads to different structures within one sample is not imperatively a limitation, as excellent techniques have been reported to reach large-scale single crystalline structures.<sup>[29,30]</sup> Figure 4.21 shows an optical microscopy image of large area, single-crystalline domains and correlative electron microscopy. Two extended single-crystalline domains can be discerned from the distinct scattering colors corresponding to different domain orientations. Whereas the initial orientation of the domains to the stretching direction differs, they feature the same absolute stretching factor  $S \sim 1.7$ . This is demonstrated by the correlative electron microscopy images which show identical structures within the whole single-crystalline areas.

Moreover, even with the presented method is possible to identify the different structures present within a sample by simple laser diffraction experiments which indicates large single crystalline areas (Figure 4.22). The diffraction patterns reveal rectangular (Figure 4.22 a), particle lines (Figure 4.22 b), oblique (Figure 4.22 c), and square structures (Figure 4.22 d).

The presented technique potentially offers a new approach to enable the preparation of a large variety of defined ordered particle arrays to tune their optical, photonic and wetting properties to specific applications. Furthermore, the method is compatible with batch and continuous solution surface processing methods with immediate implications for the generation of ordered particle arrays on a variety of solid and flexible substrates.

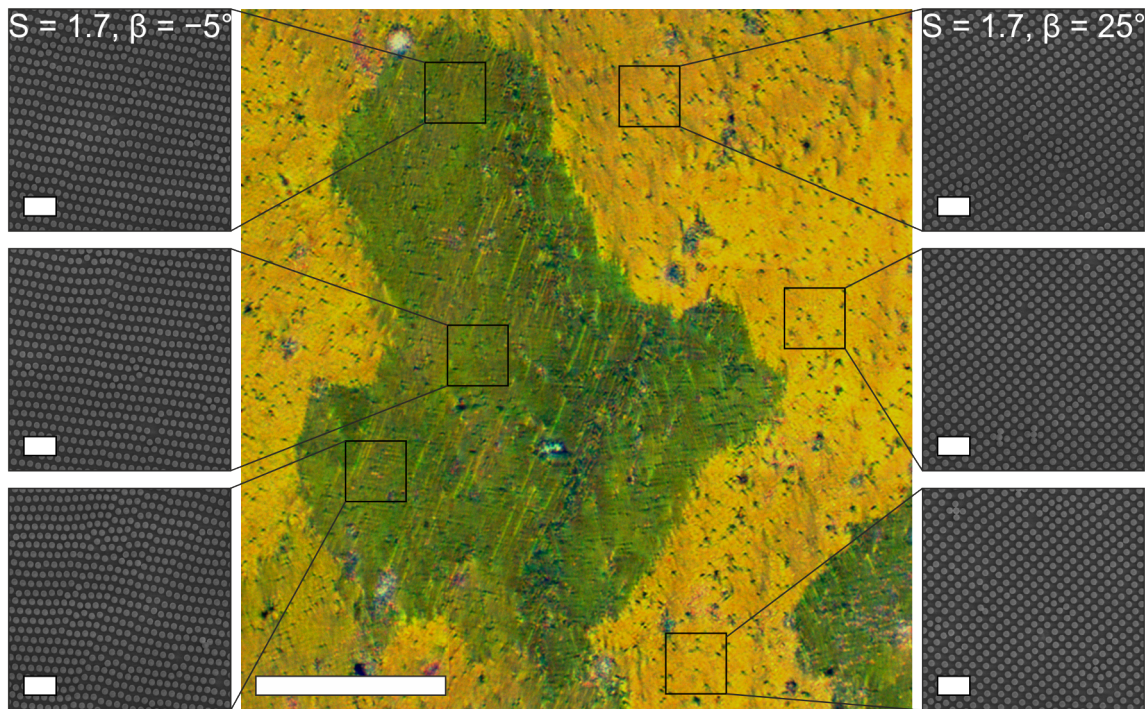


Figure 4.21: Optical microscopy image of large area, single-crystalline domains and correlative electron microscopy. Scale bars are  $50 \mu\text{m}$  (optical microscopy) and  $2 \mu\text{m}$  (electron microscopy).

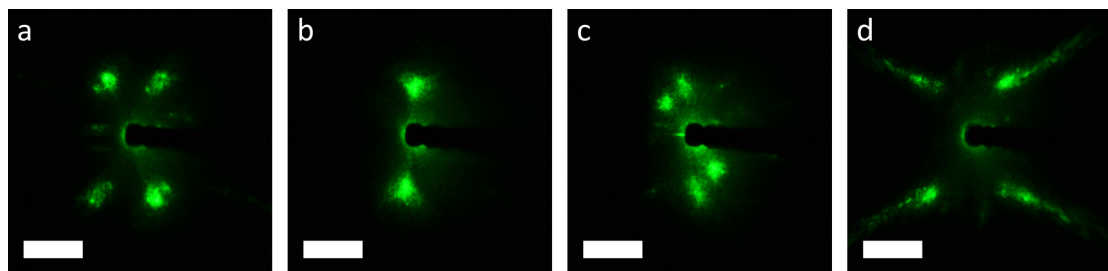


Figure 4.22: Laser diffraction images from a sample with different non-close-packed structures: (a) rectangular, (b) particle lines, (c) oblique and (d) square. Scale bars are  $5 \text{ mm}$ .

## 4.6 Appendix

Particle positions and diameters were determined from the SEM images using MATLAB's circle detection function (Figure 4.23 a). From the particle positions, the average stretched basis vectors  $\vec{a}'$  and  $\vec{b}'$  were then determined by averaging all interparticle vectors with a Python script provided by B. A. F. Kopera (Physical Chemistry I – Polymer Systems, University of Bayreuth) (Figure 4.23 b).

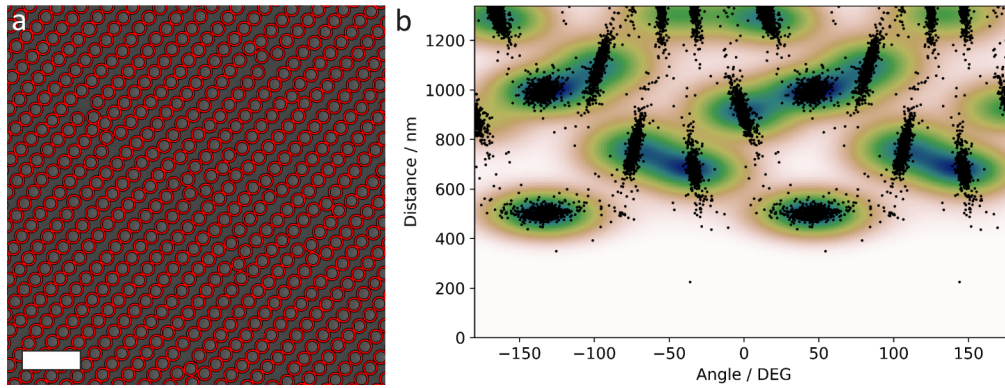


Figure 4.23: (a) SEM image of a stretched particle array. The red circles indicate the particles found by MATLAB's circle detection function after optimizing the search parameters manually. Scale bar is  $2 \mu\text{m}$ . (b) 2D Histogram of the distance between particle pairs and the corresponding angle with the x-axis for the SEM image in (a). Each black dot represents an inter-particle connection. A Gaussian kernel density estimator is used to calculate the smooth distribution function (color). Local maxima in the distribution, with small interparticle distances, represent possible candidates for the stretched basis vectors  $\vec{a}'$  and  $\vec{b}'$  in polar coordinates.

## References

- [1] Nemiroski, A.; Gonidec, M.; Fox, J. M.; Jean-Remy, P.; Turnage, E.; Whitesides, G. M. Engineering Shadows to Fabricate Optical Metasurfaces. *ACS Nano* **2014**, *8*, 11061–11070.
- [2] Romanov, S. G.; Vogel, N.; Bley, K.; Landfester, K.; Weiss, C. K.; Orlov, S.; Korovin, A. V.; Chuiko, G. P.; Regensburger, A.; Romanova, A. S.; Kriesch, A.; Peschel, U. Probing guided modes in a monolayer colloidal crystal on a flat metal film. *Physical Review B* **2012**, *86*, 195145.
- [3] Vogel, N.; Weiss, C. K.; Landfester, K. From soft to hard: the generation of functional and complex colloidal monolayers for nanolithography. *Soft Matter* **2012**, *8*, 4044–4061.
- [4] Li, Y.; Cai, W.; Duan, G. Ordered Micro/Nanostructured Arrays Based on the Monolayer Colloidal Crystals. *Chemistry of Materials* **2008**, *20*, 615–624.
- [5] Yang, S. M.; Jang, S. G.; Choi, D. G.; Kim, S.; Yu, H. K. Nanomachining by colloidal lithography. *Small* **2006**, *2*, 458–75.
- [6] Ai, B.; Yu, Y.; Möhwald, H.; Zhang, G.; Yang, B. Plasmonic films based on colloidal lithography. *Advances in Colloid and Interface Science* **2014**, *206*, 5–16.
- [7] Cumpston, B. H. et al. Two-photon polymerization initiators for three-dimensional optical data storage and microfabrication. *Nature* **1999**, *398*, 51.
- [8] Drotlef, D.-M.; Stepien, L.; Kappl, M.; Barnes, W. J. P.; Butt, H.-J.; del Campo, A. Insights into the Adhesive Mechanisms of Tree Frogs using Artificial Mimics. *Advanced Functional Materials* **2013**, *23*, 1137–1146.
- [9] Vogel, N.; Retsch, M.; Fustin, C. A.; Del Campo, A.; Jonas, U. Advances in colloidal assembly: the design of structure and hierarchy in two and three dimensions. *Chemical Reviews* **2015**, *115*, 6265–311.
- [10] Stelling, C.; Bernhardt, C.; Retsch, M. Subwavelength Etched Colloidal Monolayers: A Model System for Tunable Antireflective Coatings. *Macromolecular Chemistry and Physics* **2015**, *216*, 1682–1688.
- [11] Fenollosa, R.; Meseguer, F. Non-Close-Packed Artificial Opals. *Advanced Materials* **2003**, *15*, 1282–1285.
- [12] Isa, L.; Kumar, K.; Muller, M.; Grolig, J.; Textor, M.; Reimhult, E. Particle lithography from colloidal self-assembly at liquid-liquid interfaces. *ACS Nano* **2010**, *4*, 5665–70.
- [13] Law, A. D.; Buzza, D. M.; Horozov, T. S. Two-dimensional colloidal alloys. *Physical Review Letters* **2011**, *106*, 128302.

- [14] Vogel, N.; Goerres, S.; Landfester, K.; Weiss, C. K. A Convenient Method to Produce Close- and Non-close-Packed Monolayers using Direct Assembly at the Air-Water Interface and Subsequent Plasma-Induced Size Reduction. *Macromolecular Chemistry and Physics* **2011**, *212*, 1719–1734.
- [15] Akinoglu, E. M.; Morfa, A. J.; Giersig, M. Understanding anisotropic plasma etching of two-dimensional polystyrene opals for advanced materials fabrication. *Langmuir* **2014**, *30*, 12354–61.
- [16] Plettl, A.; Enderle, F.; Saitner, M.; Manzke, A.; Pfahler, C.; Wiedemann, S.; Ziemann, P. Non-Close-Packed Crystals from Self-Assembled Polystyrene Spheres by Isotropic Plasma Etching: Adding Flexibility to Colloid Lithography. *Advanced Functional Materials* **2009**, *19*, 3279–3284.
- [17] Volk, K.; Fitzgerald, J. P.; Retsch, M.; Karg, M. Time-Controlled Colloidal Superstructures: Long-Range Plasmon Resonance Coupling in Particle Monolayers. *Advanced Materials* **2015**, *27*, 7332–7.
- [18] Quint, S. B.; Pacholski, C. Extraordinary long range order in self-healing non-close packed 2D arrays. *Soft Matter* **2011**, *7*, 3735–3738.
- [19] Vogel, N.; Fernandez-Lopez, C.; Perez-Juste, J.; Liz-Marzan, L. M.; Landfester, K.; Weiss, C. K. Ordered arrays of gold nanostructures from interfacially assembled Au@PNIPAM hybrid nanoparticles. *Langmuir* **2012**, *28*, 8985–93.
- [20] Spatz, J. P.; Mössmer, S.; Hartmann, C.; Möller, M.; Herzog, T.; Krieger, M.; Boyen, H.-G.; Ziemann, P.; Kabius, B. Ordered Deposition of Inorganic Clusters from Micellar Block Copolymer Films. *Langmuir* **2000**, *16*, 407–415.
- [21] Malaquin, L.; Kraus, T.; Schmid, H.; Delamarche, E.; Wolf, H. Controlled particle placement through convective and capillary assembly. *Langmuir* **2007**, *23*, 11513–21.
- [22] Khanh, N. N.; Yoon, K. B. Facile organization of colloidal particles into large, perfect one- and two-dimensional arrays by dry manual assembly on patterned substrates. *Journal of the American Chemical Society* **2009**, *131*, 14228–30.
- [23] Stelling, C.; Mark, A.; Papastavrou, G.; Retsch, M. Showing particles their place: deterministic colloid immobilization by gold nanomeshes. *Nanoscale* **2016**, *8*, 14556–64.
- [24] Yan, X.; Yao, J.; Lu, G.; Li, X.; Zhang, J.; Han, K.; Yang, B. Fabrication of non-close-packed arrays of colloidal spheres by soft lithography. *Journal of the American Chemical Society* **2005**, *127*, 7688–9.
- [25] Li, X.; Wang, T.; Zhang, J.; Yan, X.; Zhang, X.; Zhu, D.; Li, W.; Zhang, X.; Yang, B. Modulating two-dimensional non-close-packed colloidal crystal arrays by deformable soft lithography. *Langmuir* **2010**, *26*, 2930–6.

- [26] Retsch, M.; Zhou, Z.; Rivera, S.; Kappl, M.; Zhao, X. S.; Jonas, U.; Li, Q. Fabrication of Large-Area, Transferable Colloidal Monolayers Utilizing Self-Assembly at the Air/Water Interface. *Macromolecular Chemistry and Physics* **2009**, *210*, 230–241.
- [27] Weekes, S. M.; Ogrin, F. Y.; Murray, W. A.; Keatley, P. S. Macroscopic Arrays of Magnetic Nanostructures from Self-Assembled Nanosphere Templates. *Langmuir* **2007**, *23*, 1057–1060.
- [28] Cerro, R. L. Moving contact lines and Langmuir-Blodgett film deposition. *Journal of Colloid and Interface Science* **2003**, *257*, 276–83.
- [29] Shinotsuka, K.; Kajita, Y.; Hongo, K.; Hatta, Y. Crystal Perfection of Particle Monolayer at the Air-Water Interface. *Langmuir* **2015**, *31*, 11452–7.
- [30] Meng, X.; Qiu, D. Gas-flow-induced reorientation to centimeter-sized two-dimensional colloidal single crystal of polystyrene particle. *Langmuir* **2014**, *30*, 3019–23.

## 5 Preparation of quasicrystals by colloidal self-assembly

Chapter 4 showed that non-close-packed, non-hexagonal particle assemblies can be prepared by colloidal self-assembly at the water/air interface. These structures were obtained by using single particle types. For even more complex, aperiodic structures, binary particle mixtures are required. Many applications benefit from these ordered but aperiodic particle arrays to control and tune optical properties.

Especially, wave transport and interference in photonic crystals have been widely investigated in the past years and are of fundamental relevance for optical devices.<sup>[1]</sup> Materials with photonic band gap (PBG) are of great interest as the propagation of electromagnetic waves is forbidden in these structures for a distinct wavelength range.<sup>[2]</sup> Though there is a variety of periodic structures that can be exploited for PBG applications, it should be noted that also aperiodic structures, in particular quasicrystals, can interfere with light.<sup>[3]</sup> Quasicrystals are classified between periodic and disordered structures. Although they lack any periodicity, they feature sharp diffraction peaks due to their long range order. In contrast to periodic crystals, where the rotational symmetries are restricted to two, three, four and six, in aperiodic quasicrystals higher symmetries, such as, e. g. eight, ten, twelve or eighteen, are allowed.

After their discovery in 1984<sup>[4,5]</sup>, quasicrystalline structures have been mainly reported for intermetallic compounds. In these structures the quasicrystalline order is manifested on the atomic length scale. Consequently, they can interact on the sub-nanometer length scale, e. g. with electrons and influence the electronic properties.<sup>[6,7]</sup>

Only with the first discoveries of soft matter quasicrystals it became possible to fabricate quasicrystalline structures with lattice constants in the nanometer to micrometer range. At these length scales structures are able to interact with light and become relevant for advanced photonic applications. In recent years the number of quasicrystals in soft matter systems continuously increased, covering more and more different systems including supramolecular structures of organic dendrimers<sup>[8]</sup>, block copolymers<sup>[9-11]</sup>, and colloidal inorganic nanoparticles<sup>[12-15]</sup>. The variety of materials suggests that the formation of quasicrystals is not dependent on some special interaction, but rather there exists a generic mechanism that promotes quasicrystalline order.

This constitutes the motivation for the growing field of theoretical work about quasicrystals. The main focus of theoretical investigations lies on the origin and stability of quasicrystals and the corresponding driving forces. One basis of computer simulations is the characteristic orientation of neighboring colloids in quasicrystalline structures. When the colloids are connected via imaginary lines, a distinct tiling of triangles, tetragons and other polygons is obtained. Thereby, quasicrystalline patterns feature certain preferential orientations with local order, that is incompatible with periodicity. This order can be induced by the existence of competing length-scales or appropriate bond angles in a

system. Computer simulations realize distinct angles by patchy particles, whereas two length-scales can be generated by different particle pair potentials. In this respect, quasicrystalline structures have been found for various potentials, ranging from three-well potentials<sup>[16,17]</sup> over single soft potentials<sup>[18]</sup> to hard step potentials<sup>[19]</sup>. Whereas potentials with more than one minimum are difficult to rationalize with experimentally available systems, there are appropriate implementations of single soft and hard potentials. Soft potentials characterize very well, e. g. core-shell micelles, for which an increasing repulsive force exists for a progressive overlap of the shells. Hard step potentials better describe binary systems of spheres with two different sizes.

The theoretical work of Dotera *et al.*<sup>[19]</sup> and the first realization of a quasicrystalline structure from nanoparticles by Talapin *et al.*<sup>[12]</sup> were the inspiration for the following work to prepare two-dimensional quasicrystals with colloidal particles. For a system of hard spheres with two different sizes there are various tilings imaginable, but in principle only a tiling of squares and equilateral triangles is of special interest (Figure 5.1). This tiling is referred to an Archimedean-like tiling due to a revenant motif of two squares and three triangles meeting at one vertex with a  $3^2.4.3.4$  configuration, where the numbers symbolize the arrangement around the vertex. Whereas pure  $3^2.4.3.4$  patterns describe periodic structures, which belong to the Frank-Kasper phases<sup>[20]</sup>, smaller domains with  $3^2.4.3.4$  patterns within a structure without translational symmetry can be part of a quasicrystal with dodecagonal symmetry.

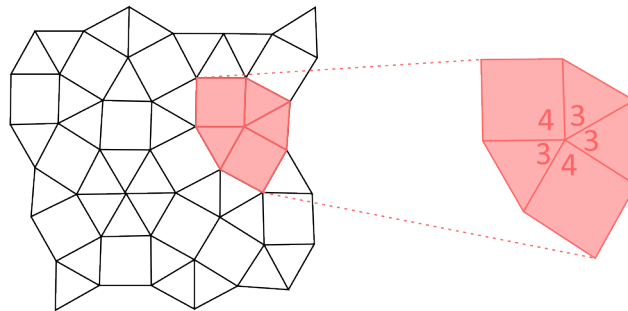


Figure 5.1: Dodecagonal quasicrystal with Archimedean-like tiling of squares and equilateral triangles showing the  $3^2.4.3.4$  configuration around many vertices.

In summary, there exist numerous theoretical papers, that predict the formation of quasicrystals for systems featuring two length scales. Moreover, the experimental results of self-assembled binary nanoparticle superlattices confirm the possibility to create quasicrystalline structures with particles of two different sizes. However, currently the self-assembly of binary quasicrystals has only been accomplished for particles in the lower nanometer range. An equivalent for colloidal particles has not yet been realized, but is of considerable interest for photonic applications.

## 5.1 Preparation of colloidal monolayers

This thesis presents a fabrication method for two-dimensional quasicrystalline colloidal monolayers from a binary particle mixture. Thereby, the work mainly focuses on the preparation of particle arrays with dodecagonal symmetry based on the square-triangle tiling described above. The quasicrystalline structure is constituted by the large particles only, which decorate the vertices, while the small particles work as placeholders. For this purpose, the binary particle mixtures are assembled at the water/air interface via an established method by Retsch *et al.*<sup>[21]</sup> In this method, the particles possess a certain degree of freedom during self-assembly, which allows them to take the appropriate place in the quasicrystalline tiling. The general procedure of the particle self-assembly is shown in Figure 5.2.

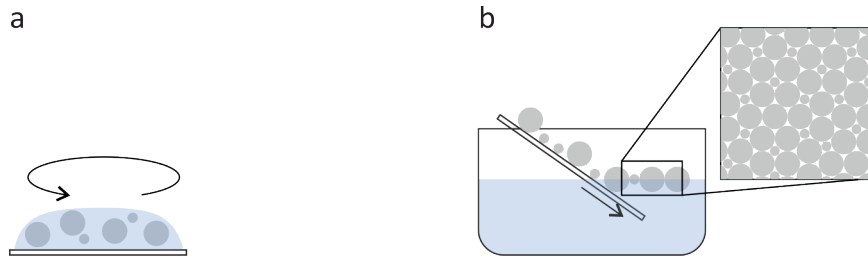


Figure 5.2: Fabrication of quasicrystalline colloidal monolayers by interfacial self-assembly. (a) A binary particle dispersion is spin-coated onto cationically functionalized glass slides. (b) Slow immersion of the glass slide into an aqueous solution of SDS at high pH yields a binary monolayer at the water/air interface.

The experiments were carried out with polystyrene (PS) particles of various sizes ranging from 300 nm – 1500 nm. The advantage of PS particles is the convenient synthesis, that yields particles over a wide range of diameters (100 nm – 5  $\mu\text{m}$ ) with narrow size distributions. For the major part of the work two model particles (small (S) and large(L) with a size ratio of  $\gamma_{S/L} = 0.42$  ( $d_S = 334$  nm,  $d_L = 800$  nm) were used. In the first step, particle mixtures with distinct concentration ratios were prepared from the individual particle dispersions. The binary mixtures with a total concentration of 3 wt% were subsequently spin-coated onto cationically functionalized glass slides (Figure 5.2 a). The positive surface charges on the glass induce a good distribution of individually separated particles. In the following step, the glass slide was slowly immersed into an aqueous solution of SDS and ammonia (pH 12). During immersion, the particles detached from the glass surface at the three-phase contact line. Thereby, they were transferred to the water/air interface, where they self-assembled into binary structures (Figure 5.2 b). In a final step, the colloidal monolayer could be collected on a hydrophilic substrate.

## 5.2 Theoretical analysis of quasicrystalline particle arrangements

Depending on the chosen size and concentration ratio of the particles, the self-assembly of binary mixtures leads to a variety of ordered and disordered structures. A lot of work has already investigated co-self-assembly of different types of particles as simple method for the fabrication of binary colloidal crystals. However, the reported results have in common that they mainly focused on periodic structures.<sup>[22]</sup> By contrast, quasicrystalline structures require distinct size and number ratios to obtain the desired tiling of particles.

From a theoretical point of view, there are two conceivable decorations of the Archimedean-like tiling with a binary particle mixture: a high density (HD) (Figure 5.3 a) and a low density (LD) (Figure 5.3 b) configuration. In the HD quasicrystal, three close-packed large particles form equilateral triangles. Squares consist of four large particles enclosing a single small particle (Figure 5.3 a). The LD quasicrystal features equilateral triangles with one centered, small particle and squares that accommodate four small particles (Figure 5.3 b).

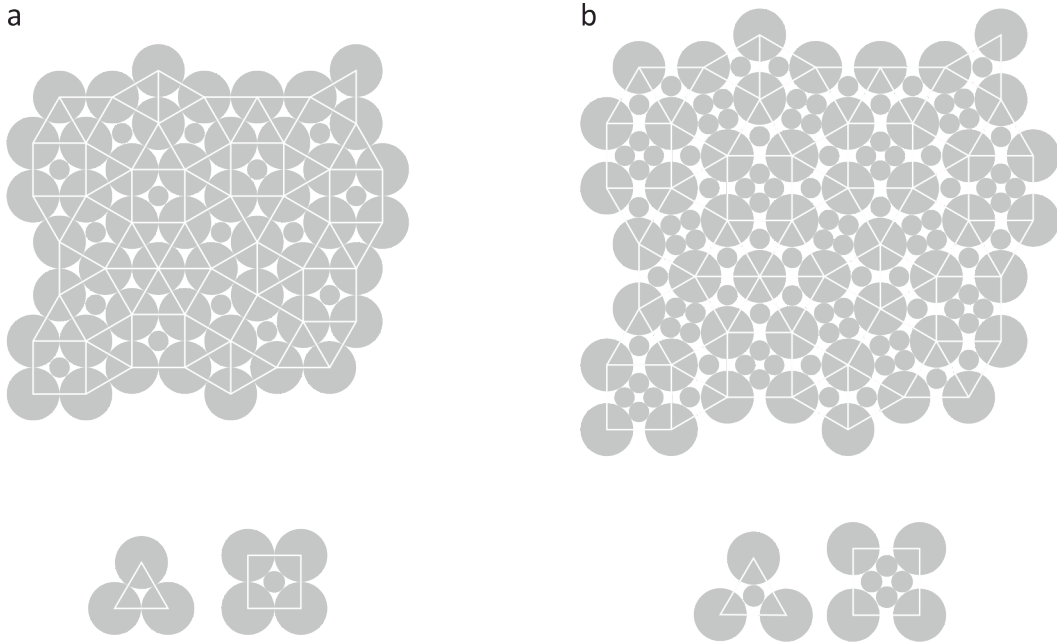


Figure 5.3: Decoration of an Archimedean-like square-triangle tiling. (a) High density dodecagonal square-triangle tiling. (b) Low density dodecagonal square-triangle tiling.

In order that small and large particles co-crystallize from a mixture into a quasicrystalline structure the two main experimental parameters, size ratio  $\gamma_{S/L} = d_S/d_L$  and the number ratio  $\alpha_{S/L} = N_S/N_L$  of the two types of particles, have to be matched.

Considering the size ratio, the largest single small particle that theoretically fits into the interstices of the squares in a HD dodecagonal quasicrystal has the size ratio  $\gamma_{S/L} = \sqrt{2} - 1 \approx 0.41$ . This can be calculated from geometrical considerations. In this case, the small particles are located in plane at the water/air interface with the large particles.

The required particle sizes for the decoration of the LD dodecagonal quasicrystal, which has been observed in self-assembled nanoparticle superlattices, are derived from Talapin *et al.*<sup>[12]</sup> They reported a size ratio of  $\gamma_{S/L} \approx 0.43$  as determining factor for the formation of a quasicrystalline phase. In this assembly none of the large particles are in close contact and the small particles have to pre-assemble into quadripartite arrangements. Due to the lower packing density and the more complex arrangement the LD quasicrystalline pattern is in practice less probable for colloidal particles.

The basis of the calculation of the particle number ratio is the requirement for quasicrystals that the area of the tiling occupied by triangles and squares has to be equal,  $A_{\square} = A_{\Delta}$ .<sup>[23]</sup> From this requirement, the number ratio of squares and triangles can be calculated using the area equations of the respective geometric shapes (square and equilateral triangle with a side length  $a$ ) and the number of squares and triangles,  $N_{\square}$  and  $N_{\Delta}$ .

$$N_{\square} \cdot a^2 = N_{\Delta} \cdot \frac{\sqrt{3}}{4} \cdot a^2 \quad (5.1)$$

$$\frac{N_{\square}}{N_{\Delta}} = \frac{\sqrt{3}}{4} \quad (5.2)$$

The particle number ratio is now dependent on the decoration of the square and triangular tiles with small and large particles. Thereby, squares and triangles are considered separately. The final stoichiometry of the particles is then derived from the individual unit cells (Figure 5.4).



Figure 5.4: Unit cells of the individual tiles in an Archimedean-like square-triangle tiling. (a) Unit cells of the HD decoration: triangle  $L_1S_0$ , square  $L_1S_1$ . (b) Unit cells of the LD decoration: triangle  $L_1S_2$ , square  $L_1S_4$ .

In the HD quasicrystal, one triangle is decorated by three large particles and one square by four large particles and one small particle. Consequently, the resulting unit cells can be assigned to  $L_1S_0$  for the triangles and  $L_1S_1$  for the square. For the calculation of the number of small and large particles, it has to be considered that a unit cell of the triangular tiles actually consists of two triangles. Therefore, a factor of 0.5 has to be added, as the calculation refers to per triangle. The number of small and large particles,  $N_S$  and  $N_L$ , is now calculated by multiplication of the number of squares and triangles in the tiling with the respective number of particles in the unit cells,  $N_{S,\Delta}$ ,  $N_{S,\square}$ ,  $N_{L,\Delta}$  and  $N_{L,\square}$ .

$$N_S = N_{\Delta} \cdot N_{S,\Delta} \cdot \frac{1}{2} + N_{\square} \cdot N_{S,\square} = 1 \cdot 0 \cdot \frac{1}{2} + \frac{\sqrt{3}}{4} \cdot 1 = \frac{\sqrt{3}}{4} \quad (5.3)$$

$$N_L = N_{\Delta} \cdot N_{L,\Delta} \cdot \frac{1}{2} + N_{\square} \cdot N_{L,\square} = 1 \cdot 1 \cdot \frac{1}{2} + \frac{\sqrt{3}}{4} \cdot 1 = \frac{1}{2} + \frac{\sqrt{3}}{4} \quad (5.4)$$

This corresponds to a stoichiometry of the HD quasicrystal of  $L_{\frac{1}{2} + \frac{\sqrt{3}}{4}} S_{\frac{\sqrt{3}}{4}}$  which is approximately  $LS_{0.46}$ . An analogous calculation for the LD quasicrystal with the unit cells  $L_1S_2$  and  $L_1S_4$  for the triangles and the squares, respectively, leads to the following stoichiometry of  $L_{\frac{1}{2} + \frac{\sqrt{3}}{4}} S_{1 + \sqrt{3}}$  ( $LS_{2.93}$ ). Thus, the HD quasicrystal requires a number ratio of  $\alpha_{S/L} \approx 0.46$  and the LD quasicrystal a number ratio of  $\alpha_{S/L} \approx 2.93$ .

### 5.3 Influence of the particle number ratio

In order to investigate if the HD and LD structure are experimentally realizable, particle mixtures with the appropriate number ratios were prepared and assembled at the water/air interface. For both the HD and the LD phase, the model particles with a size ratio of  $\gamma_{S/L} = 0.42$  were used. This is an intermediate value which can fit for both structures.

Figure 5.5 shows scanning electron microscopy (SEM) images of the prepared monolayer for the particle mixture with  $\gamma_{S/L} = 0.42$  and  $\alpha_{S/L} = 0.46$  required for the HD quasicrystal. The individual large and small particles from several SEM images were counted which yielded an experimental stoichiometry of  $\alpha_{S/L} = 0.48$ . This is in good agreement with the theoretically calculated stoichiometry of the prepared mixture and indicates a homogeneous co-crystallization of the two types of particles. This impression is also given by the SEM overview image in Figure 5.5 a. Indeed, the fast Fourier transform (FFT) in the inset features twelve peaks which confirms the formation of a dodecagonal quasicrystalline pattern. Furthermore, the magnification in Figure 5.5 b shows the characteristic  $3^2 \cdot 4 \cdot 3 \cdot 4$  motifs of an Archimedean-like tiling with the particle decoration expected for the HD structure.

The homogeneity of the monolayer is further demonstrated by the photograph in Figure 5.6 a. At the same time, it can be seen that the domain sizes are comparatively small, as no grain boundaries are visible to the naked eye. However, with a focused laser beam it is possible to obtain a resolved diffraction pattern also featuring twelve peaks (Figure 5.6 b).

In comparison to the assembly of the HD quasicrystalline phase, also self-assembly experiments were performed for the formation of the predicted LD structure. For this purpose a particle mixture with  $\gamma_{S/L} = 0.42$  and  $\alpha_{S/L} = 2.93$  was prepared. The SEM images of this sample are depicted in Figure 5.7.

The SEM image in Figure 5.7 a characterizes very well the overall appearance of the

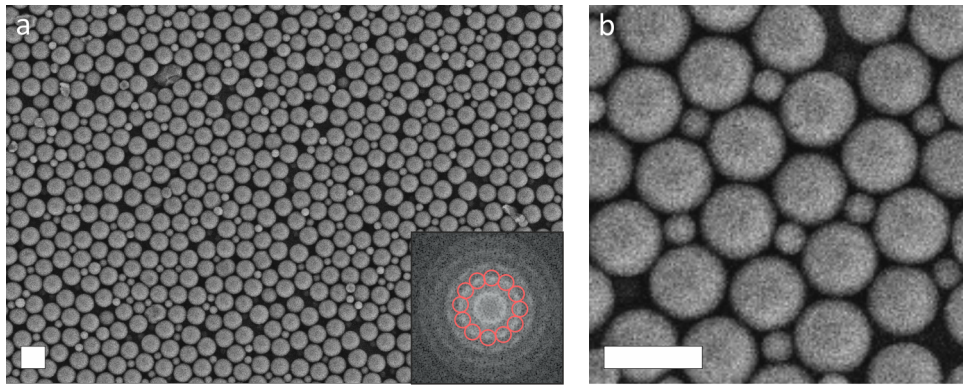


Figure 5.5: SEM images of binary particle monolayers with  $\gamma_{S/L} = 0.42$  and  $\alpha_{S/L} = 0.46$ . (a) Overview of the monolayer, with the inset showing the FFT with twelve-fold symmetry. (b) Magnification of (a) showing the characteristic  $3^2.4.3.4$  motifs of an Archimedean-like tiling. Scale bars are  $1 \mu\text{m}$ .

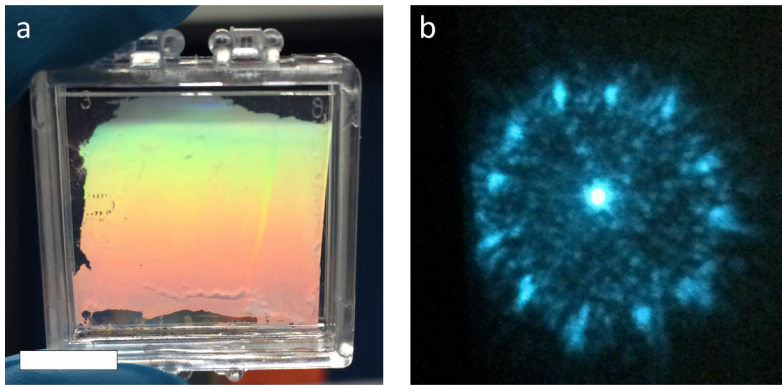


Figure 5.6: (a) Photograph of the particle monolayer with  $\gamma_{S/L} = 0.42$  and  $\alpha_{S/L} = 0.48$ . Scale bar  $1 \text{ cm}$ . (b) Laser diffraction obtained from the monolayer in (a) by a focused laser beam with a wavelength of  $488 \text{ nm}$ .

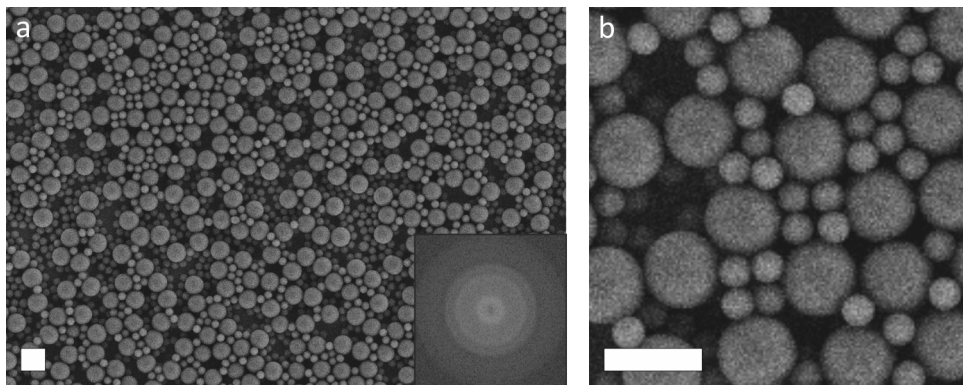


Figure 5.7: SEM images of binary particle monolayers with  $\gamma_{S/L} = 0.42$  and  $\alpha_{S/L} = 2.93$ . (a) Overview of the monolayer, with the inset showing the FFT of an amorphous distribution. (b) Magnification of (a) showing rare, individual particle arrangements that match the predicted decoration of the tiling. Scale bars are  $1 \mu\text{m}$ .

monolayer. The small and large particles do not form a homogeneous structure. Whereas there are small islands where the both particles are closely packed, there are other spots where larger accumulations of small particles promote the formation of disrupted structures. The FFT in the inset also suggests that there is no ordered structure. Nevertheless, the experimentally obtained averaged stoichiometry is with  $\alpha_{S/L} = 3.04$  in good agreement with the theoretical value. The magnification (Figure 5.7b) shows individual particle arrangements that match the predicted decoration in the LD structure, but they are rather rarely distributed in the monolayer. Overall, the high number of defects and inhomogeneities of the monolayer indicate that a decoration with the LD structure is not stable and cannot be realized experimentally using our model particles. In conclusion, this demonstrates that the number ratio is a crucial parameter to obtain intact structures.

#### 5.4 Influence of the particle size ratio

In order to further emphasize the importance of the size ratio, the impact of different particle sizes on the formed structures was investigated. Thereby, the number ratio of  $\alpha_{S/L} = 0.46$  was kept constant. While under these conditions a structure with twelve-fold symmetry was obtained for a particle size ratio of  $\gamma_{S/L} = 0.42$ , a lower or a higher size ratio yielded significantly different structures (Figure 5.8).

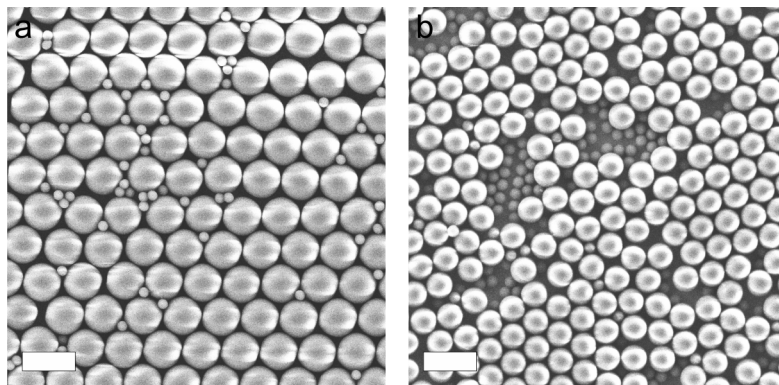


Figure 5.8: SEM images of binary particle monolayers with a theoretical number ratio of  $\alpha_{S/L} = 0.46$ . (a) Particle mixture with a size ratio of  $\gamma_{S/L} = 0.31$  (experimentally counted  $\alpha_{S/L} = 0.48$ ). (b) Particle mixture with a size ratio of  $\gamma_{S/L} = 0.45$  (experimentally counted  $\alpha_{S/L} = 0.51$ ). Scale bars are  $2\ \mu\text{m}$ .

For a lower size ratio ( $\gamma_{S/L} = 0.31$ ), the large particles assembled into a hexagonal close-packed structure (Figure 5.8 a). In this case, the small particles hardly interfered with the self-assembly. They are located mostly at the interstices of the hexagonal packed large particles. A few small particles are also between two large particles, yet this leads only to insignificant displacements.

For a higher size ratio ( $\gamma_{S/L} = 0.45$ ), the small and the large particles tend to phase separate to form individual islands of hexagonally packed structures (Figure 5.8 b). The

small particles do not fit anymore into the interstitial sites of the large particles, so that they interrupt a controlled self-assembly. This leads to small domains of the separately assembled particles.

Summarizing the results for varying size and number ratio, it was shown that only the HD quasicrystalline phase was experimentally realized with  $\gamma_{S/L} = 0.42$  and  $\alpha_{S/L} = 0.46$ . For all other deviant values either disordered or periodic structures were obtained.

## 5.5 Calculation of bond orientational order

In order to further support the results for the HD quasicrystalline phase, calculations of the bond orientational order (BOO) were performed. The bond orientational order parameter is a measure of the order in particle assemblies. In this case "bond" represents the lines that result from the assignment of nearest particle neighbors. Then, the angles between these bonds are used to calculate the average BOO parameter.<sup>[24]</sup> A BOO value of 1 denotes perfect order for a certain symmetry, whereas BOO values  $\ll 1$  signify that a certain symmetry is not present. These calculations can be used to verify that our structures actually concern a quasicrystalline arrangement rather than a twinned hexagonal structure, which would likewise feature twelve peaks in the FFT. Table 5.1 shows the results for the calculations of the BOO for the most commonly observed symmetries in crystalline and quasicrystalline structures. It can be seen that the maximal value is calculated for dodecagonal symmetry, whereas the value for the six-fold symmetry, which is an indication for twinned hexagonal structures, is significantly lower. The prevalence of the twelve-fold symmetry can also be seen in the 2D plot of the normalized bond vectors (Figure 5.9 a). Thereby, the twelve bright spots indicate the most frequent direction of imaginary bonds between the particles. As essentially the quasicrystalline structure is only manifested by the large particles - the small particles only have a directing function to stabilize the squares of four large particles - their positions were extracted and the FFT was re-calculated (Figure 5.9 b). This FFT has a better quality than the inset in Figure 5.5 a, because only the important information, positions of the large particles, is used for the calculation. Here, too, the existence of the dodecagonal quasicrystalline structure is confirmed. The FFT features three orders of peaks that are characteristic for a twelve-fold symmetry.

Table 5.1: Calculation of the BOO for the monolayer with  $\gamma_{S/L} = 0.42$  and  $\alpha_{S/L} = 0.46$ .

	<b>3-fold</b>	<b>4-fold</b>	<b>5-fold</b>	<b>6-fold</b>	<b>10-fold</b>	<b>12-fold</b>	<b>18-fold</b>
<b>BOO</b>	0.01	0.03	0.12	0.12	0.01	0.36	0.11

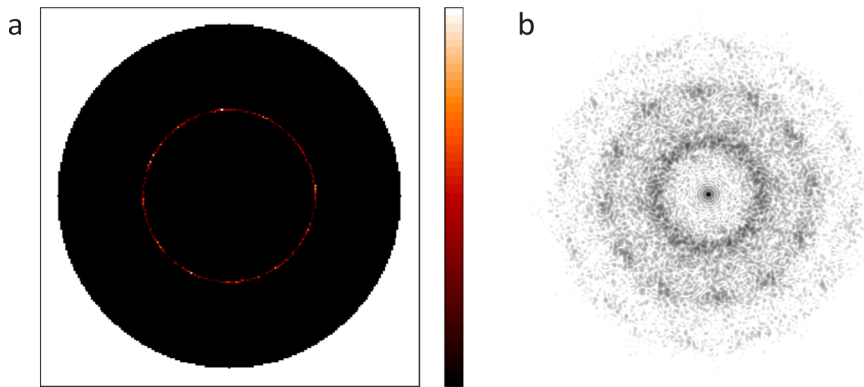


Figure 5.9: Calculations for the monolayer with  $\gamma_{S/L} = 0.42$  and  $\alpha_{S/L} = 0.46$ . (a) 2D plot of the normalized bond vectors. (b) FFT for the extracted positions of only the large particles.

## 5.6 Molecular dynamics simulations of binary particle mixtures

Besides the demonstration of the experimental concept, also theoretical simulations were performed. In these simulations the influence of the size and number ratio on the formation of quasicrystalline structures was investigated. Additionally, the electrostatic repulsion and the scope of electrostatic interaction were analyzed.

The basis of each molecular dynamics (MD) simulation is a 2D box filled with small and large particles of a distinct size and number ratio. The particles are well distributed and have broad distances from each other (Figure 5.10 a). During the simulation, the box decreases in size as the length of two opposite sides is reduced. This simulates the preparation of colloidal monolayers via the method of Retsch *et al.*<sup>[21]</sup>, where the available space is reduced in one dimension during immersion. In the experimental process the particles are also broadly distributed on a glass slide, before they are pushed into a densely packed arrangement at the water/air interface. The simulation proceeds until the particles cannot move any more and they freeze at their final position (Figure 5.10 b).

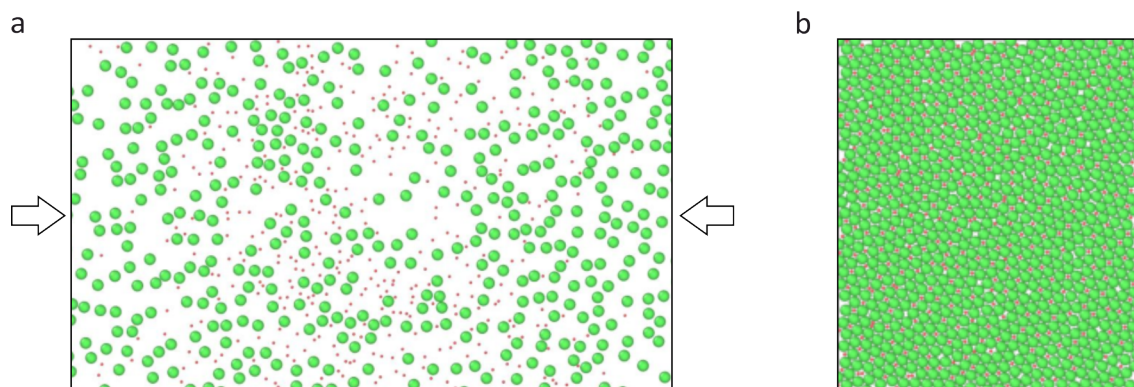


Figure 5.10: 2D box filled with small and large particles (a) at the beginning of a simulation and (b) at the end of a simulation.

Finally, the BOO of a 12-fold symmetry is calculated for the particle arrangements in the tight boxes. The MD simulations were performed for size ratios  $\gamma_{S/L} = 0.15 - 0.45$  and varying electrostatic repulsion between the small particles ( $E_S$ ) and the large particles ( $E_L$ ). Figure 5.11 gives an overview of the results for these simulations.

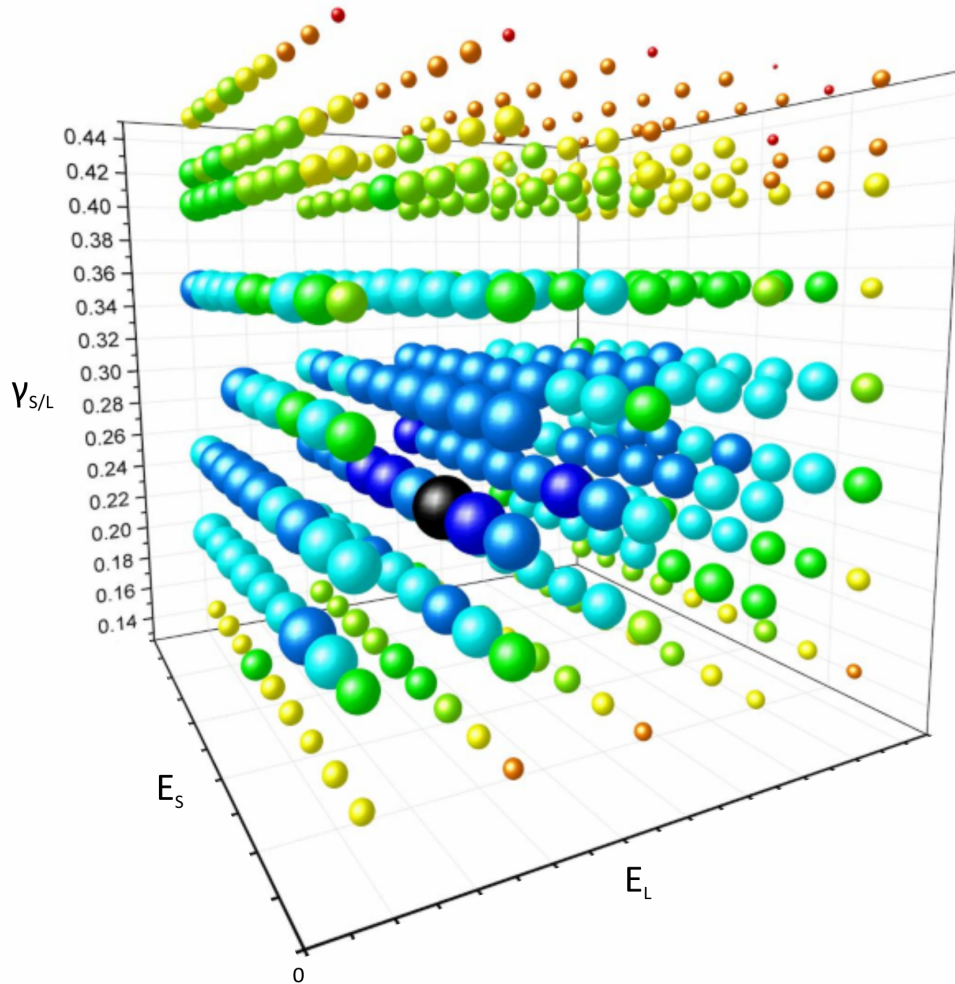


Figure 5.11: 3D diagram of the values for 12-fold BOO from the results of varying size ratio  $\gamma_{S/L}$ , electrostatic repulsion between the small particles  $E_S$  and the large particles  $E_L$ . The values of the BOO increase from the small, red spheres to the large, blue spheres. The black sphere represents the highest BOO value of 0.65.

The colors and the sizes of the spheres represent the value of the BOO for 12-fold symmetry. Thereby, the small, red spheres constitute low values for the BOO, whereas the large, blue spheres stand for high values of the BOO. The black sphere represents the highest value of 0.65. The 3D diagram nicely shows the main trends for the investigated parameters.  $E_S$  and  $E_L$  both have only minor effects on the BOO value, whereas for  $\gamma_{S/L}$  a clear optimum range can be observed. The highest values for a 12-fold BOO are obtained for a  $\gamma_{S/L}$  between 0.2 and 0.3. This is lower than the experimental results with  $\gamma_{S/L} = 0.42$ . A reason for this discrepancy could be the fact that the simulation is truly 2D. However,

the experiments take place at the water/air interface where firstly the exact position of the particles in  $z$  direction is unknown. Secondly, during assembly the particle position in  $z$  direction can be shifted due to attractive forces. This leads to a 2.5D behavior in the experiments so that  $\gamma_{S/L}$  can shift to higher values than theoretically calculated.

For a more detailed view on the effects of each parameter two sections were made through the 3D diagram, which meet at the black sphere. The diagrams show the dependence of the 12-fold BOO on  $\gamma_{S/L}$  and  $E_S$  (Figure 5.12) and on  $\gamma_{S/L}$  and  $E_L$  (Figure 5.13).

In Figure 5.12 it can be seen that the 12-fold BOO varies only slightly along the  $E_S$  axis. Only for very low and very high values of  $E_S$  the decrease of the BOO is more pronounced. By contrast, there is a strong dependence of the 12-fold BOO on  $\gamma_{S/L}$ . The best results are obtained for  $\gamma_{S/L} = 0.25$ . However, the BOO value significantly decreases for higher and lower size ratios. In the case of low size ratios the small particles fit into the interstices of hexagonally packed large particles, whereas for high size ratios the small and large particles phase separate. In both cases, no 12-fold symmetry can evolve. This is equivalent to the results from the experiments, where the formation of 12-fold symmetry was also observed only for a very narrow range of size ratios.

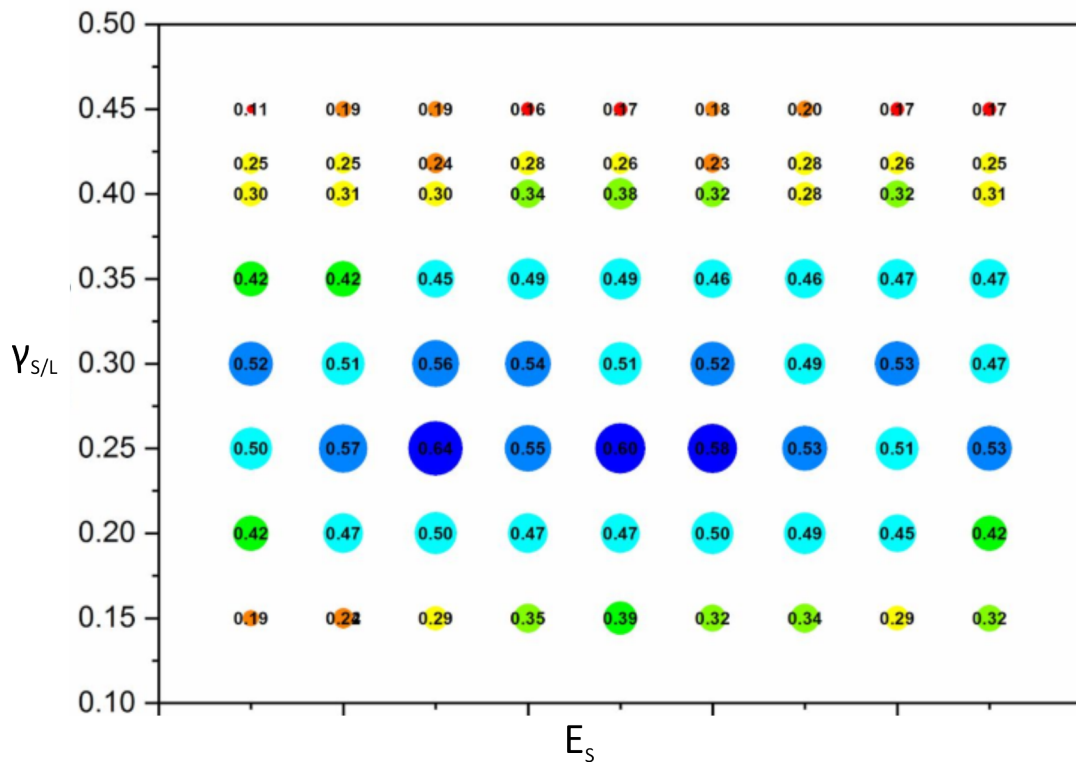


Figure 5.12: Dependence of the 12-fold BOO on the size ratio  $\gamma_{S/L}$  and electrostatic repulsion between the small particles  $E_S$ . The values of the BOO increase from the small, red circles to the large, blue circles.

In Figure 5.13 the 12-fold BOO is shown in dependence on  $\gamma_{S/L}$  and  $E_L$ . Different from  $E_S$ , here a trend can be observed for the BOO value along the  $E_L$  axis. Tendentially, better BOO values are observed for a weaker electrostatic repulsion between the large particles. This is reasonable, as the large particles need to come into narrow contact for the formation of a 12-fold symmetry. Furthermore,  $\gamma_{S/L}$  has again an optimum at 0.25. Here, too, the BOO drops significantly for other lower and higher size ratios.

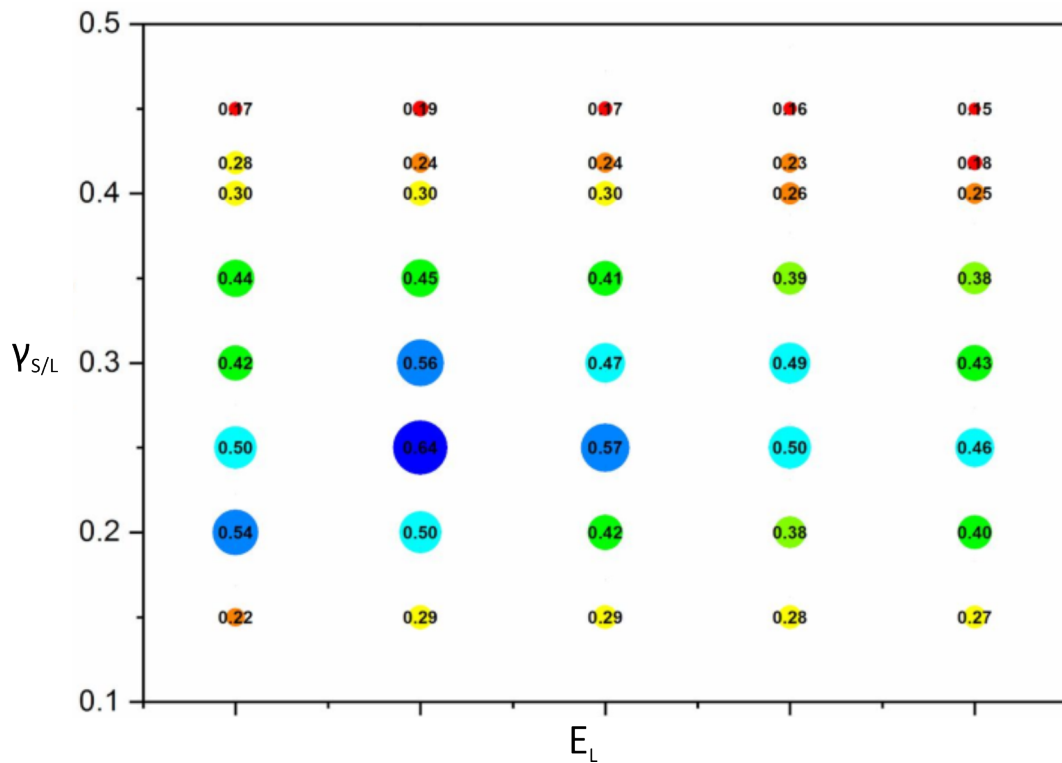


Figure 5.13: Dependence of the 12-fold BOO on the size ratio  $\gamma_{S/L}$  and electrostatic repulsion between the large particles  $E_L$ . The values of the BOO increase from the small, red circles to the large, blue circles.

The influence of the number ratio  $\alpha_{S/L}$  on the formation of structures with 12-fold symmetry is depicted in Figure 5.14. It can be seen that there is a significant maximum for the BOO at  $\alpha_{S/L} = 0.46$ . This is identical to the calculated value for the HD quasicrystalline phase and also identical to the experimental results. The diagram also reveals that the number ratio is a very sensitive parameter, whereby already small deviations from the optimum value hinder the formation of extended quasicrystalline structures.

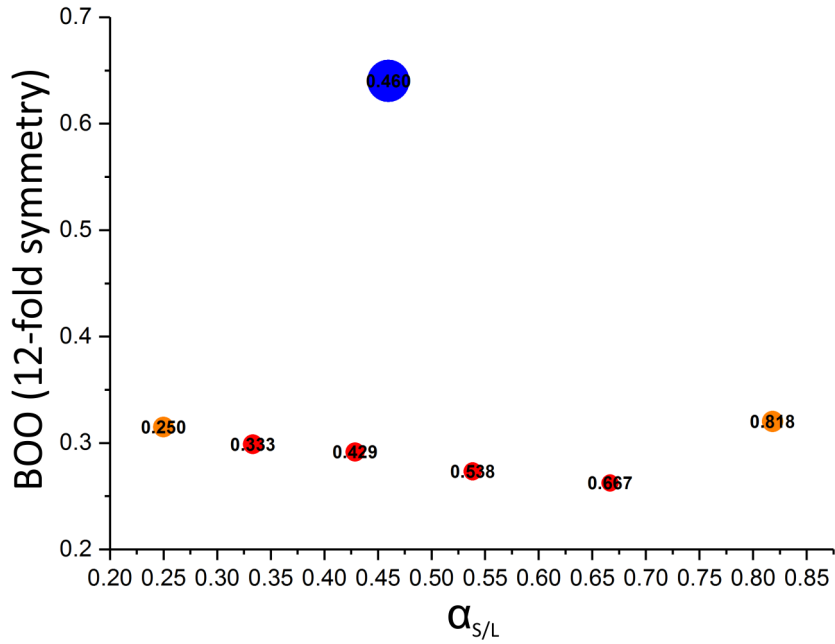


Figure 5.14: Dependence of the 12-fold BOO on the number ratio  $\alpha_{S/L}$ .

In conclusion, it was demonstrated that colloidal quasicrystals can be formed by self-assembly of binary particle systems. Thereby, it is crucial to apply distinct size and number ratios which are theoretically motivated. The theoretical predicted size and number ratios could be evidenced by compliant experimental and simulated results. Furthermore, it was shown that the electrostatic repulsion between the small particles is neglectable while the repulsion between the large particles must not be too high.

## References

- [1] Joannopoulos, J.; Johnson, S.; Winn, J.; Meade, R. *Photonic Crystals: Molding the Flow of Light*; Princeton University Press, 2011.
- [2] Mekis, A.; Chen, J. C.; Kurland, I.; Fan, S.; Villeneuve, P. R.; Joannopoulos, J. D. High Transmission through Sharp Bends in Photonic Crystal Waveguides. *Physical Review Letters* **1996**, *77*, 3787–3790, PRL.
- [3] Zoorob, M. E.; Charlton, M. D. B.; Parker, G. J.; Baumberg, J. J.; Netti, M. C. Complete photonic bandgaps in 12-fold symmetric quasicrystals. *Nature* **2000**, *404*, 740–743.
- [4] Shechtman, D.; Blech, I.; Gratias, D.; Cahn, J. W. Metallic Phase with Long-Range Orientational Order and No Translational Symmetry. *Physical Review Letters* **1984**, *53*, 1951–1953.
- [5] Levine, D.; Steinhardt, P. J. Quasicrystals: A New Class of Ordered Structures. *Physical Review Letters* **1984**, *53*, 2477–2480.
- [6] Poon, S. Electronic properties of quasicrystals an experimental review. *Advances in Physics* **1992**, *41*, 303–363.
- [7] Mayou, D. Discussion of electronic properties of quasicrystals. *Philosophical Magazine* **2008**, *88*, 2209–2215.
- [8] Zeng, X.; Ungar, G.; Liu, Y.; Percec, V.; Dulcey, A. E.; Hobbs, J. K. Supramolecular dendritic liquid quasicrystals. *Nature* **2004**, *428*, 157–160.
- [9] Fischer, S.; Exner, A.; Zielske, K.; Perlich, J.; Deloudi, S.; Steurer, W.; Lindner, P.; Foerster, S. Colloidal quasicrystals with 12-fold and 18-fold diffraction symmetry. *Proceedings of the National Academy of Sciences of the United States of America* **2011**, *108*, 1810–1814.
- [10] Zhang, J.; Bates, F. S. Dodecagonal Quasicrystalline Morphology in a Poly(styrene-*b*-isoprene-*b*-styrene-*b*-ethylene oxide) Tetrablock Terpolymer. *Journal of the American Chemical Society* **2012**, *134*, 7636–7639, PMID: 22506899.
- [11] Gillard, T. M.; Lee, S.; Bates, F. S. Dodecagonal quasicrystalline order in a diblock copolymer melt. *Proceedings of the National Academy of Sciences* **2016**, *113*, 5167–5172.
- [12] Talapin, D. V.; Shevchenko, E. V.; Bodnarchuk, M. I.; Ye, X.; Chen, J.; Murray, C. B. Quasicrystalline order in self-assembled binary nanoparticle superlattices. *Nature* **2009**, *461*, 964–967.
- [13] Bodnarchuk, M. I.; Erni, R.; Krumeich, F.; Kovalenko, M. V. Binary Superlattices from Colloidal Nanocrystals and Giant Polyoxometalate Clusters. *Nano Letters* **2013**, *13*, 1699–1705, PMID: 23488858.

- [14] Yang, Z.; Wei, J.; Bonville, P.; Pileni, M.-P. Beyond Entropy: Magnetic Forces Induce Formation of Quasicrystalline Structure in Binary Nanocrystal Superlattices. *Journal of the American Chemical Society* **2015**, *137*, 4487–4493, PMID: 25785302.
- [15] Ye, X.; Chen, J.; Irrgang, M. E.; Engel, M.; Dong, A.; Glotzer, S. C.; Murray, C. B. Quasicrystalline nanocrystal superlattice with partial matching rules. *Nature Materials* **2017**, *16*, 214–219.
- [16] Engel, M.; Damasceno, P. F.; Phillips, C. L.; Glotzer, S. C. Computational self-assembly of a one-component icosahedral quasicrystal. *Nature Materials* **2015**, *14*, 109–116.
- [17] Damasceno, P. F.; Glotzer, S. C.; Engel, M. Non-close-packed three-dimensional quasicrystals. *Journal of Physics: Condensed Matter* **2017**, *29*, 234005.
- [18] Schoberth, H. G.; Emmerich, H.; Holzinger, M.; Dulle, M.; Forster, S.; Gruhn, T. Molecular dynamics study of colloidal quasicrystals. *Soft Matter* **2016**, *12*, 7644–7654.
- [19] Dotera, T.; Oshiro, T.; Zihlerl, P. Mosaic two-lengthscale quasicrystals. *Nature* **2014**, *506*, 208–211.
- [20] Frank, F. C.; Kasper, J. S. Complex alloy structures regarded as sphere packings. II. Analysis and classification of representative structures. *Acta Crystallographica* **1959**, *12*, 483–499.
- [21] Retsch, M.; Zhou, Z.; Rivera, S.; Kappl, M.; Zhao, X. S.; Jonas, U.; Li, Q. Fabrication of Large-Area, Transferable Colloidal Monolayers Utilizing Self-Assembly at the Air/Water Interface. *Macromolecular Chemistry and Physics* **2009**, *210*, 230–241.
- [22] Vogel, N.; Viguerie, L. d.; Jonas, U.; Weiss, C. K.; Landfester, K. Wafer-Scale Fabrication of Ordered Binary Colloidal Monolayers with Adjustable Stoichiometries. *Advanced Functional Materials* **2011**, *21*.
- [23] Widom, M. Bethe ansatz solution of the square-triangle random tiling model. *Physical Review Letters* **1993**, *70*, 2094–2097.
- [24] Steinhardt, P. J.; Nelson, D. R.; Ronchetti, M. Bond-orientational order in liquids and glasses. *Phys. Rev. B* **1983**, *28*, 784–805.

## 6 Preparation of quasicrystals by soft lithography

Whereas both chapter 4 and 5 relied on colloidal self-assembly, an even broader variety of structures can be realized by soft lithography. Although sophisticated methods have been developed, self-assembly still features limitations in domain sizes and inherently contains defects. By contrast, lithography creates perfect single crystalline structures which are suitable for detailed investigation of relationships between structure and optical properties.

The physics of photonic crystals are of particular interest of current research as they control various optical phenomena. An exceptional characteristic of photonic crystals is the presence of a photonic band gap (PBG), which is the optical analogue of an electronic band gap in semiconductors. Photonic materials typically feature structures with periodically alternating dielectric constants. Photons in these structures are subject to multiple scattering so that light transport is prevented. A complete PBG, therefore, characterizes a range of wavelengths, for which light does not exist within the structure of the crystal. Notwithstanding, the presence of a defect in the crystal structure can lead to a localization of light. This means that a point defect can act as microcavity, a line defect as waveguide or a planar defect as mirror. Accordingly, the major application of photonic crystals is to control light. In recent years, light has become favored in the optoelectronics sector. Photonic crystals in optical fibers have some important advantages over e. g., electrons in metal wires, as light travels at very high speeds and it can transport significantly larger amounts of information per time.<sup>[1-3]</sup>

In this respect it is important to note that photonic quasicrystals can provide similar functionalities concerning optical interference phenomena. Quasicrystals can be described as an intermediate class besides periodic and amorphous structures. They lack any translational symmetry, but feature long-range orientational order, which is the reason for their sharp diffraction patterns. By contrast to periodic systems, photonic quasicrystals provide a higher structural complexity, which gives rise to optical effects, that cannot be realized with periodic structures. The physical properties of quasicrystals have been investigated with respect to e. g., the localization of plasmon modes<sup>[4]</sup> and enhanced optical transmission<sup>[5]</sup>. But they have also been applied as optical lenses<sup>[6]</sup>, in lasers<sup>[7]</sup> and in surface enhance Raman spectroscopy (SERS)<sup>[8]</sup>. Another appealing aspect of photonic quasicrystals is the existence of a (complete) PBG.

From a theoretical point of view, a PBG can be described by the solutions of Maxwell's equations.

$$\{\nabla \times \frac{1}{\epsilon(r)} \nabla \times\} H(r) = \frac{\omega^2}{c^2} H(r) \quad (6.1)$$

where  $H(r)$  is the magnetic field of a photon,  $\omega$  is the frequency,  $c$  is the speed of light

and  $\epsilon(r)$  is the dielectric function. Thereby, the solutions are completely defined by the strength and symmetry properties of  $\epsilon(r)$ . If we consider a periodic photonic crystal, there exists for each solution a wavevector  $k$  and a band index  $n$ . The collection of all allowed wavevectors describes the so-called Brillouin zone. In other words, for periodic structures the photonic band structure is defined by the dispersion relations in the Brillouin zone. As quasicrystals are an individual group of materials, they are not governed by the stringent regulations of periodicity derived by classical crystallography. In periodic crystals only two-, three-, four- and six-fold rotational symmetry is allowed. By contrast, quasicrystals possess arbitrary rotational symmetry, which can be even higher than six. This makes them aperiodic and a strict Brillouin zone cannot be defined. Rather, an effective Brillouin zone, the pseudo-Jones zone, is constructed by the basic set of reciprocal vectors of the quasicrystalline structure.

In order to determine a PBG, the overlaps of spectral gaps at the Brillouin zone boundaries have to be considered. Due to the restricted symmetries in periodic crystals their Brillouin zone is typical of anisotropic shape. By contrast, a consequence of the higher symmetries in quasicrystalline structures is a more circular Brillouin zone, so that also a PBG becomes more isotropic. Moreover, complete band gaps become available as the undulations of the frequency bands are smaller. A trade-off though is the scattering power of quasicrystals, which weakens with increasing symmetry. In conclusion, this makes quasicrystals inferior to crystals for materials with low dielectric contrast. As under these conditions quasicrystals possess larger PBG, they are particularly suitable as a candidate for applications in e. g. optical fibers, where a high optical transmission is required.

So far, much effort has been put into the investigation of periodic photonic crystals. Unfortunately, for these materials it was crucial to have large dielectric contrasts, as photonic crystals with lower contrast prevent opening a PBG.<sup>[9,10]</sup> Zoorob *et al.* showed for the first time that also for materials with low dielectric contrast a complete PBG can be realized using quasicrystalline structures.<sup>[11]</sup> They fabricated two-dimensional photonic quasicrystals with feature sizes in the submicron range by etching air holes into silicon nitride and glass.

One of the major drawbacks of their work is the dependence on a fabrication technology, that requires expensive equipment and production is limited to small scale devices. In this work, it was taken the advantage of Maxwell's equations that they are not based on fundamental length scales. If the dependence of the dielectric function on the wavelength is ignored, physical properties can be deduced for various dimensions of the feature size. Therefore, it is practical to fabricate photonic quasicrystals using readily available methods with high throughput and low costs. Consequently, this work is based on soft lithography to fabricate two-dimensional quasicrystalline structures with easily accessible feature sizes in the micron range. These structures will be characterized and the results obtained can eventually be used to extrapolate the behavior of the same structures at considerably smaller length scales.

## 6.1 Preparation of micropatterns by soft lithography

This work presents a simple and straightforward method for the fabrication of arbitrary two-dimensional quasicrystalline structures on the microscale and their characterization with respect to photonic properties. In principle, the method is based on soft lithography as part of the concept of rapid prototyping developed by Whitesides *et al.*<sup>[12,13]</sup>

The procedure involves the preparation of a template via photo lithography, which is replicated in poly(dimethylsiloxane) (PDMS) via soft lithography. Finally, the structure is transferred to a thin metal layer to investigate structure-property relationships by attenuated total reflection Fourier transform infrared spectroscopy (ATR-FTIR) measurements. For the preparation of the template, a photo resist was spin-coated onto a silicon wafer (Figure 6.1 a). A photo mask enabled selective exposure of the photo resist with UV light (Figure 6.1 b). Exposed areas of the photo resist are cross-linked, while the remaining non-exposed parts can be removed by dissolving in an appropriate solvent (Figure 6.1 c).

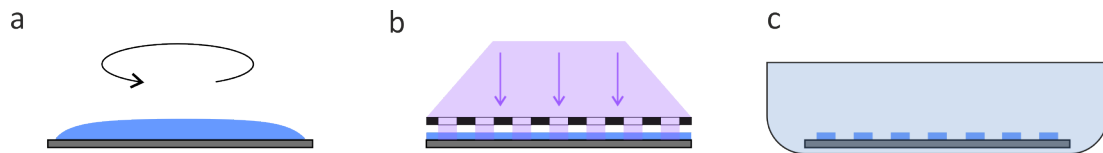


Figure 6.1: Schematic illustration of the preparation of a template by photo lithography. (a) For this purpose, a photo resist is spin-coated onto a silicon wafer and (b) selectively exposed to UV light through a photo mask comprising the desired structure. (c) The exposure induces a cross-linking in the resist, so that unexposed areas can be dissolved in an appropriate solvent.

Thereby, the photo mask features the quasicrystalline pattern. For the major part of this work, a quasicrystalline structure with twelve-fold symmetry generated by the deflation method was chosen (Figure 6.2).

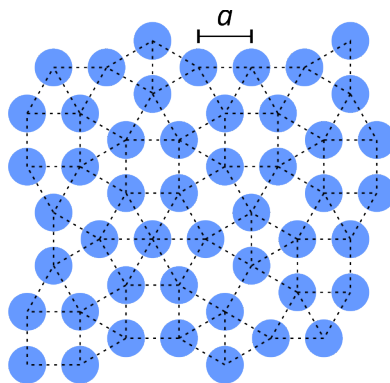


Figure 6.2: Section of a quasicrystalline structure with twelve-fold symmetry generated by the deflation method.

But also quasicrystals with other, arbitrary symmetry, e. g., five- and eighteen-fold, were generated using the generalized dual method (GDM) (Figure 6.3). The characteristic measure of all generated structures is given by the size  $a$ , which represents the edge length of the tiles. This edge length  $a$  is comparable to the lattice constant of periodic structures. It influences the wavelength range, within which interaction between the structure and light takes place.

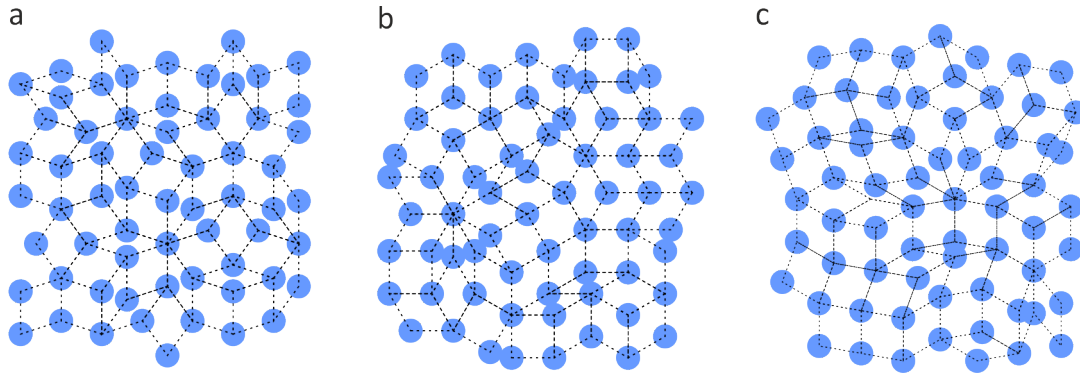


Figure 6.3: Sections of quasicrystalline structures generated by the GDM showing (a) five-fold, (b) twelve-fold and (c) eighteen-fold symmetry.

The result of this first step is a template that comprises a relief of the quasicrystalline structure from the photo mask (Figure 6.4 a) and can be used for replication via soft lithography. For the preparation of PDMS-based structures, a mixture of PDMS prepolymer and curing agent is cured on the template (Figure 6.4 b). This yields a negative relief structure in PDMS (Figure 6.4 c).

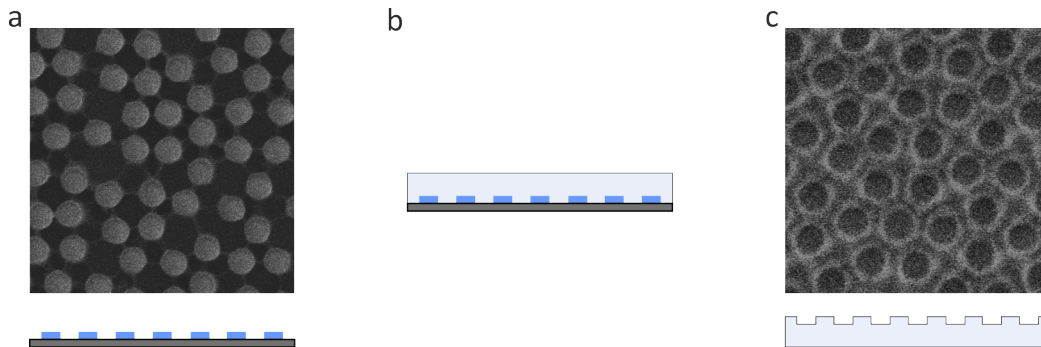


Figure 6.4: Schematic illustration of the replication of two-dimensional quasicrystalline structures via soft lithography. (a) The template is a wafer with photo resist that features a relief structure. (b) Liquid PDMS prepolymer is cured on the template. (c) The relief structure of the template is thereby replicated in PDMS.

In order to characterize the prepared structure by ATR-FTIR, the quasicrystalline pattern is a second time replicated in a thin metal layer of gold. For this purpose, gold and titanium are successively vapor deposited to generate a conformal coating on the PDMS (Figure 6.5 a). In this respect, titanium has the role of a linking layer. During plasma treatment, on the surface of mere PDMS and titanium, silanol and titanol groups are

formed, respectively (Figure 6.5 b). When these two surfaces are contacted under the influence of a slight pressure and moderate heat, the silanol and titanol groups bond covalently. Consequently, the gold layer detaches from the PDMS relief and is transferred onto a flat PDMS substrate (Figure 6.5 c).

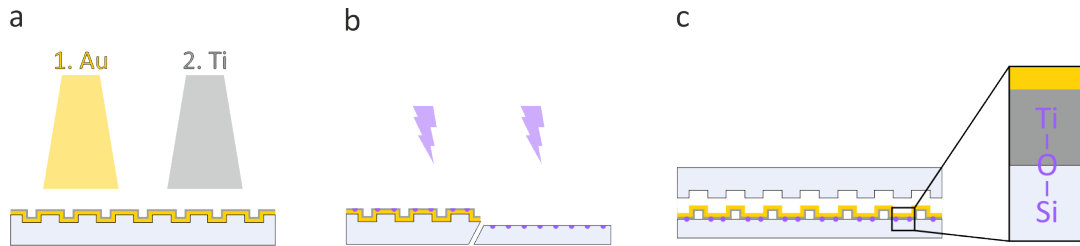


Figure 6.5: Schematic illustration of the transfer of two-dimensional quasicrystalline structures from PDMS to gold films. (a) Gold and titanium are successively vapor deposited onto the structured PDMS. (b) In order to transfer the metal structure onto a flat PDMS substrate, the surfaces of the titanium layer on the structured PDMS and of the flat PDMS substrate are activated in an air plasma. (c) Under slight pressure and moderate heat, covalent bonds are formed between the titanium layer and the PDMS substrate. Thereby, the patterned gold film is transferred.

The most striking advantage of lithography as a source for the generation of microstructures is the overall control of the structure. Lithography features an exact replication of the desired structure without any defects, which are inherent to other methods, e. g. self-assembly. Whereas lithography methods such as electron or focused ion beam lithography are comparable expensive, rely on special equipment and feature a low throughput, soft lithography as applied in this work is a very convenient technique. Structures with feature sizes down to  $1\ \mu\text{m}$  can be produced in cm-scale within a few hours.

## 6.2 Replication of micropatterns to thin metal layers

A photograph of PDMS comprising a quasicrystalline structure with twelve-fold symmetry is shown in Figure 6.6 a. The laser diffraction through these structures features a perfect scattering image with multiple diffraction orders (Figure 6.6 b).

The perfection of the structure is also demonstrated by the SEM images of the patterned PDMS (Figure 6.7). The quasicrystalline structure is represented by cylindrical air holes in a PDMS matrix. It can be seen that the replication shows a defect-free single quasicrystalline arrangement of the cylinders.

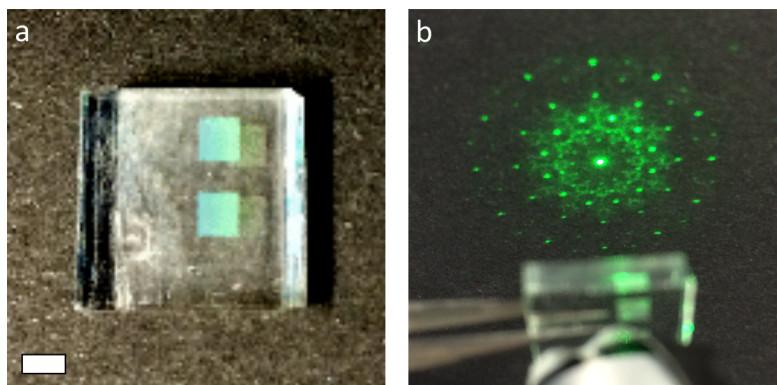


Figure 6.6: (a) Photograph and (b) laser diffraction (532 nm) of a quasicrystalline structure with twelve-fold symmetry in PDMS. Scale bar is 2 mm.

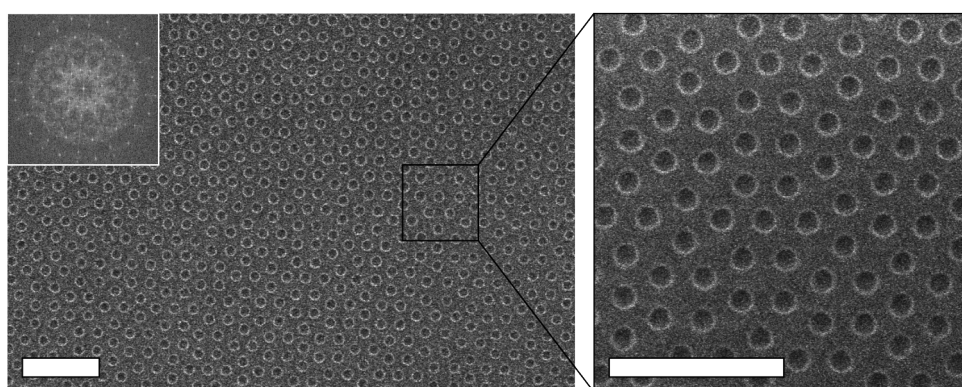


Figure 6.7: SEM images of the quasicrystalline structure with twelve-fold symmetry in PDMS, with the inset showing the FFT. Scale bars are  $10 \mu\text{m}$ .

The transfer of this structure to a thin gold layer in the final step requires vapor deposition of the metal. The transferred metal films were investigated by scanning electron microscopy (SEM) and atomic force microscopy (AFM) (Figure 6.8). In dependence on the layer thickness either a hole mask or a conformal replication of the air cylinders were obtained. In our case for a layer thickness of 50 nm, hole masks (Figure 6.8 a/b) were formed, whereas a layer thickness of 100 nm yielded a complete, conformal replication of gold cylinders (Figure 6.8 c/d).

### 6.3 Characterization of optical properties

For the subsequent characterization by ATR-FTIR, the gold films comprising the gold cylinders were chosen, as these films proved to be more stable and reproducible during transfer. Based on the PDMS structures, gold films with different characteristic lattice sizes  $a$  were prepared. Thereby, the cylinder diameter was kept constant at  $1.25 \mu\text{m}$ , while the center-to-center distance was gradually increased from  $2 \mu\text{m} - 3 \mu\text{m}$  (Figure 6.9).

ATR-FTIR was used to characterize the optical properties of the gold films in dependence

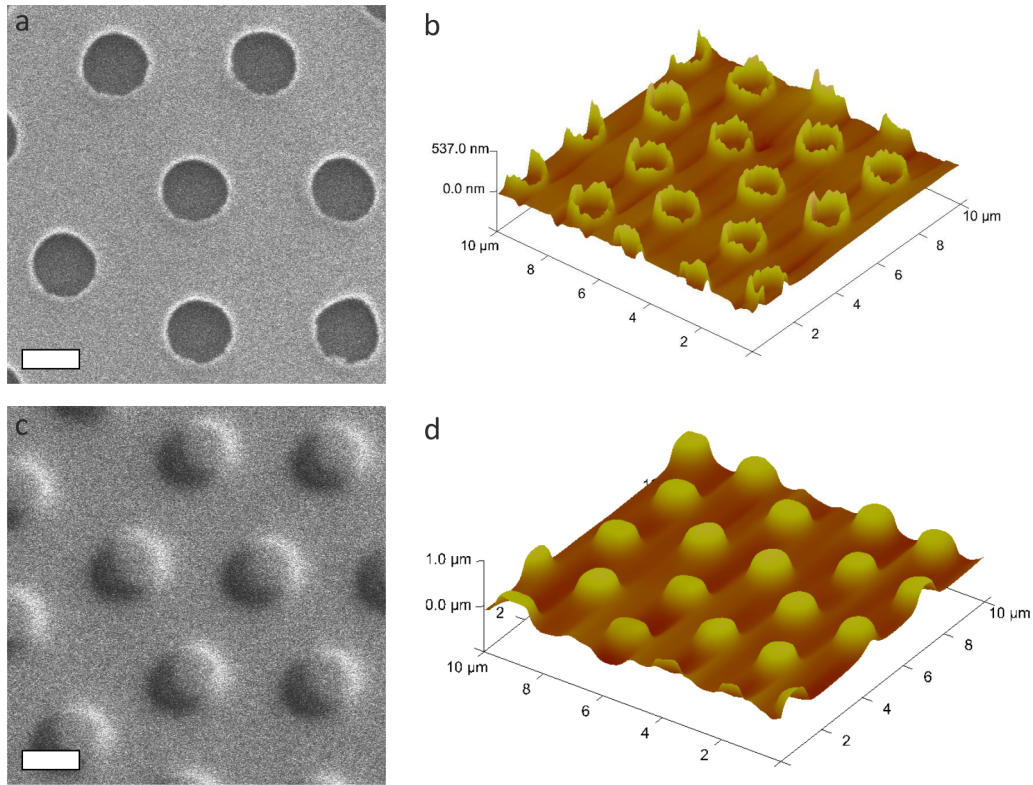


Figure 6.8: SEM and AFM images of the quasicrystalline structure with twelve-fold symmetry in a gold layer with a thickness of (a)/(b) 50 nm and (c)/(d) 100 nm. Scale bars are 1  $\mu\text{m}$ .

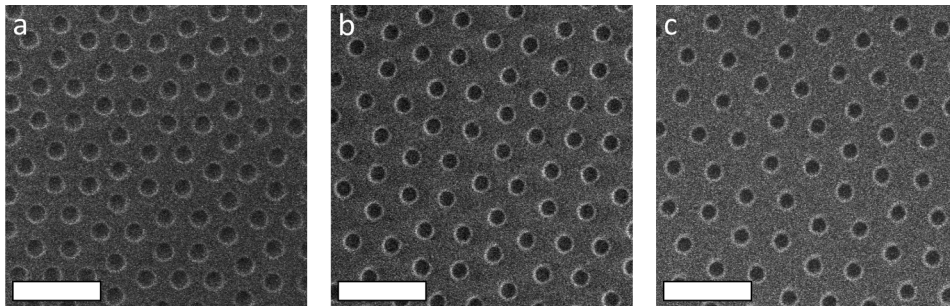


Figure 6.9: SEM images of quasicrystalline structures with characteristic lattice size of (a)  $a = 2.50 \mu\text{m}$ , (b)  $a = 2.75 \mu\text{m}$  and (c)  $a = 3.00 \mu\text{m}$ .

on their lattice size. In this method, the infrared (IR) light is coupled into the sample in form of an evanescent wave. If the sample features (partial) photonic band gaps, light cannot propagate through the structure within a certain wavelength range. As a result, the transmission is reduced. Figure 6.10 depicts the transmittance spectra of the three investigated samples as solid lines and the corresponding fits as dashed lines. Furthermore, plain gold on PDMS is shown as reference spectrum.

It can be seen that the transmittance shows a broad minimum between 7  $\mu\text{m}$  and 10  $\mu\text{m}$  for all samples. This alone does not qualify a photonic bad gap, but the distinct minima

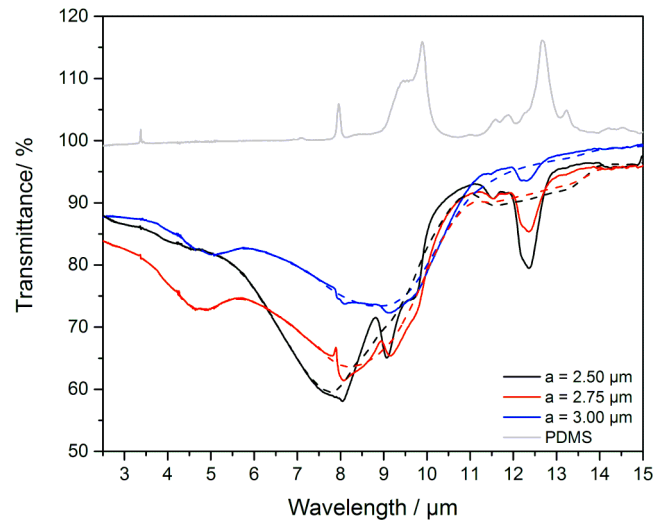


Figure 6.10: Transmittance spectra of gold cylinders with dodecagonal symmetry measured with ATR-FTIR. The original transmittance spectra (solid lines) are fitted (dashed lines) in order to determine the transmittance minimum.

shift in dependence on the center-to-center distance  $a$  of the samples, which may indicate a band gap. Besides, the transmittance minimum there are several other features present in the transmittance spectra. These features largely originate from the PDMS substrate as the penetration depth of the evanescent wave typically exceeds the layer thickness of the gold (100 nm). The reference spectrum of PDMS covered with a plain gold layer confirms this assumption (Figure 6.10, grey solid line). It can be seen that the transmittance only approaches a minimum of 60%. For a stronger reduction of the transmittance both the sample geometry and the materials have to be further optimized.

If the wavelengths of the transmittance minima are plotted against the characteristic lattice size  $a$  a linear dependence can be observed (Figure 6.11). The wavelength of the minimum approximately amounts to  $\lambda = a/0.33$ .

The systematic occurrence of transmittance minima suggests the existence of a photonic band gap. However, a complete characterization requires probing the transmittance angle-dependent corresponding to a reciprocal lattice. Furthermore, the results have to be compared to complex band structure calculations for a confirmation of the band gap.

#### 6.4 Simulation of waveguiding properties

Simulations were accomplished to further investigate and verify the presence of (partial) photonic band gaps for the prepared gold films. For this purpose, the quasicrystalline structure from Figure 6.2 was modified by removal of cylinders along a line with a  $90^\circ$  bending. In this configuration, the photonic quasicrystal can work as a waveguide, which

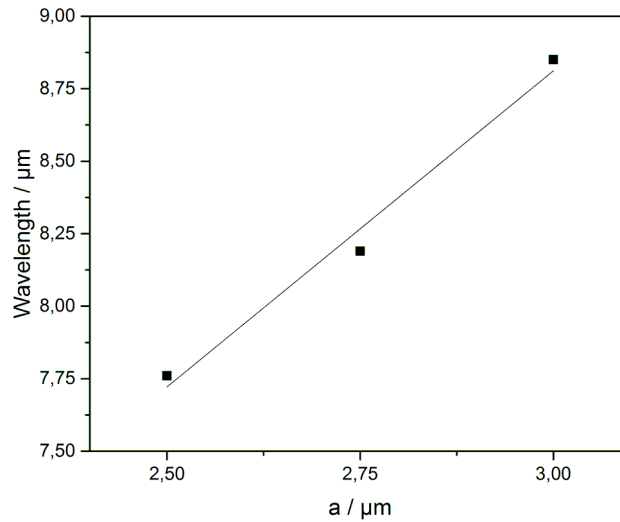


Figure 6.11: Wavelength of the transmittance minima as a function of the characteristic lattice size  $a$ .

concentrates the power of propagating light within the defect structure. The interaction of light with the quasicrystalline structure comprising a line defect was simulated with COMSOL (Figure 6.12).

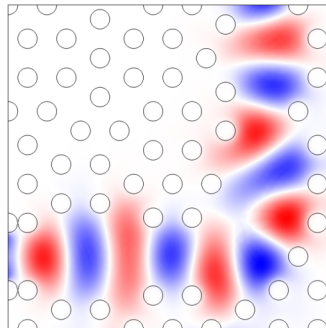


Figure 6.12: COMSOL simulation for the propagation of light within a line defect of a dodecagonal quasicrystalline structure. The wave is coupled in at the left side and propagates through the bending defect before leaving the structure at the top. Simulation parameters:  $\lambda = a/0.3$ , materials = gold (medium), air (circles).

The depicted section shows the simulation for a wave with  $\lambda = a/0.35$  and a gold film (medium = gold, circles = air). Red and blue colors denote positive and negative vertical displacement of the wave, respectively. It can be seen that the incoming wave at the left side is confined within the line defect. The wave follows the  $90^\circ$  bending and leaves the structure at the top. This behavior can be observed for wavelengths  $\lambda$  in the range of  $\sim a/0.25 - a/0.35$ . The wave hardly diffuses into the quasicrystalline structure, but decays exponentially off the defect line.

The results of the simulation support the assumption that the quasicrystalline structure possesses a (partial) photonic band gap. Furthermore, the wavelength range is also in accordance with the experimental findings where the partial photonic band gaps are assumed at wavelengths  $\lambda \approx a/0.3$ .

In conclusion, it was shown that quasicrystalline structures can be fabricated by soft lithography with feature sizes down to  $1\ \mu\text{m}$ . The structures show perfect diffraction patterns for a dodecagonal symmetry. Measurements of the optical properties revealed that the transmission significantly decreased for a certain wavelength range which is dependent on the lattice constant. Simulations verified that light with an appropriate wavelength is confined within a defect structure in the quasicrystal. Summarizing experiments and simulations, this suggests the existence of a (partial) photonic band gap.

## References

- [1] Yablonovitch, E. Inhibited Spontaneous Emission in Solid-State Physics and Electronics. *Physical Review Letters* **1987**, *58*, 2059–2062.
- [2] Joannopoulos, J. D.; Villeneuve, P. R.; Fan, S. Photonic crystals: putting a new twist on light. *Nature* **1997**, *386*, 143–149, 10.1038/386143a0.
- [3] Joannopoulos, J.; Johnson, S.; Winn, J.; Meade, R. *Photonic Crystals: Molding the Flow of Light*; Princeton University Press, 2011.
- [4] Dallapiccola, R.; Gopinath, A.; Stellacci, F.; Negro, L. D. Quasi-periodic distribution of plasmon modes in two-dimensional Fibonacci arrays of metal nanoparticles. *Optics Express* **2008**, *16*, 5544–5555.
- [5] Przybilla, F.; Genet, C.; Ebbesen, T. W. Enhanced transmission through Penrose sub-wavelength hole arrays. *Applied Physics Letters* **2006**, *89*, 121115.
- [6] Huang, F. M.; Kao, T. S.; Fedotov, V. A.; Chen, Y.; Zheludev, N. I. Nanohole Array as a Lens. *Nano Letters* **2008**, *8*, 2469–2472, PMID: 18572971.
- [7] Mahler, L.; Tredicucci, A.; Beltram, F.; Walther, C.; Faist, J.; Beere, H. E.; Ritchie, D. A.; Wiersma, D. S. Quasi-periodic distributed feedback laser. *Nature Photonics* **2010**, *4*, 165–169, 10.1038/nphoton.2009.285.
- [8] Gopinath, A.; Boriskina, S. V.; Reinhard, B. M.; Negro, L. D. Deterministic aperiodic arrays of metal nanoparticles for surface-enhanced Raman scattering (SERS). *Optics Express* **2009**, *17*, 3741–3753.
- [9] Cassagne, D.; Jouanin, C.; Bertho, D. Hexagonal photonic-band-gap structures. *Physical Review B* **1996**, *53*, 7134–7142.
- [10] Barra, A.; Cassagne, D.; Jouanin, C. Existence of two-dimensional absolute photonic band gaps in the visible. *Applied Physics Letters* **1998**, *72*, 627–629.
- [11] Zoorob, M. E.; Charlton, M. D. B.; Parker, G. J.; Baumberg, J. J.; Netti, M. C. Complete photonic bandgaps in 12-fold symmetric quasicrystals. *Nature* **2000**, *404*, 740–743.
- [12] Xia, Y.; Whitesides, G. M. Soft Lithography. *Angewandte Chemie International Edition* **1998**, *37*, 550–575.
- [13] Xia, Y.; Whitesides, G. Soft lithography. *Annual Review of Materials Science* **1998**, *28*, 153–184.



## 7 Conclusion and future perspectives

In this thesis ordered structures with other than hexagonal symmetry were prepared by self-assembly and soft lithography. Thereby the following major results were achieved:

1. Preparation of ordered particle arrays with all two- dimensional Bravais lattices by self-assembly of colloidal particles.
2. Preparation of colloidal quasicrystals with dodecagonal symmetry by self-assembly of binary particle mixtures.
3. Fabrication of quasirystalline micropatterns by soft lithography with arbitrary symmetry.

**The self-assembly of colloidal particles into ordered particle arrays with all two- dimensional Bravais lattices** was successfully demonstrated. The presented method combines the convenience of an established interfacial self-assembly technique with the broadened availability of new structures. Compared to existing routes to non-close-packed colloidal crystals, this approach is superior with respect to its simplicity and its variability. Polymer colloids consisting of poly(*n-butyl-co-methyl methacrylate*) were synthesized by emulsifier-free emulsion polymerization. These particles were self-assembled at the water/air interface. Whereas an uptake on hydrophilic substrates yielded standard hexagonal close-packed particle arrangements, the collection on hydrophobic substrates induced a one-dimensional stretching of the colloidal monolayer along the uptake direction. It was revealed that a thermal fixation of the particles on the substrate was crucial for the preservation of the stretched non-close-packed structure. In this work, the fixation was accomplished either via the particles or the substrate. Without this step, capillary forces induced a re-contraction of the particle arrangement upon drying. Additionally, it was shown that the magnitude of stretching is only dependent on the contact angle of the hydrophobic substrate. Hence, the final symmetry of the structure is fully determined by two experimental parameters. This enables the preparation of two-dimensional colloidal crystals with all Bravais lattices.

**Self-assembled colloidal quasicrystals with dodecagonal symmetry** obtained from a binary particle system showed a good order. For this purpose monodisperse polystyrene particles with distinct sizes were prepared by emulsifier-free emulsion polymerization. A linear dependence of the particle diameter on the reaction temperature, the co-monomer concentration and the salt concentration was revealed. Thereby, the latter parameter proved to be unsuitable as the monodispersity was significantly reduced in the presence of higher salt amounts. Based on theoretical considerations, the self-assembly of different particles with a varying size and number ratio were investigated. It was shown that only the quasicrystalline structure with the higher density of large particles could be

formed, while the low density quasicrystalline structure was experimentally not stable. In the former case the size and number ratio have to match  $\gamma_{S/L} = 0.42$  and  $\alpha_{S/L} = 0.46$ , respectively. The formed quasicrystalline phase featured a twelve-fold symmetry, which was verified by additional calculations of the bond orientational order. Furthermore, the behavior of binary particle systems was studied in molecular dynamics simulations. Thereby, besides the size and number ratio, also the influence of the electrostatic repulsion between the particles was analyzed. Whereas the repulsion between the small particles has only minor effects on the formed structure, a high repulsion between the large particles interferes with the formation of ordered structures. The simulations with a varying size and number ratio were in good accordance with the experimental results. It was revealed that the adjustment of these two parameters is crucial for the formation of a colloidal quasicrystal.

**The fabrication of quasicrystalline microstructures by soft lithography** allowed the characterization of optical properties. It was demonstrated that quasicrystalline structures with arbitrary symmetry and varying lattice constants can be molded in polydimethylsiloxane. These quasicrystals feature a defect-free structure with dimensions in the cm range. A further advantage is the possibility to transfer these structures to other moldable materials and thin metal layers. It was shown that a thin gold film comprising the quasicrystalline structure can be used to characterize optical properties. The measurements revealed a transmittance minimum for all investigated structures in dependence on their lattice size. This emphasizes that quasicrystalline assemblies are a promising technology for controlling the transport of electromagnetic waves.

The results of this thesis regarding the preparation of ordered structures with other than hexagonal symmetry have a broad implication for future work in this field of study.

The presented method for the formation of ordered particle arrangements with all two-dimensional Bravais lattices can be used for arbitrary particles in the nano- to micrometer range which self-assemble at interfaces. This work identified the requirement for immobilization of the particles as a crucial step. In this work thermal fixation was used to increase the adhesive contact area of the particles on the substrate. For future works, other strategies based on e. g. covalent or non-covalent binding are of interest. Furthermore, the prepared non-close-packed structures can be implemented to colloidal lithography. The presented results focused mainly on two-dimensional particle assembly, but as a short outlook, also three dimensional non-close-packed structures are possible to realize. If a substrate with a non-close-packed structure is reused as substrate for a second deposition, it was observed that the particle positions in the second layer are dictated by the previous one. Therefore, the non-close-packed structures can be applied as directing templates.

The self-assembled quasicrystalline structures were limited to small domain sizes. Therefore future work should involve the optimization of the self-assembly process in order to increase the size of single quasicrystalline domains. In the next step, the self-assembled structures can then be used for characterization of optical properties. This will enable a deeper insight into the structure-property relationships of colloidal quasicrystals. Moreover, the self-assembly of colloids consisting of other organic and inorganic materials can be investigated. Deducing from the molecular dynamics simulations the formation of colloidal quasicrystals is not restricted to a certain kind of particle type as long as the requirements for size and number ratio are fulfilled.

The fabrication of quasicrystalline micropatterns by soft lithography yielded reproducibly high quality structures in poly(dimethylsiloxane). Future work should attend the question if soft lithography is still possible when the lattice constants are reduced to the nanometer range. For application in the field of telecommunication it is desirable to achieve band gaps at around  $1.5 \mu\text{m}$ . Moreover, new materials will be investigated in order to enhance the dielectric contrast and favor complete photonic band gaps. Additionally, the dependence of photonic band gaps on the degree of symmetry can be investigated in more detail. In principle, complete photonic band gaps are more likely for higher symmetries.

The presented ideas show that there is still a number of challenges for future work to solve. Nevertheless, the results of this work extend the possibilities to produce colloidal structures and also show promising results for future applications.



## 8 Experimental Section

### 8.1 Materials

For the synthesis of polymers and polymer particles styrene ( $\geq 99\%$ , Aldrich), acrylic acid ( $\geq 99\%$ , Aldrich), azobisisobutyronitrile (AIBN) ( $98\%$ , Aldrich), potassium peroxydisulfate (KPS) ( $\geq 99\%$ , Aldrich), and toluene ( $\geq 99\%$ , VWR) were used as received. *n*-butyl acrylate (nBA) ( $\geq 99\%$ , Aldrich) was purified by column chromatography over an aluminum oxide powder (activated, basic, Brockmann I, Sigma-Aldrich). Water was taken from a Milli-Q system (Millipore) with a resistivity of  $18\text{ M}\Omega\text{cm}$  for synthesis and purification steps.

For the preparation of colloidal monolayers Hellmanex  $\text{\textcircled{R}}$  III (Aldrich), ethanol ( $> 99.8\%$ , VWR), *N*-trimethoxysilylpropyl-*N,N,N*-tri-methylammonium chloride ( $50\%$  in methanol, ABCR), ammonia ( $28\%$ , VWR), and sodium dodecyl sulfate (SDS) ( $98\%$ , VWR) were also used as received. As glass slides, standard microscopy slides (Menzel, Braunschweig, Germany) were used.

The fabrication of micropatterns was accomplished with EPON $\text{\textcircled{R}}$ SU-8 2000.5 ( $14.3\%$  in  $\gamma$ -butyrolactone, microchem), mrDEV 600 (microchem), and poly(dimethylsiloxane) (PDMS) base polymer and curing agent (Sylgard $\text{\textcircled{R}}$ 184, Dow Corning) without further purification.

### 8.2 Synthesis

#### 8.2.1 Synthesis of PS colloids

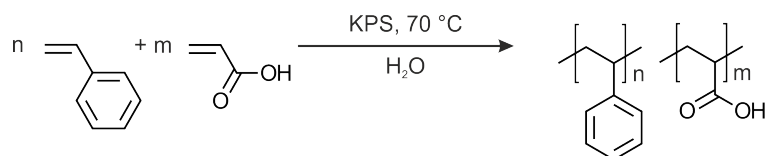


Figure 8.1: Emulsion polymerization of styrene and acrylic acid.

Monodisperse polystyrene (PS) particles with acrylic acid as co-monomer were prepared by emulsifier-free emulsion polymerization (Figure 8.1). The synthesis procedure was adapted from Ottewill *et al.*<sup>[1]</sup> The polymerizations were carried out in 500 mL three necked flasks under a slight argon flow. The flasks were charged with water and styrene and the mixture was heated up to  $70\text{ }^\circ\text{C}$  under vigorous stirring. After equilibration for 20 min, acrylic acid was added and the mixture was equilibrated for a further 10 min. KPS was dissolved in water prior to addition. The polymerization was carried out over night and quenched by exposure to ambient atmosphere. A typical solid content of the raw product was  $7\text{ wt}\%$ . For purification, the particles were centrifuged and washed with

water three times. Particles dispersed in 5 mL water had a shelf-life of more than one year. The particle size was determined by scanning electron microscopy (SEM) measurements.

### 8.2.2 Synthesis of PMMA particles

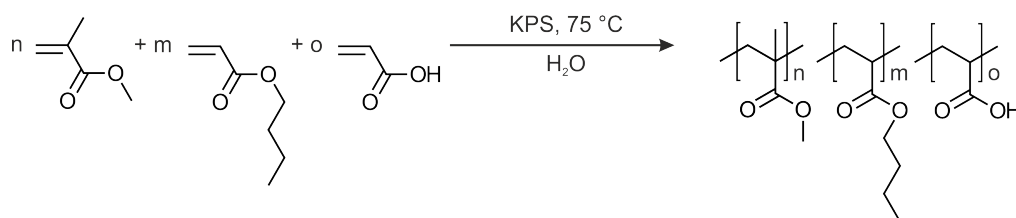


Figure 8.2: Emulsion polymerization of methyl methacrylate, *n*-butyl acrylate and acrylic acid.

Monodisperse poly(*n*-butyl acrylate-co-methyl methacrylate) (P(*n*BA-co-MMA)) particles were prepared by emulsifier-free emulsion polymerization (Figure 8.2). 450 mL milliQ water were mixed with 35 mL methyl methacrylate (MMA) and 15 mL *n*BA, respectively. The mixture was equilibrated at 75 °C under a slight argon flow for 15 min. Subsequently, 2 mL of acrylic acid were added to the mixture followed by a further equilibration step for 5 min. The polymerization was started by a rapid injection of 150 mg KPS dissolved in 5 mL milliQ water. The reaction was carried out overnight. The polymerization was quenched by exposure to air. Residual educts were removed by dialysis against water for five days, changing water twice a day. Particles with a mean diameter of  $434 \pm 12$  nm and with a glass transition temperature of 61 °C were obtained. The particles were prepared by F. A. Nutz (Physical Chemistry I – Polymer Systems, University of Bayreuth).

### 8.2.3 Synthesis of polymers for hydrophobic substrates

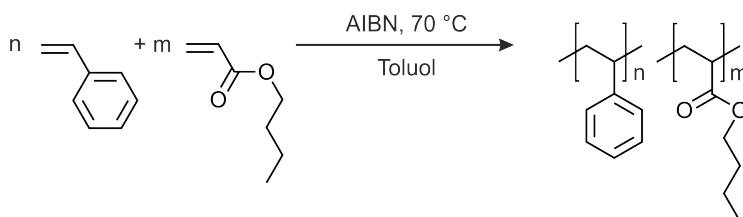


Figure 8.3: Free radical polymerization of styrene and *n*-butyl acrylate.

Hydrophobic polymers used as substrate coating were prepared by free radical polymerization (Figure 8.3). In order to adjust the glass transition temperature ( $T_g$ ) of the resulting polymer, styrene was co-polymerized with *n*BA as described by Fernandez-Garcia *et al.*<sup>[2]</sup> The polymerization was carried out in an argon atmosphere. In a 100 mL Schlenk flask 150 mg AIBN was dissolved in 40 mL toluene. Then, 7 mL styrene and 3 mL *n*BA were added and the reaction mixture was heated to 70 °C. The polymerization was

quenched after 3 h by cooling in an ice bath. Subsequently, the polymer was precipitated in a methanol/dry ice mixture. The white solid was dried at room temperature under reduced pressure. The resulting polymer showed a  $T_g = 54^\circ\text{C}$ .

### 8.3 Sample Preparation

#### 8.3.1 Preparation of hydrophobic substrates

Hydrophobic substrates were prepared by spin-coating glass slides with either PS, poly(*n*-butyl acrylate-co-styrene) (P(nBA-co-S)) or poly(methyl methacrylate) (PMMA). Solutions in toluene with 10–20 wt% polymer were spin-coated at 3000 rpm for 3 min and subsequent annealing at  $200^\circ\text{C}$  for 5 min. SU-8 substrates were obtained by spin-coating SU-8 2050 at 3000 rpm for 30 s. After a soft bake at  $65^\circ\text{C}$  for 1 min and at  $95^\circ\text{C}$  for 7 min, the substrate was exposed to UV light for  $2 \times 4\text{ s}$ . A post exposure bake was carried out at  $65^\circ\text{C}$  for 1 min and at  $95^\circ\text{C}$  for 6 min. Commercially available polytetrafluoroethylene (PTFE) films with a thickness of 1 mm were cut into  $1 \times 1\text{ cm}^2$  pieces and used after cleaning with ethanol.

#### 8.3.2 Preparation of two-dimensional colloidal crystals

In this thesis, two-dimensional colloidal crystals are prepared according to the method reported by Retsch *et al.* (Figure 8.4).<sup>[3]</sup> This procedure can be divided into two major steps. The functionalization of glass slides, that work as parental substrates, and the assembly process at the water/air interface.

In the first step, glass substrates were cleaned in an aqueous solution of 2 vol% Hellmanex® III in an ultrasonic bath for 15 min. After rinsing in pure water, the glass slides were deposited in ethanol and once more treated in an ultrasonic bath for 15 min (Figure 8.4 a). The cleaned glass was dried under a stream of compressed air. This step is crucial to remove any contaminants on the glass that could influence the particle assembly. The dried slides were then exposed to an oxygen plasma for 60 s in order to activate the glass surface for functionalization (Figure 8.4 b). The functionalization of the glass slides was accomplished with *N*-trimethoxysilylpropyl-*N,N,N*-trimethylammonium chloride. For this purpose, an aqueous solution of the silane with a concentration of 1 vol% was prepared and stirred for 10 min prior to immersion of the glass slides. Directly after plasma treatment, the glass slides were deposited into the silane solution (Figure 8.4 c). After 1 h the glass slides were rinsed with water and ethanol and dried in a gentle air stream. Finally, the glass slides were stored at  $90^\circ\text{C}$  for 1 h to complete the condensation of the silane onto the glass surface (Figure 8.4 d). For the assembly process, particle dispersions with 2–5 wt% were spin-coated onto the cationically functionalized glass slides (4000 rpm, 15 s) (Figure 8.4 e). Thereby, the particles were individually distributed on the

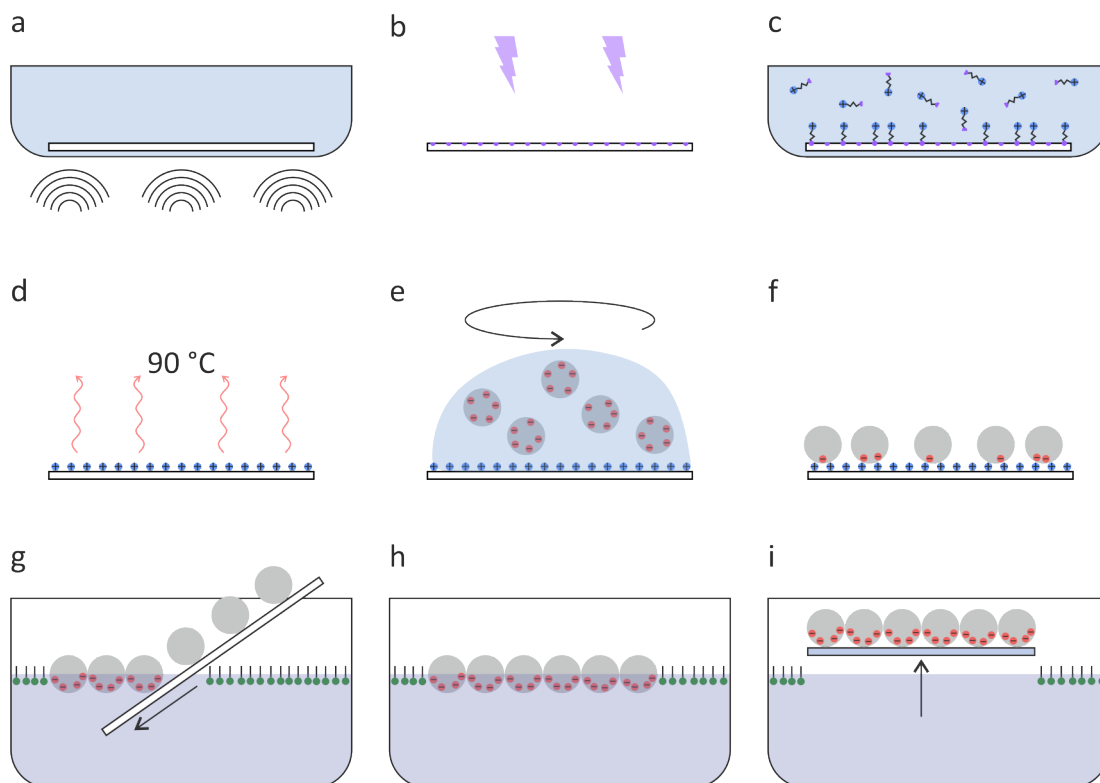


Figure 8.4: Schematic illustration of the procedure established by Retsch *et al.*<sup>[3]</sup> for the preparation of two-dimensional colloidal crystals. (a) Glass slides are cleaned in an ultrasonic bath. (b) The surface of the glass slides is activated in an oxygen plasma. (c)/(d) For the functionalization the activated glass is treated with a cationic silane, which condenses to the glass surface at elevated temperature. (e)/(f) Aqueous particle dispersions are spin-coated onto the functionalized glass slides to yield a layer of individually distributed particles. (g)/(h) Upon slow immersion of the glass slide into a solution of ammonia and SDS, the particles form a close-packed monolayer at the water/air interface. (i) The monolayer can be collected on various hydrophilic substrates.

glass, attracted by the cationic surface groups (Figure 8.4 f). Subsequently, the coated glass slides were slowly immersed into an aqueous solution under a shallow angle (Figure 8.4 g). The solution was adjusted to pH 12 by ammonia and additionally comprises 0.1 mM SDS. Upon immersion of the glass slide, the particles detached from the glass and assembled at the three-phase contact line into a hexagonal close packed monolayer (Figure 8.4 h). The freely floating monolayer could be collected from the water/air interface by arbitrary hydrophilic substrates. For this purpose, the substrates were submerged into the solution and lifted through the monolayer, whereby the particles attached to the surface (Figure 8.4 i).

For hydrophobic uptake the substrate was immersed through the floating monolayer at an angle of  $45^\circ$  relative to the water surface and was left at the bottom of the beaker with the monolayer facing upwards. After heating the water near the glass transition temperature of the particles or the substrate for 5 min on a hotplate, the monolayers were

removed from the solution. Finally, the substrates with the colloidal assemblies were dried under ambient conditions.

### 8.3.3 Preparation of quasicrystalline micropatterns

The procedure for fabrication of micropatterns used in this thesis follows the concept of rapid prototyping which combines photo and soft lithography (Figure 8.5).

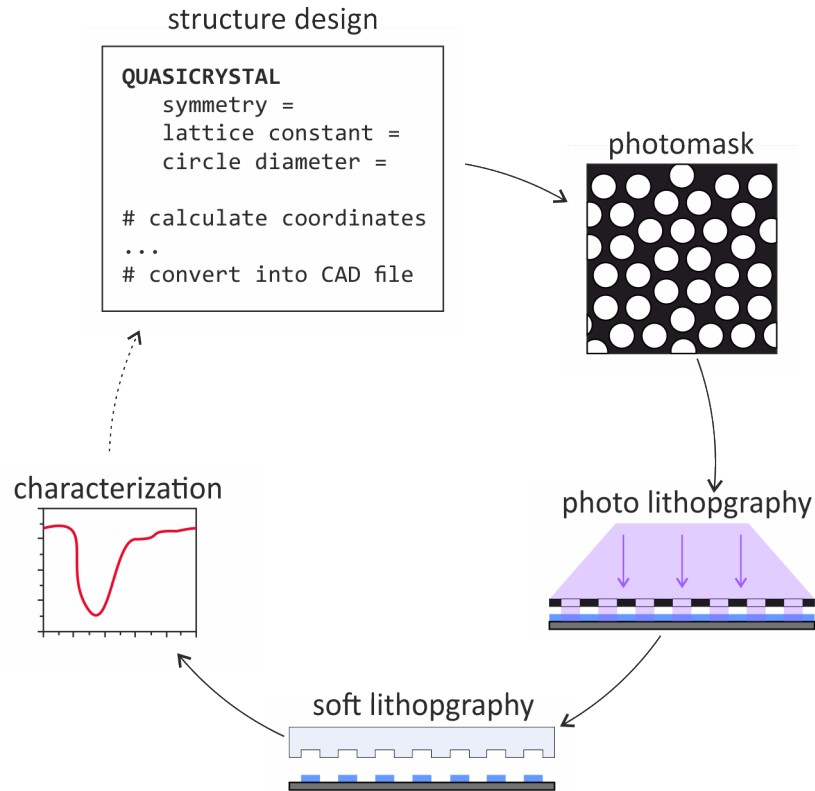


Figure 8.5: Schematic illustration of the rapid prototyping process including design of structures, printing of photomasks, photo lithography, soft lithography and characterization.

The micropatterns feature an arrangement of circular holes with a certain diameter and distance. The positions of the holes are calculated with the generalized dual method (GDM) and visualized by computer-aided design (CAD) software (AutoCAD®2017). Prior to the actual manufacture the structures are converted into high-resolution chrome photomasks (512000 dpi) (JD Photo Data, Hitchin, United Kingdom). For the photo lithographic manufacture of the templates a silicon wafer is used as substrate. As the structures have dimensions in the micrometer range, it is crucial to avoid contamination with e.g. dust during the manufacture. For this reason, the whole manufacture takes place in a clean room. Furthermore, the room is illuminated with yellow light to facilitate the handling of the photo resist. The polished silicon wafer is cleaned with 2-propanol and stored at 200 °C in the oven for 10 min. As the structures themselves do not adhere di-

rectly on the wafer due to their small size, an adhesion promoter in form of an additional continuous layer of photo resist is used. The cooled-off wafer is spin-coated with the photo resist SU8-2005 at 3000 rpm for 30 s. This results in a layer thickness of 5  $\mu\text{m}$  for the adhesion promoter. The wafer is stored on a hotplate at 95 °C for 2 min so that the solvent can evaporate from the photo resist film. Subsequently, the complete wafer is exposed to UV light with a wavelength of 365 nm for  $2 \times 2.5$  s in a mask-aligner (MJB4, SÜSS MicroTec AG, Munich, Germany). By illumination the photo initiator of the photo resist is activated and a renewed storage on a hotplate at 95 °C for 3 min cross-links the film. For the actual structure the photo resist SU8-2000.5 is spin-coated at 3000 rpm for 30 s to yield a layer thickness of 0.5  $\mu\text{m}$ . The film is dried on a hotplate at 95 °C for 1 min. This time the exposure with UV light is accomplished through the chrome photomask for  $2 \times 1.5$  s. Thereby only selected areas are cross-linked during the following treatment on a hotplate at 95 °C for 1 min. All non-cross-linked portions of the film are removed. For this purpose, the wafer is immersed in a bath of mr-DEV 600 and strongly agitated until all monomer is removed. Finally, the wafer is rinsed with 2-propanol and gently dried with a stream of air.

In the second preparation section the templates are replicated in PDMS via soft lithography. The liquid PDMS prepolymer is blended by mixing the base polymer with the curing agent in a 10:1 ratio. The mixture is poured onto the template and degassed at reduced pressure and ambient temperature until all bubbles have disappeared. The prepolymer is then cured at 75 °C for 2 h. The resulting solid PDMS layer comprising circular holes with quasicrystalline symmetry is peeled off the silica wafer.

Prior to further processing the PDMS is cleaned with 2-propanol to remove dust that could impair the adhesion of metal layers. Subsequently, 50–100 nm gold and 5 nm titanium are vapor deposited onto the structured PDMS. In the final step, the metal layer can be transferred onto flat PDMS via contact printing. By means of plasma treatment the surfaces of the flat PDMS and the titanium layer are oxidized and activated for bonding. The titanol and silanol groups are brought into contact and heated to 100 °C on a hotplate to form covalent bonds. Thereby the gold-titanium layer is transferred from the structured to the flat PDMS.

## **8.4 Methods**

### **8.4.1 Scanning electron microscopy**

SEM images were taken on a LEO 1530 Gemini Field Emission SEM (Carl Zeiss AG, Oberkochen, Germany) with a Schottky field emission cathode operating at an acceleration voltage of 3.00 kV. An in-lens detector and/or a secondary electron detector were used for imaging.

In order to avoid an accumulation of electrostatic charges during SEM measurements, the conductivity of the samples was increased by sputter-coating. The samples were placed on an aluminum stub (Plano) by a conductive adhesion graphite pad (Plano). The samples were sputter-coated with a layer of 1.3 nm platinum using a Cressington HR208 sputter-coater and a Cressington mtm20 thickness controller.

### **8.4.2 Contact angle**

Contact angle measurements were performed on an OCA 20 (DataPhysics Instruments GmbH, Filderstadt, Germany) with the sessile drop technique. Water was used as liquid with a surface tension of  $0.072 \text{ Nm}^{-1}$ .

### **8.4.3 Differential scanning calorimetry**

The thermal analysis of polymer particles and polymer was accomplished with a Q1000 DSC (TA Instruments, New Castle, United States) over a temperature range from  $-50 - 200 \text{ }^\circ\text{C}$  with a heating rate of  $10 \text{ K min}^{-1}$ . The received data was evaluated with Universal Analysis 2000 2.5A software to determine the  $T_g$ .

### **8.4.4 Optical microscopy**

Optical microscope images were acquired with an Olympus IX 70 light microscope (Olympus, Hamburg, Germany).

### **8.4.5 Atomic force microscopy**

Images by atomic force microscopy (AFM) were acquired using a NanoScope 4 (Bruker, Billerica, United States). Height profiles were recorded in tapping mode. The measured height profiles were flattened (1st order) with the software NanoScope Analysis 1(1st order) in order to prevent the influence of any tilt of the sample position on the sample stage.

## References

- [1] Goodwin, J. W.; Hearn, J.; Ho, C. C.; Ottewill, R. H. Studies on the preparation and characterisation of monodisperse polystyrene latices. *Colloid and Polymer Science* **1974**, *252*, 464–471.
- [2] Fernandez-Garcia, M.; Cuervo-Rodriguez, R.; Madruga, E. L. Glass transition temperatures of butyl acrylate-methyl methacrylate copolymers. *Journal of Polymer Science Part B: Polymer Physics* **1999**, *37*, 2512–2520.
- [3] Retsch, M.; Zhou, Z.; Rivera, S.; Kappl, M.; Zhao, X. S.; Jonas, U.; Li, Q. Fabrication of Large-Area, Transferable Colloidal Monolayers Utilizing Self-Assembly at the Air/Water Interface. *Macromolecular Chemistry and Physics* **2009**, *210*, 230–241.

## Danksagung

An dieser Stelle möchte ich mich bei allen bedanken, die mich während meiner Promotion unterstützt haben.

Als erstes möchte ich mich bei meinem Doktorvater Prof. Dr. Stephan Förster für die gute Betreuung bedanken. Besonders danke ich dir dafür mich auch in schwierigen Phasen der Promotion immer wieder motiviert und aufs Neue begeistert zu haben. Ich habe mich während meiner Zeit als Doktorand sowohl fachlich als auch persönlich enorm weiterentwickeln können.

Dem Elitenetzwerk Bayern sowie der Graduate School an der Universität Bayreuth danke ich für die finanzielle Unterstützung, wodurch ich viele Konferenzen und Seminare im In- und Ausland besuchen konnte.

Ich danke auch den technischen Angestellten, Karl-Heinz Lauterbach und Julia Moßner, unseren Sekretärinnen, Elisabeth Düngfelder und Jennifer Hennessy, sowie Dr. Stephan Hauschild. Ohne eure Hilfe bei vielen alltäglichen, kleinen und größeren Aufgaben wäre die Doktorandenzeit um einiges mühsamer gewesen.

Großer Dank gilt der gesamten (ehemaligen) Physikalischen Chemie. Besonders bedanken möchte ich mich bei meinen Laborkollegen Maria und Susi. Danke für die super Zusammenarbeit im Keller, die vielen Diskussion, die Ratschläge, und den Spaß, den wir gemeinsam hatten. Aber auch die Zeit zusammen als Förstis, Retschis und Kargis war unvergesslich und wird immer ein besonderer Abschnitt in meinem Leben bleiben. Danke euch allen für das klasse Arbeitsklima, die Mittagspausen am Kicker und die vielen Abende im Kaffeezimmer, auf unserer Terrasse oder im Biergarten. Danke, Pia, Fabi, Christian, Alex, Anna, Bernd, Astrid, Kristina, Kirsten, Arne, Matze und Eddie.

Danke auch den Zua-g'reisten, Felix, Anna, Daniel und Svenja, für die schöne Zeit in Bayreuth auch außerhalb der Uni.

Der größte Dank gilt den wichtigsten Menschen in meinem Leben: Patrick und Johanna, Mama, Papa, Meli, Martin und Magdalena. Ihr habt mich immer unterstützt und dazu beigetragen, dass ich heute hier stehe.



## Eidesstattliche Versicherungen und Erklärungen

§8 Satz 2 Nr. 3 PromO BayNAT

Hiermit versichere ich eidesstattlich, dass ich die Arbeit selbstständig verfasst und keine anderen als die von mir angegebenen Quellen und Hilfsmittel benutzt habe (vgl. Art. 64 Abs 1 Satz 6 BayHSchG).

§8 Satz 2 Nr. 3 PromO BayNAT

Hiermit erkläre ich, dass ich die Dissertation nicht bereits zur Erlangung eines akademischen Grades eingereicht habe und dass ich nicht bereits diese oder eine gleichartige Doktorprüfung endgültig nicht bestanden habe.

§8 Satz 2 Nr. 4 PromO BayNAT

Hiermit erkläre ich, dass ich Hilfe von gewerblichen Promotionsberatern bzw. –vermittlern oder ähnlichen Dienstleistern weder bisher in Anspruch genommen habe noch künftig in Anspruch nehmen werde.

§8 Satz 2 Nr. 7 PromO BayNAT

Hiermit erkläre ich mein Einverständnis, dass die elektronische Fassung meiner Dissertation unter Wahrung meiner Urheberrechte und des Datenschutzes einer gesonderten Überprüfung unterzogen werden kann.

§8 Satz 2 Nr. 8 PromO BayNAT

Hiermit erkläre ich mein Einverständnis, dass bei Verdacht wissenschaftlichen Fehlverhaltens Ermittlungen durch universitätsinterne Organe der wissenschaftlichen Selbstkontrolle stattfinden können.

Bayreuth, den \_\_\_\_\_

\_\_\_\_\_

Miriam Hummel